

Ph. D. Dissertation

**ELECTROCHEMICAL REDUCTION OF CARBON
DIOXIDE ON GOLD-BASED BIMETALLIC
ELECTRODES**

Ahmed Mohsen Mohamed Ismail Mohamed

Supervisors:

Dr. Csaba Janáky

Associate Professor

Dr. Edit Csapó

Assistant Professor



DOCTORAL SCHOOL OF CHEMISTRY
University of Szeged
Faculty of Science and Informatics
Department of Physical Chemistry and Materials Science
Szeged

2020

Table of Contents

Table of Contents	i
List of Abbreviations	iii
List of Figures	iv
List of Tables	viii
1. Introduction	1
2. Literature Background	3
2.1. Fossil Fuel Dependence.....	3
2.2. CO ₂ Recycling.....	4
2.3. Electrochemical CO ₂ Reduction.....	6
2.4. Monometallic Catalysts.....	10
2.5. Gold-Based Bimetallic Systems.....	15
2.5.1. Combination with Moderate CO-Binding Metal.....	15
2.5.2. Combination with Strong CO-Binding Metal.....	19
2.5.3. Combination with Weak CO-Binding Metal.....	20
2.5.4. Combination with Formate-Producing Metal.....	20
2.6. Non-Au-Based Bimetallic Systems.....	21
3. Motivation and Aims	25
4. Experimental	27
4.1. Materials.....	27
4.2. Au-Sn Bimetallic NPs.....	28
4.2.1. Synthesis of Au NPs.....	28
4.2.2. Synthesis of Au-Sn Bimetallic NPs.....	28
4.3. Au-Ag Bimetallic NPs.....	29
4.3.1. Synthesis of Au-Ag Alloy NPs.....	29
4.3.2. Synthesis of Au-Ag Core-Shell NPs.....	29
4.3.3. Synthesis of Ag NPs.....	30
4.4. Au-Pb Bimetallic NPs.....	30
4.4.1. Synthesis of Au-Decorated Pb NPs.....	30
4.4.2. Synthesis of Pb NPs.....	31
4.4.3. Synthesis of Pb-Decorated Au NPs (Pb ₉₅ Au ₅ NPs).....	31
4.5. Morphological and Structural Characterization of Au-based NPs.....	32
4.6. Electrode Preparation.....	33

4.7. Electrochemical Measurements and CO ₂ Reduction Products Analysis.....	34
4.8. Isotopic Labeling Experiments.....	36
4.9. In situ Raman Spectroelectrochemistry.....	37
4.10. Ambient Pressure Photoemission Spectroscopy Measurements.....	38
4.11. Theoretical Calculations.....	38
5. Results and Discussion.....	40
5.1. Au-Sn Bimetallic NPs Activity for CO ₂ RR.....	40
5.1.1. Synthesis and Characterization of Au-Sn Bimetallic NPs.....	40
5.1.2. Electrocatalytic CO ₂ Reduction Activity.....	45
5.2. Au-Ag Nanoalloys Activity for CO ₂ RR.....	54
5.2.1. Synthesis and Characterization of Au-Ag Alloy NPs.....	54
5.2.2. Electrocatalytic CO ₂ Reduction Activity.....	57
5.3. Au-Pb Bimetallic NPs Activity for CO ₂ RR.....	65
5.3.1. Synthesis and Characterization of Au-decorated Pb NPs.....	65
5.3.2. Electrocatalytic CO ₂ Reduction Activity.....	70
5.3.3. Computational Simulations.....	82
6. Conclusions.....	86
References.....	89
Acknowledgments.....	98
Publication list.....	101

List of Abbreviations

APS – Ambient pressure UV-photoelectron spectroscopy

CO₂RR – CO₂ reduction reaction

CHE – Computational Hydrogen Electrode

CV – Cyclic voltammetry

DFT – Density functional theory

ECSA – Electrochemical active surface area

E_F – Fermi level

FE – Faradaic efficiency

GC – Gas chromatography

GC-BID – gas chromatography coupled with a barrier dielectric discharge detector

GC-MS – gas chromatography coupled with a mass spectrometer detector

HER – Hydrogen evolution reaction

LSV – Linear sweep voltammetry

LSPR – Localized surface plasmon resonance

NPs – Nanoparticles

NWs – Nanowires

OER – Oxygen evolution reaction

OCP – Open circuit potential

PCET – Proton-coupled electron transfer

PVP – Poly(vinylpyrrolidone)

RDS – Rate-determining step

RHE – Reversible hydrogen electrode

SEM – Scanning electron microscopy

TEM – Transmission electron microscopy

WF – Work function

XRD – X-ray diffraction

List of Figures

Figure 1. CO ₂ recycling (electrochemical CO ₂ reduction coupled to renewable electricity sources, can enable its conversion into fuels and chemicals in a sustainable way).....	5
Figure 2. Pathways for the electrochemical reduction of CO ₂ to CO and HCOOH. [28].....	8
Figure 3. Oxide-derived metal electrode formation.....	13
Figure 4. Schematic illustration of various mixing patterns and geometric structures of bimetallic electrocatalysts	15
Figure 5. Schematic diagram of the bi-functional interface effect and stabilization of *COOH intermediate [59]	16
Figure 6. Schematic illustration of the synthesis of Au-Sn bimetallic NPs using a two-step approach.....	29
Figure 7. Schematic illustration of the synthesis of Au-Ag alloy NPs by varying the initial Au:Ag molar ratio	30
Figure 8. Schematic illustration of the preparation of Au-Pb bimetallic using a two-step approach.....	31
Figure 9. (A) LSV profiles of Au ₂ Sn ₁ catalyst recorded with different loadings in CO ₂ -saturated 0.1 M NaHCO ₃ stabilized after multiple cycles. The black line indicates the activity of the bare glassy carbon (GC) substrate. Scan rate = 5 mV s ⁻¹ . (B) A photograph of the prepared electrode, which shows the deposited layer on GC. 33	33
Figure 10. LSV profiles of Au ₈₀ Ag ₂₀ catalyst recorded with different loadings in CO ₂ -saturated 0.1 M NaHCO ₃ stabilized after multiple cycles. Scan rate = 5 mV s ⁻¹	34
Figure 11. Schematic diagram of the electrochemical reduction of CO ₂ in a two-compartment cell. (counter electrode (CE), working electrode (WE), reference electrode (RE)).....	36
Figure 12. The optimized structures of the most stable surfaces. The difference between Pb-Au3%O (111) and Pb-Au3%Od (111) is that the O is lower in the subsurface of Pb-Au3%Od (111) and is more stable by 0.1 eV compared to Pb-Au3%O (111), O is on the surface.	39
Figure 13. (A) X-ray diffraction patterns of Au-Sn bimetallic NPs and the parent metals. The diffractions corresponding to the respective crystal phases in the samples are indicated by these marks; ♦ Au, ◊ AuSn, • AuSn ₂ , Δ Sn. Rietveld refinement of the XRD patterns recorded for samples: (B) Au ₂ Sn ₁ , (C) Au ₁ Sn ₁	41
Figure 14. (A) TEM and (B) HR-TEM images of gold seeds. The lattice fringes of the sample were observed clearly showing a d-spacing value of 0.23 nm corresponding to (111) plane of fcc Au.....	42
Figure 15. TEM images of Au-Sn bimetallic NPs. (A) Au ₂ Sn ₁ , (B) Au ₁ Sn ₁ , (C) Au ₁ Sn ₂ , and (D) Au ₁ Sn ₄ . (E-H) corresponding HR-TEM images. Lattice fringes are highlighted together with the corresponding crystal facets. The thickness of the amorphous layer increased, in the series of samples with growing tin content as follows; 1.5 ± 0.19, 1.8 ± 0.32, 2.45 ± 0.25, and 2.75 ± 0.23 nm	43
Figure 16. Size distribution of Au-Sn bimetallic NPs (a) Au seeds, (B) Au ₂ Sn ₁ , (C) Au ₁ Sn ₁ , (D) Au ₁ Sn ₂ , and (E) Au ₁ Sn ₄	43
Figure 17. (A) and (B) TEM images of Au ₂ Sn ₁ bimetallic NPs with a core-shell structure suggesting the diffusion of Sn.....	44
Figure 18. High-resolution XP spectra of Au-Sn bimetallic NPs: (A) Au 4f spectrum, and (B) Sn 3d spectrum	45
Figure 19. (A) LSV profiles of Au ₁ Sn ₂ catalyst recorded in CO ₂ -saturated 0.1 M NaHCO ₃ , and N ₂ -saturated 0.1 M Na ₂ SO ₄ . Scan rate = 5 mV s ⁻¹ . (B) LSV profiles of Au-Sn NPs and Au and Sn foils, recorded in CO ₂ -saturated 0.1 M NaHCO ₃ stabilized after multiple cycles. The black line indicates the activity of the bare glassy carbon substrate. Scan rate = 5 mV s ⁻¹ . The loading was 0.35 mg cm ⁻² in all cases.....	46
Figure 20. Electrochemical CO ₂ reduction performance of the Au ₁ Sn ₂ catalyst: (A) total current density as a function of time at various potentials, (B) HCOOH, CO, and H ₂ partial current densities. Error bars represent the standard deviation, obtained by studying three different electrodes	47

Figure 21. Long-term stability performance of Au ₁ Sn ₂ catalyst measured in CO ₂ -saturated 0.1 M NaHCO ₃ at -1.0 V vs. RHE.....	47
Figure 22. CO ₂ reduction activity of Au-Sn bimetallic NPs at -0.8 V, -0.9 V, -1.0 V, and -1.1 V vs. RHE: total current density as a function of time (A) Au foil, (B) Au ₂ Sn ₁ , (C) Au ₁ Sn ₁ , (D) Au ₁ Sn ₄ , and (E) Sn foil. (F-J) the corresponding FE of CO, HCOOH, and H ₂ . (K-O) the corresponding partial current densities of CO, HCOOH, and H ₂	48
Figure 23. TEM images of Au ₁ Sn ₂ catalyst: (A) before and (B) after 10 h electrolysis in CO ₂ -saturated 0.1 M NaHCO ₃ at -1.0 V vs. RHE	49
Figure 24. Electrochemical CO ₂ reduction activity of Au-Sn NPs, and parent metals. (A) Total current density, (B) normalized total current density measured at -1.1 V vs. RHE. Error bars represent the standard deviation obtained by studying three different electrodes.....	49
Figure 25. Electrochemical CO ₂ reduction activity of Au-Sn NPs, and parent metals. Faradaic efficiency values as a function of composition at - 1.0 V vs. RHE. Error bars represent the standard deviation obtained by studying three different electrodes	50
Figure 26. Electrochemical CO ₂ reduction performance of physically mixed Au and Sn electrode: (A) total current density as a function of time at various potentials, (B) Reduction potential dependence of Faradaic efficiency and (C) partial current density	51
Figure 27. Variation of the work function of Au-Sn bimetallic NPs as a function of composition. Error bars represent the standard deviation obtained by studying three different samples for each composition	51
Figure 28. The ratio of the products formed during potentiostatic electrolysis at -1.1 V vs. RHE in a ¹² CO ₂ -saturated 0.1 M NaH ¹³ CO ₃ electrolyte (right axis), and in a ¹³ CO ₂ -Saturated 0.1 M NaH ¹² CO ₃ electrolyte (left axis) under nonequilibrium conditions. The products are (A) ¹³ CO and ¹² CO, (B) H ¹³ COOH and H ¹² COOH.....	52
Figure 29. Raman spectra collected on Au ₁ Sn ₂ catalyst in CO ₂ -saturated 0.1 M NaHCO ₃ : (A) at a potential of -0.8 V vs. RHE, (B) as a function of the employed bias potential	53
Figure 30. (A) Raman spectra collected on Sn NPs-coated electrode in CO ₂ -saturated 0.1 M NaHCO ₃ . (B) Potential dependence for the ν(C-H) of formate anion at 2880 cm ⁻¹ band intensity on Au ₁ Sn ₂ and Sn NPs-coated electrodes as a function of the employed bias potential	53
Figure 31. (A) Raman spectra collected on Au ₁ Sn ₂ catalyst-coated electrode in N ₂ -saturated 0.1 M Na ₂ SO ₄ at different bias potentials. (B) Raman spectra collected on Au NP-coated electrode in CO ₂ -saturated 0.1 M NaHCO ₃ at different bias potentials	54
Figure 32. TEM images of (A) Au NPs and (B) Ag NPs	54
Figure 33. TEM images of Au-Ag alloy NPs with different compositions. (A) Au ₈₀ Ag ₂₀ , (B) Au ₆₀ Au ₄₀ , (C) Au ₄₀ Ag ₆₀ , and (D) Au ₂₀ Ag ₈₀ . (E-H) The corresponding magnified TEM images	55
Figure 34. (A) TEM image of Au NPs (core) and (B) corresponding magnified TEM image with an insight figure of the size distribution histogram. (C) TEM image of Ag@Au core-shell NPs and (D) corresponding magnified TEM image of a single particle with insight figure of the size distribution histogram	55
Figure 35. XRD patterns of Au-Ag alloy NPs with different compositions, Ag@Au core-shell NPs and the monometallic Au and Ag NPs.....	56
Figure 36. (A) Normalized UV-vis absorption spectra of Au, Ag, and Au-Ag alloy NPs with different compositions. (B) LSPR band maximum as a function of the Au content in the bimetallic NPs. The photograph in the inset shows the color change with the composition. (C) Normalized UV-vis absorption spectra of Ag@Au core-shell NPs	57
Figure 37. (A) LSV profiles of Au ₆₀ Ag ₄₀ catalyst in CO ₂ -saturated 0.1 M NaHCO ₃ (pH = 6.62) and N ₂ -saturated 0.1 M Na ₂ SO ₄ (pH = 6.88), scan rate = 5 mV s ⁻¹ . (B) LSV profiles of Au-Ag alloys with different compositions in CO ₂ -saturated 0.1 M NaHCO ₃ (pH = 6.62), scan rate = 5 mV s ⁻¹ . The loading was 0.53 mg cm ⁻² in all cases	58
Figure 38. Tafel plot of the partial current density for CO on Au ₆₀ Ag ₄₀ catalyst	58

- Figure 39.** (A) Total current density for Au₆₀Ag₄₀ NPs as a function of time, a representative of electrolysis experiment at different potentials. At higher overpotentials, the current data becomes noisy as a result of the intense gas evolution that fluctuates the current. (B) Total current density for Au, Ag and Au–Ag alloy NPs as a function of applied potential. (C) Faradaic efficiency of CO and H₂ formation on Au–Ag alloy NPs with different compositions at –0.7 V vs. RHE.....59
- Figure 40.** Faradaic efficiency of CO and H₂ formation on Au–Ag alloy NPs with different compositions at –0.7 V vs. RHE.....60
- Figure 41.** Faradaic efficiency of CO and H₂ on (A) Au, (B) Au₆₀Ag₄₀, and (C) Ag NPs as a function of the applied potential60
- Figure 42.** Electrochemical CO₂ reduction performance of Au–Ag alloys with different compositions. Partial current densities for (A) CO and (B) H₂ as a function of the applied potential61
- Figure 43.** Square root photoemission curves for (A) Au, (B) Au₈₀Ag₂₀, (C) Au₆₀Ag₄₀, (D) Au₄₀Ag₆₀, (E) Au₂₀Ag₈₀, (F) Ag, and (G) Ag@Au core-shell NPs62
- Figure 44.** Electronic properties of Au–Ag alloys. Position of Fermi level of Au–Ag alloys as a function of Ag content63
- Figure 45.** Electronic properties of Au–Ag alloys. (A) Work function of Au–Ag alloys versus Ag content (left axis) and CO partial current density versus Ag content (right axis). (B) Work function of Au–Ag alloys versus Ag content (left axis) and H₂ partial current density versus Ag content (right axis)63
- Figure 46.** Comparison of CO₂ reduction activity of Ag@Au core-shell with that of Au₂₀Ag₈₀ alloy NPs. Total current density vs time for (A) Ag@Au core-shell, and (B) Au₂₀Ag₈₀ alloy NPs. Faradaic efficiency for CO and H₂ production vs applied potential on (C) Ag@Au core-shell, and (D) Au₂₀Ag₈₀ alloy NPs64
- Figure 47.** X-ray diffraction patterns of Au–Pb NPs and the parent metals. These marks indicate the diffractions corresponding to the respective crystal phases in the samples: (♦) α-PbO₂, (φ) α-PbO, (●) Pb (dot line), (Δ) Au (JCPDS No.: 04-0784).....65
- Figure 48.** TEM images of (B) Au₅Pb₉₅, (C) Au₂₀Pb₈₀, (D) Au₅₀Pb₅₀ NPs, and (D) single particle of Au₅Pb₉₅, showing lattice fringes with a d spacing of 0.28 nm corresponding to the (111) plane of fcc Au, which are located around a core, which features lattice fringes with d-spacing values of 0.31 and 0.28 nm corresponding to (101) and (111) planes of α-PbO and Pb, respectively. The nominal compositions were used for the notation of the Au–Pb bimetallic system66
- Figure 49.** TEM images of: (A) Pb NPs (d = 40 ± 3.5 nm), (B) Au NPs (d = 29 ± 3 nm), and (C) Pb₉₅Au₅ (d = 32.3 ± 6 nm)67
- Figure 50.** (A) TEM image of Au₅₀Pb₅₀ showing the deposited Au NPs on the surface of Pb NPs. (B) High resolution TEM image of Au₅₀Pb₅₀ showing lattice fringes with a d spacing of 0.23 nm corresponding to the (111) plane of fcc Au, which are located on the on the top of Pb NPs, which features lattice fringes with d spacing values of 0.31 and 0.28 nm corresponding to (101) and (111) planes of α-PbO and Pb, respectively 67
- Figure 51.** XPS survey scans of the Au–Pb bimetallic catalysts: Au₅₀Pb₅₀, Au₂₀Pb₈₀, Au₅Pb₉₅, and Pb₉₅Au₅ .68
- Figure 52.** High-resolution XP spectra of the Pb 4f peaks: (A) Au₅Pb₉₅ (B) Au₂₀Pb₈₀ (C) Au₅₀Pb₅₀, and (D) Pb₉₅Au₅.....69
- Figure 53.** High-resolution XP spectra of the (A) Pb 4f peaks and (B) O 1s peaks for Au₅₀Pb₅₀ catalyst; before and after CO₂ electrolysis in CO₂-saturated 0.5 M KHCO₃ (pH = 7.2) at –1.07 V vs. RHE for 1 h, and after Ar⁺ sputtering70
- Figure 54.** Representative LSV profiles of Au₅₀Pb₅₀ catalyst in CO₂-saturated 0.5 M KHCO₃ (pH = 7.2) and N₂-saturated 0.5 M Na₂SO₄ (pH = 7.5), scan rate = 5 mV s⁻¹.....70
- Figure 55.** LSV profiles of Au–Pb NPs with different compositions in CO₂-saturated 0.5 M KHCO₃ (pH= 7.2) stabilized after multiple cycles. Scan rate = 5 mV s⁻¹. (A) The layers were heated in air atmosphere at 280 °C, and (B) The layers were heated in Ar atmosphere at 280 °C. The loading was 0.48 mg cm⁻² in all cases.....71

- Figure 56.** Cyclic voltammograms of the Au₂₀Pb₈₀, Pb, and Au NPs used for the qualitative characterization in CO₂-saturated 0.5 M KHCO₃ with a scan rate of 50 mV s⁻¹, the potential was scanned between -1.1 and 2.0 V vs. RHE. Each cycle starts with an anodic scan followed by a cathodic scan 72
- Figure 57.** Electrochemical CO₂ reduction activity of Au:NPs (A) total current density as a function of time at various potentials, (B) H₂, and CO Faradaic efficiencies. Electrochemical CO₂ reduction activity of air-heated Pb: (C) total current density as a function of time at various potentials, and (D) H₂, CO, and HCOOH Faradaic efficiencies measured in CO₂-saturated 0.5 M KHCO₃..... 72
- Figure 58.** Electrochemical CO₂ reduction activity of the Air-heated Au₅₀Pb₅₀ catalyst: (A) total current density as a function of time at various potentials, and (B) H₂, CO, HCOOH, and CH₄ Faradaic efficiencies at different applied potentials..... 73
- Figure 59.** Electrochemical CO₂ reduction activity of the Au₅₀Pb₅₀ catalyst, 3 h CO₂ electrolysis measured in CO₂-saturated 0.5 M KHCO₃ at -1.07 V vs. RHE:(A) The layers were heated in Ar atmosphere at 280 °C, and (B) The layers were heated in Ar atmosphere at 280 °C..... 73
- Figure 60.** Electrochemical CO₂ reduction activity of the Pb₉₅Au₅ catalyst:(A) total current density as a function of time at various potentials, and (B) H₂, CO, HCOOH, and CH₄ Faradaic efficiencies in CO₂-saturated 0.5 M KHCO₃. The layers were heated in air atmosphere at 280 °C..... 74
- Figure 61.** Electrochemical CO₂ reduction activity of (A) Au₅Pb₉₅ and (B) Au₂₀Pb₈₀ catalysts: showing total current density and H₂, CO, HCOOH, and CH₄ Faradaic efficiencies at different applied potentials for 1h CO₂ electrolysis measured in CO₂-saturated 0.5 M KHCO₃. The layers were heated in air atmosphere at 280 °C. 74
- Figure 62.** Electrochemical CO₂ reduction activity of the Au-Pb catalysts at -1.07 V vs. RHE: (A) Total current density, (B) the partial current density of CH₄ as a function of composition. The partial current density of H₂, CO, and HCOOH on (C) Air-heated catalysts, and (D) Ar-heated samples..... 75
- Figure 63.** Electrochemical CO₂ reduction performance of the Au-Pb catalysts: Faradaic efficiency for H₂, CO, HCOOH, and CH₄, and total current density values measured during 3 h electrolysis at -1.07 V vs. RHE in CO₂-saturated 0.5 M KHCO₃ for air-heated samples; (A) Pb₉₅Au₅, (B) Au₅Pb₉₅, (C) Au₂₀Pb₈₀. (D-F) corresponding Ar-heated samples. 76
- Figure 64.** Stability of Au₅₀Pb₅₀ catalyst measured in CO₂-saturated 0.5 M KHCO₃ at -1.07 V vs. RHE. Total current density and FE for H₂, CO, HCOOH, and CH₄ versus time. The layer was heated in an air atmosphere at 280 °C 77
- Figure 65.** Isotopic labeling experiment. Mass spectra of the obtained products: (A-B) ¹³CH₄ and (C-D) ¹³CO during electrolysis at -1.07 V vs. RHE on Pb₉₅Au₅ catalyst when both CO₂ and KHCO₃ were ¹³C labeled.... 78
- Figure 66.** Electrochemical CO₂ reduction performance of the physically mixed (Au+Pb) electrode: Faradaic efficiency for H₂, CO, HCOOH, and CH₄, and total current density values measured during 3 h electrolysis at -1.07 V vs. RHE in CO₂-saturated 0.5 M KHCO₃. The layer is heated in an air atmosphere..... 79
- Figure 67.** Faradaic efficiency for H₂, HCOOH, and CH₄ and total current density values measured during 3 h electrolysis at -1.07 V vs. RHE in CO-saturated 0.5 M KHCO₃ using Pb₉₅Au₅ catalyst. The layer is heated in an air atmosphere..... 79
- Figure 68.** (A) Raman spectra collected in CO₂-saturated 0.5 M KHCO₃ as a function of the applied potential on Au₅₀Pb₅₀ catalyst, and (B) a magnified graph showing the PbO bands. The potential is versus RHE scale 80
- Figure 69.** (A) Raman spectra collected in CO₂-saturated 0.5 M KHCO₃ as a function of the applied potential on pure Pb, (dotted lines mark the bands from the substrate), and (B) a magnified graph of the spectra. The potential is versus RHE scale 82
- Figure 70.** Potential dependence of (C-H -stretch) intensity of formate anion at 2950 cm⁻¹, on Au₅₀Pb₅₀ and Pb NPs, as a function of the applied potential 82
- Figure 71.** Energy profile on Pb-Au system with 3% Au and O impurities inside the surface. Each step involves a H⁺ and e⁻ transfer. In green is the full CH₄ path. The reaction can be stopped early in the HCOOH path in blue. The transition from CHOH to CH can be stopped if the intermediate CHOH is too close to the O site in the lattice (partial oxide phase) in the red path that could lead to CO reduction. 84

List of Tables

Table 1. Electrochemical half-reactions with equilibrium potentials and the possible products [21].....	7
Table 2. Faradaic efficiencies of CO ₂ reduction products on metal electrodes in CO ₂ -saturated 0.1 M KHCO ₃ (pH = 6.8) [26]*.....	9
Table 3. Comparison of various bimetallic catalysts in the literature studied in CO ₂ reduction.....	23
Table 4. Phase composition of Au-Sn bimetallic NPs determined from Rietveld refinement.....	41
Table 5. Bulk and surface composition of Au-Sn bimetallic NPs.....	45
Table 6. Bulk composition of Au-Ag bimetallic NPs as determined by EDX analysis.....	56
Table 7. Bulk and surface composition of Au-Pb bimetallic NPs.*.....	69
Table 8. Assignment of Raman bands observed during CO ₂ electroreduction on Au ₅₀ Pb ₅₀ catalyst in CO ₂ -saturated 0.5 M KHCO ₃	81

1. Introduction

Global energy demand increasing rapidly for the advancement of society and economic growth. Despite the extensive efforts to develop clean and renewable, carbon-neutral sources, traditional fossil fuels still occupy a leading position in today's energy matrix. Carbon dioxide (CO₂) emissions generated via the combustion of fossil energy resources lead to global climate change. Consequently, an insistent need to find a way to offset the accumulation of CO₂ in the atmosphere has emerged. The capture and sequestration process of CO₂ has been proposed; however, the high cost, laborious process, and the high space requirement as well as the potential of leakage might seem inconsistent with sustainable development. In contrast, the conversion of CO₂ is a promising route to turn the waste CO₂ into valuable fuels and chemicals [1–3]. This approach has received considerable attention and significant progress has been achieved in this field. CO₂ can be converted through various processes, including thermochemical, photochemical, electrochemical, and biological techniques. Among them, electrochemical CO₂ reduction reaction (CO₂RR) powered by renewable energy has attracted great attention to convert CO₂ molecules into high-value chemicals that can act as energy carriers is an attractive approach to create an artificial and sustainable carbon cycle. CO₂R in an aqueous environment is rather complicated because of substantial kinetic barriers, compared to the competing hydrogen evolution reaction (HER) Therefore, developing electrocatalysts with high efficiency, selectivity, and long-term stability is a crucial step of great urgency towards industrialization [4].

Fundamental research started on bulk metal catalysts and the elementary mechanistic studies provide the essential understanding behind the catalytic activity, product selectivity and the nature of catalytic active sites. These studies showed that the reduction performance can be improved only via changing the catalyst material. Therefore, new catalysts have been developed and characterized such as monometallic nanoparticles (NPs), bimetallic NPs, oxide-derived metals, metal-organic frameworks, metal-free carbon materials, and nanoporous films to investigate the impact of various factors toward the CO₂R activity and selectivity, including the catalyst surface structure, size, morphology, and composition as well as the electrolyte ions, and the electrochemical cell design [5].

It was very important for the research community to understand the catalytic performance of pure metals towards CO₂R firstly before studying the composition effect, and determine the existing challenges: (1) high carbon monoxide (CO) selectivity is associated with expensive noble metal catalysts; (2) catalysts, that generate formic acid (HCOOH) suffer from low current densities and high overpotentials; (3) poor selectivity of hydrocarbons producing metal surfaces. Alloying is a promising method to improve the electrocatalytic performance by tuning the binding strength of the intermediates on a catalyst surface. Bimetallic NPs provide an ideal platform for studying the effect of surface composition. Such materials can provide active sites for reaction intermediates with tunable binding strength and thus exhibit altered reactivity relative to their monometallic counterparts [6]. The unique properties of the bimetallic catalysts arise from tailoring the electronic properties (the hybridization of the atomic orbitals that shift the d-band center with the respect to the Fermi level (E_F) and the geometric effects, which stems from the atomic arrangement at the active sites. Several combinations have been extensively studied and showed better activity compared to the constituent metals. Representative examples of Cu-free bimetallic catalysts showed recently the formation of $> 2e^-$ reduction products, demonstrating how bimetallic NPs can be employed to overcome the scaling relations in the CO₂RR [7]. Inspired from these studies, we wanted to explore the electrocatalytic activities of Au-based bimetallic catalysts and contribute to the development of bimetallic catalysts for CO₂R.

2. Literature Background

2.1. Fossil Fuel Dependence

The increasing global energy demand for economic growth and improving the standard of living is a pressing need to supply secure, clean, and sustainable energy. However, traditional fossil fuels still occupy a remarkable position in today's energy structure. Most of the energy supply in different sectors (transportation, industrial, domestic, and commercial) depends on the combustion of fossil energy sources (petroleum, natural gas, and coal). The imbalance between the natural consumption of CO₂, reduction of CO₂ in the photosynthesis by green plants and autotrophic organisms to store and release energy, and anthropogenic emissions gives rise to a net increase in the CO₂ levels in the atmosphere, leading to global climate changes, and these changes are predicted to become more severe in the future [1]. Therefore, creating sustainable solutions to improve the development of carbon-neutral energy sources and minimize the effects of CO₂ as a greenhouse gas in the atmosphere and decrease our dependence on fossil fuels is the most critical challenge facing humanity in the 21st century [3,8,9]. Strategies that are in progress could be grouped into three categories: decarbonization, carbon sequestration, and CO₂ recycling [4].

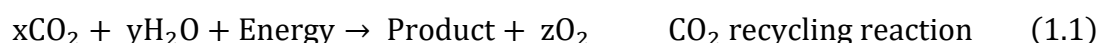
Significant progress is being carried out in decarbonization, the advancement of renewable power technologies resulted in an increase in the volume and a decrease in the price of electricity generated from renewable sources, such as solar and wind [10]. However, the intermittent nature of these sources limits the percentage of electricity they can supply without instability and power fluctuations [11], where all available energy storage technologies, including compressed air, batteries, redox flow batteries, pumped hydro, and flywheels, have limited scalability, versatility, and maximum storage time [12,13]. Therefore, developing a way to long-term storage of renewable energy for times when it is not being generated is a crucial step for controlling CO₂ emissions, and also, an alternative carbon source for chemicals and carbon-based products is needed to replace fossil fuel-derived chemical production. The use of biomass (tree and plants), the most accessible alternative carbon source, is limited by the amount of land required not to affect the environment and food-producing crops negatively, and to avoid any potential human health-related consequences. Biomass power generation includes; burning wood chips in power plants, burning biogas from waste treatment plants, and the generation of

methanol (CH₃OH) and ethanol (C₂H₅OH), which can be used as fuels [3,14]. On the other hand, the geological and deep-sea CO₂ sequestration is a strategy that allows some continued net production of CO₂ but prevents its release to the atmosphere through capturing from industrial point sources and storing it underground. The high cost of CO₂ separation from a power plant, together with transportation and storage costs as well as the high requirement of space, and the long-term impacts of geological sequestration on the environment are uncertain because of the potential for leakage are the main challenges for carbon sequestration [15].

Based on the limitations outlined above, CO₂ recycling (reutilization) could be an effective and promising way for the sustainable development of society. CO₂ conversion into carbon-based products offers a way to turn waste emissions into valuable fuels and chemicals that can act as energy carriers, creating an artificial carbon cycle. In the next section, we discuss the advantages of this approach and the different ways in which CO₂ conversion might be accomplished.

2.2. CO₂ Recycling

The development of CO₂ recycling technologies is driven by the desire to reduce fossil fuel dependence and to lower the negative impact on climate changes. CO₂ is a stable molecule and the most oxidized form of carbon, together with bicarbonate with an oxidation state of 4+. To search for a suitable scheme for CO₂ conversion to more energetic products, several strategies have been developed [16], including electrochemical reduction [4,5], photochemical reduction [17,18], thermochemical reduction [19], and CO₂ fixation in natural photosynthesis and bioinspired catalysts [20]. Therefore, there has been much work done in this field to develop catalytic materials for better selectivity and efficiency. **Figure 1** shows the conversion of CO₂ into chemicals and fuels using renewable energy and closing the carbon cycle that would be possible if CO₂ is electrochemically reduced, which is the focus of this thesis. The transformation of CO₂ follows the overall formula,



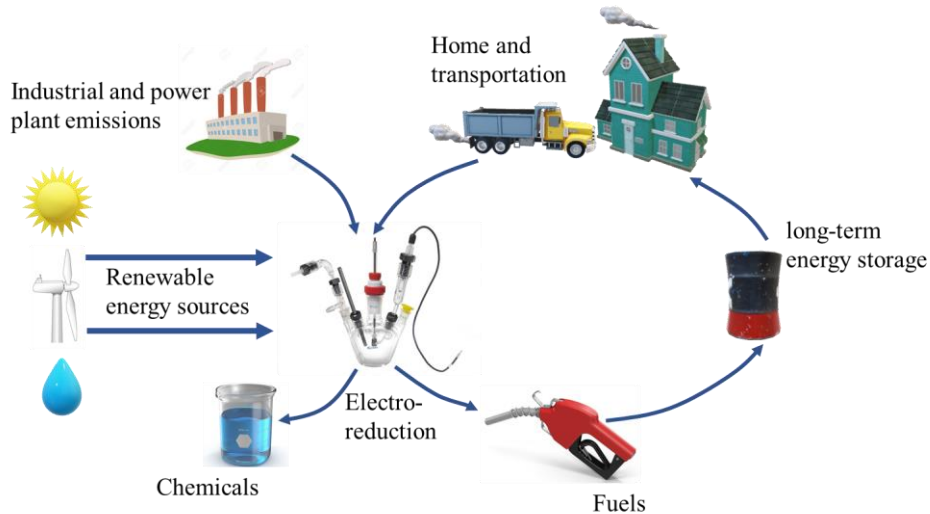
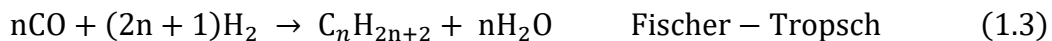


Figure 1. CO₂ recycling (electrochemical CO₂ reduction coupled to renewable electricity sources, can enable its conversion into fuels and chemicals in a sustainable way).

Briefly, the thermochemical conversion is a thermally activated CO₂ hydrogenation using hydrogen (H₂) as a reducing agent. CO₂ can be reduced to CO by the reverse water gas shift reaction,

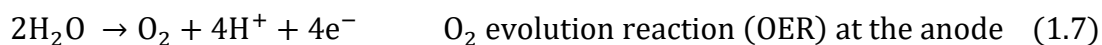


with an excess of H₂, and the water is condensed out, the product is a mixture of H₂ and CO, which is called Syngas. Syngas can be used as a feedstock to long-chain hydrocarbons or small molecules such as methane (CH₄) and CH₃OH. These reactions are called the Fischer-Tropsch reaction, methanation, and methanol synthesis, respectively [21].



All these reactions run at high temperatures and pressures, and the H₂ source is a key issue in a CO₂ hydrogenation process. For the formation of renewable chemicals, H₂ must come from a renewable source, the most promising route to renewable H₂ is water splitting, which is driven electrochemically using electricity from renewable energy sources [11,22,23], according to the following half-reactions,

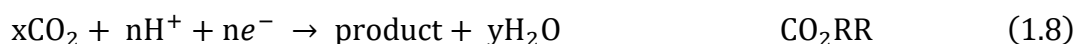




Research on thermochemical CO₂ reduction is needed and developing new catalysts for HER is required for commercial production through water electrolysis. Among the abovementioned approaches for CO₂ conversion, the electrochemical CO₂RR has attracted quickly growing attention on account of the following points: (1) its mild operating temperature and pressure, (2) a wide range of carbon-based products can be generated by controlling the applied factors, (3) it offers a way to store the electricity from intermittent sources such as, solar and wind, (4) and it could be accomplished in a single electrochemical process [21]. These features would likely lower the costs associated with the process, allowing the production to be more distributed than thermochemical conversion would do.

2.3. Electrochemical CO₂ Reduction

In order to carry out the CO₂ conversion given by **Equation 1.1** via electrochemistry, the overall reaction needs to be split into two half-reactions, water oxidation (OER, **Equation 1.7**) at the anode and CO₂RR which occurs at the cathode,



CO₂RR in aqueous electrolytes is rather complex and bears substantial kinetic barriers, compared to the competing HER, as multiple proton and electron transfer steps are involved in the different reaction pathways, leading to many possible products [4]. **Table 1** lists the equilibrium (thermodynamic) potentials for different possible products associated with CO₂RR. All the standard potentials here were reported on the pH-independent reversible hydrogen electrode (RHE) scale. Furthermore, significant energy input is needed to drive the overall reaction, where the minimum possible potential (i.e., the difference between the equilibrium potentials of CO₂RR and OER) is larger than 1 V. This indicates that the electrochemical CO₂RR will run at a potential exceeds the thermodynamic potential. This extra voltage is referred to as called overpotential, so one of the catalyst roles is to lower the overpotential (energy barrier of the reaction pathway) and make the system more efficient. Thermodynamically HER takes place at 0 V (**Table 1**), which is comparable to the equilibrium potentials of CO₂R to hydrocarbons and alcohols. Thus, the large overpotentials required for CO₂RR are also active for HER, resulting in poor product selectivity. Therefore, developing electrocatalysts with high efficiency,

selectivity, and long-term stability is a crucial step of great urgency towards industrialization [5,24].

Table 1. Electrochemical half-reactions with equilibrium potentials and the possible products [21].

Reaction	E^0 (V vs RHE)	Product
$\text{CO}_2 + 2\text{H}^+ + 2\text{e}^- \rightarrow \text{HCOOH}_{(\text{aq})}$	-0.12	Formic acid
$\text{CO}_2 + 2\text{H}^+ + 2\text{e}^- \rightarrow \text{CO}_{(\text{g})} + \text{H}_2\text{O}$	-0.10	Carbon monoxide
$\text{CO}_2 + 6\text{H}^+ + 6\text{e}^- \rightarrow \text{CH}_3\text{OH}_{(\text{aq})} + \text{H}_2\text{O}$	0.03	Methanol
$\text{CO}_2 + 8\text{H}^+ + 8\text{e}^- \rightarrow \text{CH}_4_{(\text{g})} + 2\text{H}_2\text{O}$	0.17	Methane
$2\text{CO}_2 + 8\text{H}^+ + 8\text{e}^- \rightarrow \text{CH}_3\text{COOH}_{(\text{aq})} + 2\text{H}_2\text{O}$	0.11	Acetic acid
$2\text{CO}_2 + 10\text{H}^+ + 10\text{e}^- \rightarrow \text{CH}_3\text{CHO}_{(\text{aq})} + 3\text{H}_2\text{O}$	0.06	Acetaldehyde
$2\text{CO}_2 + 12\text{H}^+ + 12\text{e}^- \rightarrow \text{C}_2\text{H}_5\text{OH}_{(\text{aq})} + 3\text{H}_2\text{O}$	0.09	Ethanol
$2\text{CO}_2 + 12\text{H}^+ + 12\text{e}^- \rightarrow \text{C}_2\text{H}_4_{(\text{g})} + 4\text{H}_2\text{O}$	0.08	Ethylene
$2\text{CO}_2 + 14\text{H}^+ + 14\text{e}^- \rightarrow \text{C}_2\text{H}_6_{(\text{g})} + 4\text{H}_2\text{O}$	0.14	Ethane
$2\text{H}^+ + 2\text{e}^- \rightarrow \text{H}_2$	0	Hydrogen
$2\text{H}_2\text{O} \rightarrow \text{O}_2 + 4\text{H}^+ + 4\text{e}^-$	1.23	Oxygen

Studies of electrochemical CO₂RR focused on the energy input and CO₂ conversion efficiency aspects and improving the selectivity and production rate as well. The first real studies with gaseous and liquid product quantification were reported by Yoshio Hori and co-worker in 1985 [25]. In this study, the catalytic activity of some polycrystalline metals electrodes was investigated in CO₂-saturated 0.1 M KHCO₃ using constant-current electrolysis. Metal electrodes can be categorized into four groups according to their major CO₂R products (**Table 2**) [26]. Pb, Hg, Tl, In, Sn, and Cd favor HCOOH production. Au, Ag, Zn, Pd, and Ga selectively produce CO, while HER is exclusively observed over Ni, Fe, Pt, and Ti. Cu shows a unique ability to catalyze the formation of hydrocarbon and oxygenates. Cu is thus the only pure metal that generates highly reduced products with > 2e⁻ transfer. As shown in **Table 2**, for all metals, a considerable overpotential is required to achieve the specified current density of 5 mA cm⁻². The formate-producing metals showed the largest overpotentials (for example, HCOOH with a

Faradaic efficiency (FE) of 97.4 % for Pb at -1.24 V vs. RHE). The smallest overpotential was achieved by Au, which produces CO with 87 % FE at -0.65 V vs. RHE.

Since then, several reports presented experimental and theoretical investigations of the catalytic properties of different metals. The selectivity has been explained by the binding energies of the key intermediates, including *COOH , *OCHO and *CO [27–30]. The initial electron transfer to CO_2 , forming $^*CO_2^-$ anion radical is thought to be the rate-determining step (RDS). The binding mode of $^*CO_2^-$ (the first surface-bound intermediate) on the metal surfaces is a key factor governing product distribution. The proton-coupled electron transfer can occur either on the carbon atom, resulting in an oxygen-bound intermediate *OCHO , or on the oxygen atom, resulting in a carbon-bound intermediate *COOH , further reduction step leads directly to $HCOOH$ and CO , respectively. **Figure 2** shows an adapted scheme about the proposed pathways for CO and $HCOOH$ formation during CO_2R [28].

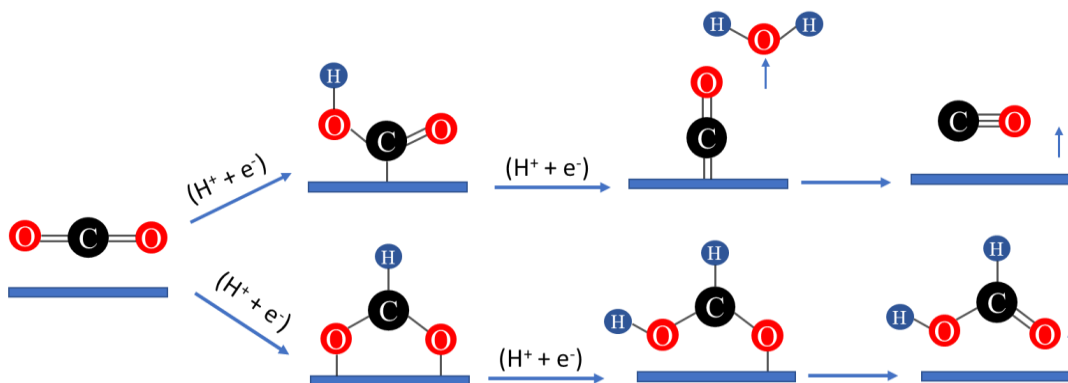


Figure 2. Pathways for the electrochemical reduction of CO_2 to CO and $HCOOH$ [28].

CO plays as the key intermediate toward the reduction of CO_2 to hydrocarbons and alcohols. Metals that bind CO very weakly are selective for CO_2 conversion to CO . As soon as CO is produced, it is released from the surface, and this inhibits the further reduction of CO to hydrocarbons and alcohols. On the other hand, metals that have a strong binding with CO produce mainly H_2 , where CO stays on the surface as a poison. Cu has intermediate *CO binding energy, this enables enough time for the surface-bound *CO to be coupled with nearby intermediates for C_2 and C_3 product formation or to be protonated to produce hydrocarbons and alcohols. Cu has positive adsorption energy for *H , which is crucial for the protonation of the intermediates. As a result, the suppression of HER is challenging [6]. The formate-producing

metals (Pb, Sn, In, Hg, and Cd) bind *CO and *H weakly. Sn appears near the top of the volcano curve plotted using the density functional theory (DFT) calculated *OCHO binding energy as a descriptor for CO₂R to HCOOH over a range of metals, suggesting that *OCHO is a key intermediate for CO₂R to HCOOH (HCOOH formation proceeds mainly through an oxygen-bonded intermediate, where there is no carbon-oxygen bond cleavage) [28].

Table 2. Faradaic efficiencies of CO₂ reduction products on metal electrodes in CO₂-saturated 0.1 M KHCO₃ (pH = 6.8) [26].*

Metal	E (V vs. RHE)	j _{total} (mA/cm ²)	Faradaic Efficiency (%)							Total (%)
			CH ₄	C ₂ H ₄	C ₂ H ₅ OH	C ₃ H ₇ OH	CO	HCOOH	H ₂	
Pb	-1.24	-5.0	0	0	0	0	0	97.4	5.0	102.4
Hg	-1.12	-0.5	0	0	0	0	0	99.5	0	99.5
Tl	-1.21	-5.0	0	0	0	0	0	95.1	6.2	101.3
In	-1.16	-5.0	0	0	0	0	2.1	94.9	3.3	100.3
Sn	-1.09	-5.0	0	0	0	0	7.1	88.4	4.6	100.1
Cd	-1.24	-5.0	1.3	0	0	0	13.9	78.4	9.4	103.0
Au	-0.65	-5.0	0	0	0	0	87.1	0.7	10.2	98.0
Ag	-0.98	-5.0	0	0	0	0	81.5	0.6	12.4	94.6
Zn	-1.15	-5.0	0	0	0	0	79.4	6.1	9.9	95.4
Pd	-0.81	-5.0	2.9	0	0	0	28.3	2.8	26.2	60.2
Ga	-0.85	-5.0	0	0	0	0	23.2	0	79.0	102.0
Cu	-1.05	-5.0	33.3	25.5	5.7	3.0	1.3	9.4	20.5	103.5
Ni	-1.09	-5.0	1.8	0.1	0	0	0	1.4	88.9	92.4
Fe	-0.52	-5.0	0	0	0	0	0	0	94.8	94.8
Pt	-0.68	-5.0	0	0	0	0	0	0.1	95.7	95.8
Ti	-1.21	-5.0	0	0	0	0	tr.	0	99.7	99.7

* Ethylene (C₂H₄), Propanol (C₃H₇OH)

For a better understanding of the CO₂RR mechanism and higher catalytic activity and product selectivity, increasingly research efforts have focused on exploring new types of catalytic active sites and structures. Various strategies such as altering crystal facets, changing morphologies, and modifying the crystal structure and the oxidation states have been investigated. In the following sections, we summarize some of these approaches and provide an overview of the recent trends in CO₂RR on monometallic NPs and discuss the key factors that affect the catalytic activities of the bimetallic catalysts.

2.4. Monometallic Catalysts

Pure metal NPs have been widely studied for electrochemical CO₂RR due to the high surface-to-volume ratio and the surface-to-mass ratio of NPs, which are advantageous for achieving high mass activity. Through the appropriate synthetic strategies and the characterization tools, as well as the computational simulation, the structure, morphology and the oxidation state can be tailored precisely. The particle size effect of some metal electrodes on their catalytic activities toward CO₂RR has been studied (e.g. Cu, Au, Pd, Ag) [31–35]. The CO₂R performance of Pd NPs with different sizes ranged from 2.4 to 10.3 nm was investigated [31]. The maximum FE_{CO} of 91.2% was achieved at – 0.89 V vs RHE on 2.4 and 3.7 nm particles, compared to 5.8% by using 10.3 nm particles at the same potential. Moreover, the turnover frequencies for CO formation within this size range showed a volcano-type curve. This suggests that tailoring the size of Pd could tune CO₂ adsorption, *COOH formation, and *CO desorption because of the varying ratio of the corner, edge, and terrace sites. DFT calculations indicated that the adsorption of CO₂ and *COOH was more favorable on the corner and edge sites than on the terrace sites of the Pd NPs, while HER on all sites was similar. Ag NPs also exhibited a volcano curve, where the current density increased firstly with decreasing the particle size from bulk to 5 nm and then decreased for particles <5 nm [32]. This volcano effect was attributed to the strong correlation between the key intermediates and the particle size.

Tuning the size of monodisperse Au NPs in the range of 4–10 nm showed that the highest CO FE of 90 % was achieved by 8 nm at – 0.67 V vs. RHE. Based on DFT calculations, the high edge (favor CO production) -to- corner (active for HER) sites ratio on the Au surface, the high the stabilization of *COOH, the key intermediate for CO production. Thus, the 8 nm Au NPs had the optimum ratio of edge sites over corner sites [33]. The size-dependent catalysis of

Au in CO₂RR to CO was further investigated by using micelle-synthesized Au NPs in the size range of 1–8 nm. The current density increased with decreasing the particle size, but the FE_{CO} showed the opposite trend. These higher current densities were associated to HER, which became more favorable over low-coordinate sites than CO₂RR [35]. In addition to the previous examples of noble metals, the size-dependent electrocatalytic reduction of CO₂ over Cu NPs was observed. Cu NPs in the mean size range from 2 to 15 nm showed that the current efficiency and product selectivity for CO and H₂ increased significantly rather than CH₄ and C₂H₄ selectivity, compared to Cu foil [34]. The increased population of low-coordinate sites on the surface of smaller Cu NPs, which bind CO₂, CO, and H atom strongly, is linked to the observed trends.

The morphology of monometallic NPs has a strong influence on surface structures, which could result in a tuned catalytic activity and product selectivity [36–38]. For example, Ag nano-coral electrocatalyst was synthesized by an oxidation-reduction approach in the presence of chloride ions in an aqueous medium. This structure exhibited a selective CO formation with 95% FE at a low overpotential ~ -0.37 V vs. RHE. The current density of 2 mA cm⁻² was achieved and remained stable for over 72 h. The activity increased by 32 times at -0.6 V vs. RHE, compared with Ag foil. The improved catalytic performance of the chloride-derived Ag nano-coral catalyst was attributed not only to the morphology effect (the increased electrochemically active area) but some insights were proposed into the role of the adsorbed chloride ions on the surface, resulting in an increase of the intrinsic activity for CO₂R and suppressing HER [36]. The porous structures help to increase the electrochemically active surface area and the mass transport for CO₂R. A nanoporous Ag catalyst was synthesized by a two-step de-alloying of Ag-Al precursor and investigated in CO₂RR. The catalyst generated CO with a FE of $\sim 92\%$ at moderate overpotentials of < 500 mV vs. RHE and exhibited a large increase in the electrochemical surface area and the catalytic activity by ~ 150 and ~ 20 times, respectively, compared to polycrystalline Ag. The improved catalytic activity may be due to the better stabilization of the key intermediates on the highly curved surface, and hence a lower thermodynamic barrier [37]. In another study, Ag-nanofoam catalysts were developed based on a concentrated additive and citrate-assisted metal deposition process [38]. The Ag foam exhibited a good activity and selectivity for CO formation at low and moderate overpotentials. The CO FEs are $\geq 90\%$ within a wide potential window ranging from -0.3 V to -1.2 V vs.

RHE and the corresponding CO partial current densities (j_{CO}) increased from -0.02 to -14.7 mA cm^{-2} . Most interesting is the ability to generate hydrocarbons at high overpotentials, reaching maximum FE_{CH_4} and $\text{FE}_{\text{C}_2\text{H}_4}$ of 51% and 8.6%, respectively at -1.5 V vs. RHE. This behavior was attributed to the stabilization of $^*\text{CO}$ on the Ag nanofoam surface, compared to the unmodified Ag foil. This results in a considerable increase of the $^*\text{CO}$ residence time, which is crucial to the further reduction steps (protonation to CH_4 and C-C coupling reaction for C_2H_4 evolution). For prolonged CO_2 electrolysis at -1.5 V vs. RHE, the degradation was observed and the FE_{CH_4} decreased to 32% within 5 h.

In addition to Ag, a top-down approach was employed using a controlled chemical etching of Cu nanocubes to get different shapes. The nanocrystals that were etched for 12 h or more showed a rhombic dodecahedral shape with enriched exposure of (110) facets. These particles exhibited a three-fold higher current density than Cu nanocubes and enhanced selectivity to hydrocarbons rather than CO at -0.8 V vs. RHE [39]. The stability of Cu nanocubes was addressed in another study, in terms of both activity and retaining the synthesized shape. The CO_2RR was performed together with product distribution and the morphology changes were monitored ex-situ using transmission electron microscopy (TEM) after different electrolysis times up to 12 h. For long electrolysis measurements, the HER activity increased and CO_2R activity decreased, and the morphology changes became obvious [21]. Additionally, octahedral Pd NPs exhibited better activity and higher selectivity toward CO formation than Pd nanocubes [40]. These improvements were attributed to a decrease in the CO binding energy on the Pd (111) surfaces of the octahedral structures.

The activity of 1D and 2D morphologies has also been studied and their potential for CO_2RR was investigated. For example, ultrathin 2 nm wide Au nanowires (NWs) with different aspect ratios were synthesized using a seed-mediated growth method. Longer NWs were much more active, where 500 nm long NWs catalyzed the CO_2RR to CO at an onset potential of -0.2 V vs. RHE. The FE_{CO} reached 94% at -0.35 V vs. RHE and remains stable for 7 h [41]. The DFT calculations suggested the higher density of active edge sites (have better CO selectivity) on NWs and the weak CO binding energy are the possible reasons for the improved catalytic activity. Hexagonal Pd nanosheets with 5 atomic thickness and 5.1 nm edge length were synthesized with uniform morphology. The Pd nanosheets generated CO with 94% FE at -0.5

V vs. RHE without any noticeable activity change. This performance was attributed to the high edge sites density on hexagonal Pd nanosheets, compared to Pd NPs [42]. Furthermore, ultrathin bismuth nanosheets with single crystallinity and enlarged surface area were prepared via the in situ topotactic transformation of bismuth oxyiodide nanosheets. The catalyst showed a selective and efficient CO_2R to HCOOH with $> 95\%$ FE at -1.5 V vs. RHE and a stable current density of 15 mA cm^{-2} for 10 h. The high selectivity for CO_2RR to HCOOH was attributed to the better stabilization of $^*\text{OCHO}$ on Bi (001) surface, compared with $^*\text{COOH}$ or $^*\text{H}$ [43].

The CO_2R performance of a metal surface showed a strong dependence on the size, morphology and surface structure. A simple approach was employed to improve the catalytic activity of polycrystalline metals, which is the reduction of a thermally or an electrochemically oxidized metals results in the formation of metal nanostructures, known as oxide-derived metal catalysts. This oxidation/reduction process is represented in **Figure 3**.

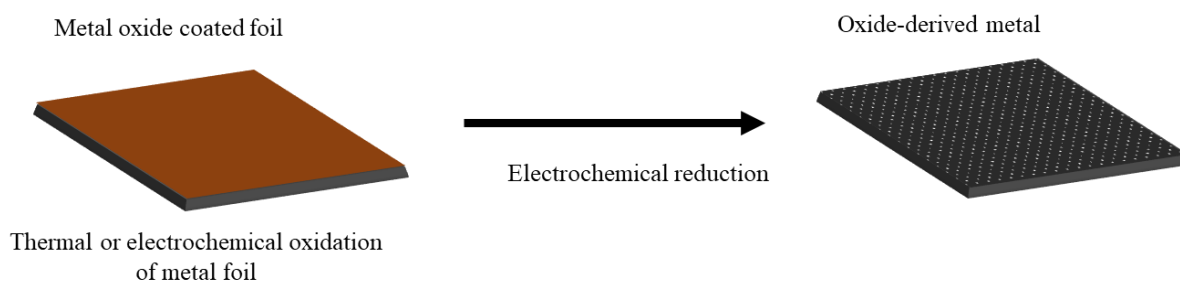


Figure 3. Oxide-derived metal electrode formation.

Nanostructured Au was prepared by anodization of an Au foil followed by a reduction step. The oxide-derived Au NPs exhibited a higher selectivity for CO production at lower overpotential and retain their activity for ~ 8 h, compared to the polycrystalline and other nanostructured Au electrodes. The enhanced activity of oxide-derived Au was directly associated with the density of grain boundaries created by the oxidation/reduction step and thus higher stability of $\text{CO}_2^{\bullet-}$ intermediate [44]. The Oxide-derived Pb has up to 700 times lower H^+ reduction activity relative to Pb foil, resulting in a high FE for CO_2R to HCOOH [45]. Such activity of p-block metals was explained by the presence of a metastable surface oxide/hydroxide layer, that suppress HER, but is active for CO_2RR over prolonged electrolysis. A modified Cu electrode was prepared by annealing Cu foil in air atmosphere at 500 °C for 12

h followed by electrochemical reduction of the resulting thick Cu_2O layer. A stable total current density of 2.7 mA cm^{-2} was obtained at -0.5 V vs. RHE and remained for 7 h, compared with fast deactivation for the commercial Cu foil and low-temperature annealed Cu foils [46]. In another study, Cu NWs were prepared by oxidation-reduction of Cu mesh. These oxide-derived nanostructures with rough surface generated mainly HCOOH and CO with a current density of -17 mA cm^{-2} at -0.9 V vs. RHE [47]. Generally, this oxidation-reduction approach provided an efficient and effective way for growing nanostructures on the surface of a variety of transition metals [48–50].

It was very important for the research community to understand the activity and selectivity of pure metals, and figure out the existing challenges: (1) high CO selectivity is associated with expensive noble metal catalysts; (2) catalysts, that generate HCOOH suffer from low current densities and high overpotentials; (3) poor selectivity of hydrocarbons producing metal surfaces. These findings suggest that tuning the binding energy of the potential intermediates on the metal surface might overcome the above limitations.

Moving beyond pure metals, bimetallic NPs provide an ideal platform for studying the effect of surface composition [51,52] and to identify how to bypass the scaling relations [53,54]. Through appropriate synthesis procedures, a wide range of combinations (with various compositions, patterns of mixing, geometric structures, and intermetallic phases) can be explored (**Figure 4**). Such materials can provide multiple active sites for reaction intermediates with tunable binding strength and thus exhibit altered reactivity relative to their monometallic counterparts. In the first study, a number of Cu-based catalysts were surveyed. These Cu-X bimetallic catalysts ($X = \text{Ni, Pb, Sn, Zn, Cd, and Ag}$) exhibited a selective reduction of CO_2 to CH_3OH , HCOOH, and CO at low overpotentials, and demonstrated enhanced activity than that of the parent metals [55]. The presence of a second element can significantly modify the catalytic performance in different ways: (1) modifying the electronic surface structure, which influences the binding energy of intermediates; (2) introducing strain effect; (3) the geometric effect, which stems from the atomic arrangement at the active sites and (4) acting synergistically for CO_2R . There are ample examples in the literature on using bimetallic catalysts in CO_2RR , which highlight the potential of the bimetallic systems to enhance and/or create unique activity relative to their parent metals. In the next section, we provide an overview and discussion about

different bimetallic systems, focusing much on the Au-based bimetallic systems, and then briefly summarize the systems that contain either Sn, Ag or Pb.

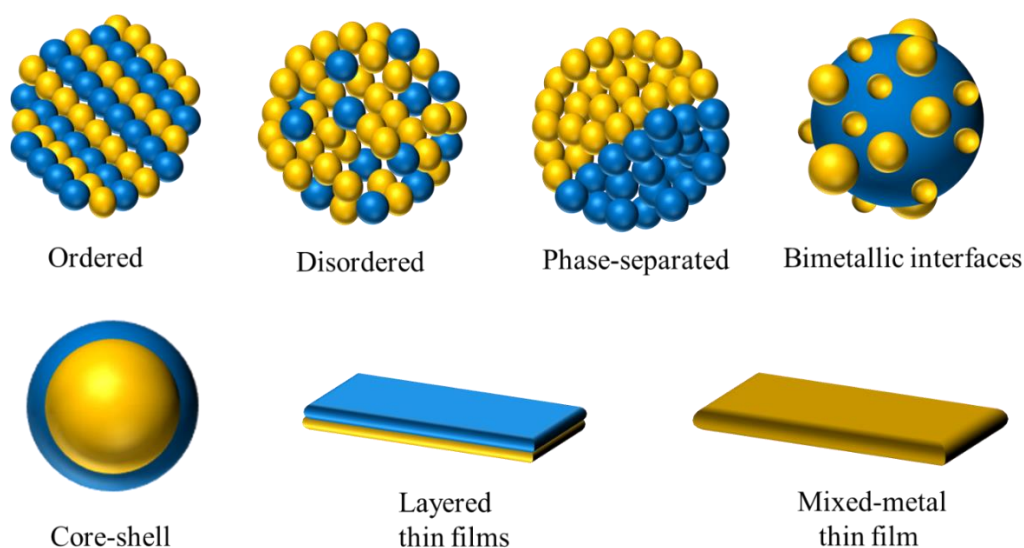


Figure 4. Schematic illustration of various mixing patterns and geometric structures of bimetallic electrocatalysts.

2.5. Gold-Based Bimetallic Systems

Au is one of the most stable and active catalysts for selective CO₂ conversion to CO [44]. The weak binding energy of CO inhibits the further reduction to hydrocarbons and alcohols. Furthermore, the activation of CO₂ molecules to *COOH on the Au surface has a high energy barrier. Therefore, the introduction of a second metal, which adsorbs the key intermediate (*CO) with different binding energies could effectively tune product distribution on the Au-based catalysts.

2.5.1. Combination with Moderate CO-Binding Metal

The combination of Au with Cu metal for its unique and moderate binding energy to CO has been widely studied. Some electrodes have shown improved selectivity and higher intrinsic for producing CO, while other bimetallic catalysts have demonstrated high activity and selectivity for multi-carbon products. Au-Cu bimetallic NPs in alloy form were synthesized prior to assembly on thin films (monolayers) for CO₂ reduction. The addition of copper atoms into gold structure resulted in the appearance of new products (CH₄ and C₂H₄), as expected, but a volcano-shaped CO-formation activity with a peak for the Au₃Cu catalyst was observed. The analysis of the surface valence band spectra revealed the d band center gradually shifts downwards from

Cu to Au and suggested that the activity/selectivity of the bimetallic compositions is linked to the electronic modification, together with the geometric effects (arrangements of metal atoms) affecting the binding energy of the key intermediates [52]. The shell-thickness dependence of the electrochemical CO₂ reduction was investigated on Au@Cu core-shell NPs. On cubic gold NPs with 7–8 layers of copper, hydrogen, and ethylene formed with higher selectivity, while with more than 14 layers of copper, the particles became more selective towards the production of hydrogen and CH₄. This trend was attributed to the catalyst composition, surface structure and strain effects [56].

The influence of surface defects (vacancies) on the catalytic activity and selectivity was investigated using de-alloyed Au₃Cu nanocubes. The vacancies were created by the treatment with acetic or nitric acid for different times to etch the superficial Cu atoms. De-alloyed Au₃Cu showed a considerable low CO onset potential and a 90.2% FE_{CO} at -0.38 V vs. RHE, compared to Au₃Cu alloy and Au NPs. Based on the computational studies, the improved performance was attributed to the stabilization of *COOH, the key intermediate for CO [57]. Electrodeposited Au-Cu alloys on nanoporous Cu film were synthesized with different compositions and exhibited an improved activity towards alcohol formation relative to pure Cu. Among the different compositions, the Cu_{63.9}Au_{36.1} generated CH₃OH with a FE of 15.9%, which is about 19 times that of pure Cu, and FE_{C₂H₅OH} increased to 12%. The incorporation of Au into Cu alloys favors alcohol production over HCOOH and suppressed HER. This revealed that the multifunction catalysis of the Au-Cu alloys could assist in improved alcohol formation [58].

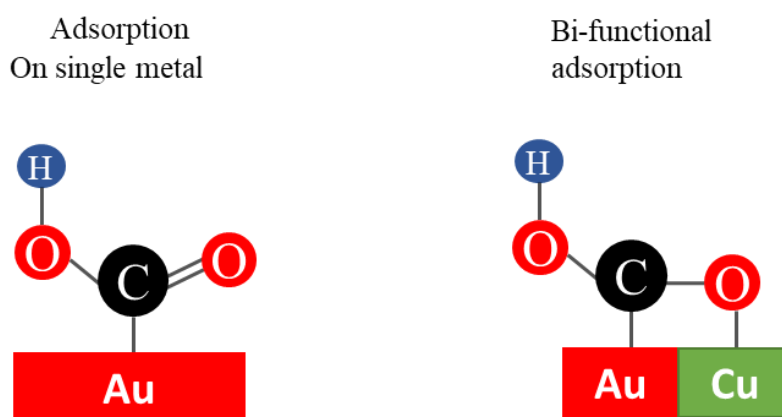


Figure 5. Schematic diagram of the bi-functional interface effect and stabilization of *COOH intermediate [59].

Au-based catalysts with bi-functional interface were developed to reduce the amount of precious metal and achieve an improved CO₂R, compared to pure metal. Au metal is combined with oxophilic metals to form a bimetallic interface rather than alloys. Among the oxygen-affinity metals, Cu metal was chosen due to the moderate binding energies of *COOH and *CO on the Cu, and Cu binds *O more strongly than Au for the further stabilization of *COOH through the oxygen-metal interaction, this bi-functional interface effect is shown in **Figure 5** [59].

In a few recent reports, they directly linked the observed improvement in C₂₊ products' activity and selectivity to a CO spillover effect [60,61]. Cu-Au catalysts were synthesized by the deposition of Au NPs on Cu₂O NWs by the galvanic replacement. After the electrochemical pre-reduction step, Cu₂O derived Cu-Au catalysts exhibited improved selectivity towards C₂₊ products with a FE of ~70% at -1.05 V vs. RHE, which is higher compared with 55% generated on Cu₂O derived Cu catalyst at the same potential. This behavior was attributed to the flow of the generated CO on Au sites to the adjacent Cu surface. This configuration increased the CO coverage on Cu and led to a further reduction of the CO to higher hydrocarbons and suppress the HER [60]. Other metallic Cu-Au combinations have been investigated for CO₂R, a polycrystalline Cu foil decorated with Au NPs (Au/Cu) The Au/Cu bimetallic catalyst synergistically reduced CO₂ to > 2 e⁻ reduction products at rates more than 2-fold higher than the constituent metals. The alcohol products were generated at 265 mV more positive potentials on the Cu/Au catalysts relative to Cu. A sequential catalysis mechanism for the production of alcohol was proposed [61]. A control experiment was performed on the Au_{0.01}Cu_{0.99} alloy surface, which did not reproduce the observed trend of alcohol production at low overpotentials. These results support the hypothesis of the sequential catalysis mechanism over two separate metals operate in close vicinity. It was also reported on the selective formation of C₂H₅OH over Au-Cu alloy NPs supported Cu submicrometer-cone arrays The FE_{C₂H₅OH} reached ~29 %, while the ethylene formation is relatively suppressed to ~16% at - 1.0 V vs. RHE. The ratio between the partial current densities of C₂H₅OH and C₂H₄ can be tuned from 0.15 ± 0.27 to 1.81 ± 0.55 by varying the Au concentration. The experimental and DFT calculations revealed the importance of Au in tuning the key intermediates binding energy at the interface and consequently modify the activity and selectivity [62].

Furthermore, the systematic atomic ordering control played an important role in the catalytic performance of Au–Cu alloy NPs. Atomically ordered AuCu NPs selectively reduced CO₂ to CO achieving a FE of 80%, whereas disordered AuCu NPs favored the HER, which was assigned to the formation of compressively strained three-atomic gold layers over the intermetallic core [63]. In another study, by coating the Cu NWs with a thin Au layer, the current density increased slightly. That catalyst generates only H₂ and CO in the whole potential range with a total FE of 100%. At – 0.50 V vs. RHE, a FE_{CO} of 11% was achieved, and reaching a maximum of 33 % at a potential of – 0.65 V vs. RHE, then decreases with a further increase of the overpotential. The low FE_{CO} observed over Au coated Cu nanowires was attributed to the pattern of this bimetallic system, which is layered thin films. The Au coating might not cover the whole Cu wires and possess some defects. The presence of Cu beneath the Au coating might facilitate the HER. At – 0.65 V vs. RHE, the CO/H₂ ratio of 1:2 remains stable for 24 h of electrolysis, the current density decayed from –14 to –8 mA cm⁻² during the first 3 h, and then became stable [64].

The above mentioned Au-Cu electrodes represent different types of bimetallic geometric structures (mixed-thin films, layered thin films, alloy, and core-shell NPs) and mixing patterns (ordered, disordered, and phase-separated) that can influence the selectivity and activity of the catalyst by modulating the adjacent binding sites. Investigations of monolayers of alloyed NPs have considered that all the constituent metals participate in bonding with the intermediates, however, in other bimetallic patterns, only one site is active or exposed to the reactants, such as layered thin films and core-shell NPs (metal on metal structure). The binding energy of CO, oxide-derived nature of Cu and phase boundaries are critical factors in the catalytic performance of these systems. The generated CO with high concentration nearby Cu sites, where CO is further reduced to hydrocarbon and oxygenates. The C–C coupling process is considered to be more favorable on oxide-derived Cu catalysts due to the grain boundaries, defects, lower coordinate sites, surface/subsurface oxygen or residual Cu⁺ species [65,66]. The phase-separated Au-Cu electrocatalysts showed the best activity towards C₂₊ alcohols superior to Au, Cu or Au-Cu alloys, this was attributed to the more stabilization of the intermediates at the Au/Cu interface, where a sequential catalysis mechanism was proposed by decoupling the multiple reduction steps during CO₂R, which is not possible on monometallic surfaces. The

insights gained from the Au/Cu catalysts motivate the development of a high surface area catalyst to produce long-chain alcohols and to investigate other bimetallic systems as well.

2.5.2. Combination with Strong CO-Binding Metal

Pd binds CO strongly and has a higher affinity to oxygen than Au [67], resulting in more stabilization of the reaction intermediates such as *COOH via bidentate interaction. The increase of the binding strength of the intermediates to the alloy surface is one of the proposed ways to break the scaling relations. Previous reports on AuPd alloys show that they have a strong ligand effect which can cause an averaging of their CO binding energies (strengthening the CO binding energy to Au sites and simultaneously weakening the binding energy of CO to Pd sites) [68]. This bimetallic system has been widely studied for many heterogeneous and electrocatalytic reactions [69], but a few reports are found on CO₂RR. Au-Pd alloy thin films are more selective to HCOOH production, relative to pure Au and Pd [70]. Pd-Au overlayers were prepared by electrodeposition of Pd on a Au substrate and catalyzed the formation of C₁ to C₅ hydrocarbons [71]. The core-shell structures with different shell thicknesses and compositions were developed and evaluated for CO₂RR, Au-Pd core-shell NPs showed that the catalytic activity and product distribution are linked to the Pd shell thickness. As the shell thickness was increased from 1 to 10 nm, hydrocarbon and formate were also formed, besides CO and H₂ [72]. The former two examples showed the formation of >2e⁻ reduction products on Cu-free electrocatalysts. Another core-shell NPs consisting of bimetallic core and an ultrathin Pd-rich shell exhibited an improved CO selectivity for all compositions compared to pure Au and Pd. By controlling the Au:Pd atomic ratio, the shell thickness and compositions can be tuned. With increasing the Au content, the FE_{CO} increases at lower overpotentials. A maximum of 96.7% was obtained at - 0.6 V vs. RHE for Au₇₅Pd₂₅ [73]. Alloying Au with different compositions of Pd on a smooth thin film surface was found to suppress hydrogen evolution by increasing the CO₂RR intermediate (*CO) coverage at lower overpotentials [51].

Au-Pt alloys with different compositions were prepared by magnetron sputtering co-deposition technique as a first systematic exploration of alloying Au with Pt, which binds CO strongly and generates mainly H₂. The syngas (CO/H₂) ratio showed a good tunability, which was attributed to the linear change in the binding strength of *COOH and *CO intermediates [74]. The variation of the electronic properties caused by adjusting the binary composition

cannot tune the binding strength of a certain intermediate without modifying others for a selective and a high CO₂ reduction performance. So, the geometric effects are also important to the catalyst design.

2.5.3. Combination with Weak CO-Binding Metal

Au, Ag, and Zn all bind CO weakly and produce mostly CO, so as soon as CO is produced, it desorbs and cannot go on further to form highly reduced products. Au-Ag bimetallic alloys and core-shell structures were designed and explored in photocatalytic [75]. and electrocatalytic reactions [76–78]. The catalytic activity of these structures has not received considerable attention towards electrochemical CO₂RR. There are a few studies about the plasmon-induced photocatalytic CO₂R under visible light irradiation. Au-Ag alloys co-decorated TiO₂ NWs (Au-Ag alloy/TiO₂ NWs) exhibited an enhanced photocatalytic activity and selectivity to CO formation, compared to Au/TiO₂, Ag/TiO₂ or pure TiO₂ NWs [79]. Moreover, the Au-Zn combination has not been employed in CO₂R yet. Ag-Zn catalysts (as Cu-free electrodes) reduced CO₂ to > 2e⁻ reduction products. Pulse-deposited Zn dendrites on a Ag foam catalyzed the formation of CH₃OH with a FE ≥ 10.5 % at a total current density of - 2.7 mA cm⁻² [80]. In another study, Ag-Zn alloy foil produced CH₃OH and CH₄ at -1.43 V vs. RHE with five-fold and three-fold higher FEs than those generated on pure Ag and Zn surfaces, respectively. Although the above results demonstrate the potential of the Ag-Zn combination in CO₂RR, the systematic investigation of alloying Au with Ag or Zn in CO₂R performance is still lacking.

2.5.4. Combination with Formate-Producing Metal

Synthesis of bimetallic electrodes containing p-block metals (such as Sn, In and Pb, all having high H₂ overpotential and favor HCOOH production) is a good strategy not only to tune the CO₂RR activity and selectivity but also to suppress HER [45]-[81,82]. A Sn/SnO_x electrode exhibited an 8-fold higher partial current density and 4-fold higher FE_{HCOOH} than the respective Sn foil [83]. Sn and Pb metals have been extensively mixed with Cu and exhibited a tunable selectivity between CO and HCOOH. Briefly, A Cu-Sn bimetallic alloy resulted in the selective reduction of CO₂ to CO with a FE ≥ 90% at - 0.6 V vs. RHE [84]. Cu/SnO₂ core-shell NPs showed thickness-dependent CO₂ reduction properties: the thicker shell (1.8 nm) acted like SnO₂ NPs and HCOOH was the major product, whereas the thinner shell (0.8 nm) was selective towards CO formation with a FE = 93% [85]. A Pb-adatom-decorated Cu foil (0.78 monolayer

Pb/Cu catalyst) effectively suppressed the HER 652-fold compared to Cu foil, and generated HCOOH with a FE of $70.5 \pm 0.7\%$ at -1.25 V vs. RHE [86]. Alloying Ag with Sn was investigated for CO₂ reduction. Ag-Sn NPs, having a bimetallic core and a thin partial oxide shell with tunable thickness (Ag-Sn/SnO_x), exhibited a volcano-type curve between FE_{HCOOH} and bulk Sn content (80 % FE_{HCOOH} and j_{HCOOH} of -16 mA cm⁻² at -0.8 V vs. RHE) [87]. From the above results, the combinations with formate-producing metals in alloy or core-shell form exhibit unique properties than those of the parent metals in terms of CO-binding energy, higher activity towards HCOOH production, and suppression of the HER. Still, beyond the above examples, the combinations of p-block metals with Au have not been studied. This is indeed surprising.

2.6. Non-Au-Based Bimetallic Systems

Cu-Ag combinations with different forms, including alloy, phase-separated, and phase-blended bimetallic have been synthesized and investigated as catalysts for CO₂RR. Bimetallic Cu-Ag thin films have been reported to suppress HER and exhibit higher selectivity for C₂₊ oxygenates through various means [88,89]. In the first example, Cu-Ag surface alloys prepared by arc melting of physically mixed Ag and Cu under Ar atmosphere, rapid quenching in deionized water, and cold rolling into foils, leading to compressive strain on Cu surface atoms. The valence band structure of Cu shifted to lower levels, and hence weakened the binding strength of *H. This resulted in selective suppression of HER by 60 – 70 % and a 10 – 15 % increase in the oxygenates formation. Mainly acetate and acetaldehyde (these are minor products <1% on pure Cu) This adjusted selectivity is attributed to reduced rates of C–O bond cleavage stemming from the decreased coverage of adsorbed hydrogen. and the reduced oxophilicity of the compressively strained Cu [88]. This was attributed to the considerable bulk-phase miscibility between Ag and Cu obtained in these films. Ag weakly binds hydrogen compared to Cu [27], so the incorporation of Ag into Cu catalysts, resulting in a lower *H surface coverage and consequently suppress the HER rates and hydrogenation of CO₂R intermediate to hydrocarbons.

Similar to Au/Cu bimetallic systems, the development of a Ag incorporated Cu₂O (Ag-Cu₂O) catalyst (phase-separated and phase-blended), leads to the suppression of H₂ evolution and modulating the selectivity of C₂H₅OH formation. The phase-blended Ag-Cu₂O showed a 34.15% FE_{C₂H₅OH} at -1.2 V vs. RHE which is three-fold higher than that of the Cu₂O at the same

potential. Besides the role of Ag sites to provide a higher concentration of CO near Au/Cu surface, the population of Ag-Cu biphasic boundaries is also considered to be critical in the determination of the ethanol selectivity [90]. The sequential catalysis mechanism and the CO spillover from Ag to Cu sites were discussed in the phase-separated Cu-Ag alloy. This oxide-derived catalyst was prepared via the galvanic replacement reaction between Ag precursor and Cu₂O NWs. At -1.05 V vs. RHE, this bimetallic generated C₂₊ products with a 76 % FE, while the oxide-derived Cu₂O exhibited only 58%. Particularly, the FE_{C₂H₄} increased from 33% to 52% after Ag incorporation into the Cu₂O NWs.

Sn-Pb alloys showed higher electrical conductivities compared to pure phases of the parent metals. Among the different compositions, Sn_{56.3}Pb_{43.7} exhibited the highest FE_{HCOOH} and j_{HCOOH} of 80 % and 45.7 mA cm⁻² at -1.36 V vs. RHE, respectively, which is about 20% more than those measured for Pb or Sn electrodes. It is supposed that the presence of SnO_x and Pb⁰ on the surface improves the electrical conductivity and catalytic activity of the alloys and facilitates the selective reduction of CO₂ to HCOOH [91]. Pd-Sn nanoalloys selectively generate HCOOH, and the CO formation and HER were suppressed at a low overpotential of -0.26 V. The catalytic activity and selectivity are correlated to the relative content of Pd⁰/Pd²⁺. DFT calculations suggest that the surface configuration of Pd-Sn-O stabilized *OCHO the key intermediate and favors the formation of HCOOH [92]. A few recent studies demonstrated the formation of highly reduced products (> 2e⁻ transfer) using electrocatalysts that do not contain copper. In addition to the Ag-Zn [80] and Au-Pd [72] catalysts that we mentioned previously, nickel (Ni)-gallium (Ga) films with different phases were prepared and tested [93]. Ni₅Ga₃ alloy catalyzed the formation of CH₄, C₂H₄, and C₂H₆ with a total FE of ~ 4%. Ni₃Al and Ni₃Ga intermetallic compounds also generated C₂ and C₃ products [94]. The activity descriptors (i.e., overpotential, current density, and product distribution) of the bimetallic nanoparticles were summarized in **Table 3**.

Table 3. Comparison of various bimetallic catalysts in the literature studied in CO₂ reduction.*

Catalyst	Preparation	state	Electrolyte	Loading ($\mu\text{g cm}^{-2}$)	j (mA cm^{-2})	E (V) vs. RHE	Faradaic Efficiency (%)	Ref.
Au ₃ Cu	Coreduction	alloy/monolayer	CO ₂ -std. 0.1 M KHCO ₃ (pH = 6.8)	7.66	~-2	-0.73	CO = 65	[52]
Au@Cu1	Two-step reduction	Au@Cu1 Core-shell	CO ₂ -std. phosphate buffer (pH = 8.0)	N/A	~-10	-0.6	CH ₄ ~5, C ₂ H ₄ = ~20 Conc. _{HCOOH} = 45 mM mg ⁻¹ _{catalyst} @ -1.0 V	[56]
Au@Cu2	Two-step reduction	Au@Cu2 Core-shell	CO ₂ -std. phosphate buffer (pH = 8.0)	N/A	~-10	-0.6	CH ₄ ~12, C ₂ H ₄ = ~5 Conc. _{HCOOH} = 13 mM mg ⁻¹ _{catalyst} @ -1.0 V	[56]
De-Au ₃ Cu	Coreduction + Surface etching	alloy	CO ₂ -std. 0.5 M KHCO ₃ (pH = 7.2)	N/A	j _{CO} = -40. j _{H₂} = 2	-0.38	CO = 90.2	[57]
Cu _{63.9} Au _{36.1}	Electrodeposition	alloy	CO ₂ -std. 0.5 M KHCO ₃ (pH = 7.6)	N/A	~-4	-1.0	CH ₃ OH = 15.9 C ₂ H ₅ OH = 12	[58]
Ordered-AuCu	Coreduction	alloy	CO ₂ -std. 0.1 M KHCO ₃ (pH = 6.8)	4.0	j _{CO} = -1.39	-0.77	CO = 80	[63]
disordered AuCu	Coreduction	alloy	CO ₂ -std. 0.1 M KHCO ₃ (pH = 6.8)	4	j _{CO} = -0.43	-0.77	CO = 34	[63]
Au _{0.55} Pd _{0.45}	e-beam codeposition	alloy	CO ₂ -std. 0.1 M KHCO ₃ (pH = 6.8)	N/A	j _{HCOOH} = -0.43	-1.0	CO = 40 H ₂ = 37 HCOOH = 7	[70]
Pd-Au	electrodeposition	Pd overlayers on Au	CO ₂ -std. phosphate buffer (pH = 6.7)	N/A	N/A	-1.4	C1 - C5 hydrocarbons total FE = 3.23	[71]
Au-Pt	Magnetron sputtering		CO ₂ -std. 0.1 M KHCO ₃ (pH = 6.8)	N/A	N/A	-0.65	Tunable syngas ratio	[74]
Cu-Au	Galvanic replacement	Au NPs at Cu wires	CO ₂ -std. 0.1 M KHCO ₃ (pH = 6.8)	N/A	~-42.87	~-1.05	C ₂ products = 77	[60]

Cu-Au	Au sputtering on Cu NWs	Core-shell	CO ₂ -std. 0.5 M KHCO ₃ (pH = 7.2)	N/A	-14	-0.65	CO = 33	[64]
Pd-Au	Electrodeposition of Pd on Au foam	Pb/Au	(0.1 M KH ₂ PO ₄ /0.1 M K ₂ HPO ₄)	N/A	-7	-1.4	C1-C5 = 3	[71]
Au@Pd	Two-setps colloidal method	Core-shell	CO ₂ -std. 0.1 M Na ₂ SO ₄ (pH = 4.0)	N/A	N/A	-0.5	HCOOH = 27	[72]
Au ₇₅ Pb ₂₅	One-step reduction	Core (alloy)-shell (Pb)	CO ₂ -std. 0.5 M KHCO ₃ (pH = 7.2)	83.9	-10	-0.5	CO = 96.7	[73]
Cu-Sn	Electrodeposition of Sn on oxide-derived Cu	alloy	CO ₂ -std. 0.1 M KHCO ₃ (pH = 6.8)	N/A	-1.0	-0.6	CO ≥ 90	[84]
Ag ₇₆ Sn ₂₄	Galvanic displacing of Sn with Ag	Core (alloy) – shell (SnO _x)	CO ₂ -std. 0.5 M NaHCO ₃ (pH = 7.2)	1000	-19.7	-0.8	HCOOH = 80	[95]
Cu/SnO ₂ (0.8)	Seed-mediate growth	Core-shell	CO ₂ -std. 0.5 M NaHCO ₃ (pH = 7.3)	40000	-4.6	-0.7	CO = 93	[85]
Cu/SnO ₂ (1.8)	Seed-mediate growth	Core-shell	CO ₂ -std. 0.5 M NaHCO ₃ (pH = 7.3)	40000	N/A	-0.9	HCOOH = 85	[85]
Au@Cu1	Seed-mediate growth	Au@Cu1 Core-shell	CO ₂ -std. phosphate buffer (pH = 8.0)	N/A	N/A	-1.0	Conc. _{HCOOH} = 45 mM mg ⁻¹	[56]
Cu ₈₇ -Sn ₁₃	Electrodeposition	alloy	CO ₂ -std. 0.1 M KHCO ₃ (pH = 6.8)	N/A	~ -1.5	-0.99	CO = 60	[96]
Cu ₅₅ -Sn ₄₅	Electrodeposition	alloy	CO ₂ -std. 0.1 M KHCO ₃ (pH = 6.8)	N/A	~ -2.7	-1.1	HCOOH = 90	[96]

*std: saturated

3. Motivation and Aims

Recent research has shown that the electrochemical CO₂RR is a potentially attractive approach to close the energetic carbon cycle because it provides a convenient means of storing electricity from intermittent energy sources such as solar and wind in high-energy-density form. The electrochemical conversion of CO₂ can generate a variety of valuable carbon-based chemicals with high current efficiency under ambient conditions. These products can be used as feedstocks for chemical synthesis or converted to hydrocarbon fuel. The investigation of the electrocatalytic activity of different materials toward CO₂ reduction has been carried out in our research group, including metal NPs, conducting polymers and metal-nitrogen doped carbon-based catalysts. Within the group, those who focused on CO₂ conversion and worked particularly to perfect the experimental methods and compare the activity of the different materials. This resulted in a robust protocol to measure the catalyst activity through improving the electrochemical cell configuration for better product detection and quantification. It was good to benefit from their initial work and from their insights into electrochemistry and catalysis. The advantage of alloying and tuning the electronic and geometric structures of the bimetallic catalysts inspired us to contribute to the development of bimetallic catalysts for CO₂R.

Here, we aimed to provide a systematic study of the electrocatalytic activity of Au-based bimetallic NPs toward CO₂R. We carefully surveyed the literature and decided to explore the combination of Au with Sn, Pb, and Ag, as three bimetallic systems which have not been employed in CO₂R yet. During my research, we aimed to find answers to the following questions:

- *Is it possible to combine Au with p-block metals (Sn and Pb) with different compositions?*
- *What is the structure (e.g., alloy, nanocomposite, or new intermetallic phase) of these systems?*
- *How does the combination of p-block metals (Sn and Pb) with Au NPs affect the catalytic performance and product distribution?*
- *Is the native oxide layer of the p-block metals stable under the reduction conditions, and if yes, how does it affect the product distribution?*
- *Could the surface electronic properties alone determine the electrocatalytic performance of Au-Ag alloys?*

As a first step, our goal was to develop a direct and reproducible approach to synthesize Au-Sn NPs with tunable composition, and well-defined morphology. In the next step, we studied

the catalytic activity of the Au-Sn NPs, investigating the effect of the phase composition in CO₂RR. Further, we introduced a new synthetic approach to prepare Au-Pb catalysts to explore the effect of replacing Sn with Pb on the catalytic activity and product distribution, we also tried to uncover the role of Au/Pb interfaces in the electrocatalytic CO₂R as well as to elucidate the stability of the native sub-stoichiometric oxide under the reduction conditions. A series of Au-Ag alloy NPs with different compositions and narrow-size distribution was prepared, as a good model to investigate the correlation between the surface electronic properties and the catalytic activity in CO₂R.

4. Experimental

This chapter describes the synthesis and morphological and structural characterizations of the three studied Au-based bimetallic systems (Au-Sn, Au-Ag, and Au-Pb). A description of the electrochemical cell that was used to carry out CO₂RR experiments is given together with the product detection and quantification. The preparation of the working electrodes and the post-treatment steps are mentioned. We also discuss the electrochemical measurements, in situ Raman spectroelectrochemistry, and the theoretical calculations.

4.1. Materials

Synthesis of Au-based bimetallic NPs

- Gold (III) chloride trihydrate (HAuCl₄·3H₂O, 99.9%, Aldrich)
- Tin (IV) chloride pentahydrate (SnCl₄·5H₂O, 98%, Honeywell/Fluka)
- Sodium citrate monobasic anhydrous (C₆H₇NaO₇, 99.5%, Fluka)
- Sodium citrate dihydrate (C₆H₅Na₃O₇·2H₂O, 99%, Aldrich)
- Sodium borohydride (NaBH₄, 99%, Aldrich)
- Poly(vinylpyrrolidone) (PVP, M_w = 40 000, Fluka)
- Silver nitrate (AgNO₃, 99.9%, Molar)
- Tannic acid (C₇₆H₅₂O₄₆, ACS reagent, Aldrich)
- Lead (II) nitrate (Pb (NO₃)₂, ≥99.0%, AnalaR NORMAPUR, Reag. Ph. Eur., ACS)
- L-Ascorbic acid (C₆H₈O₆, ≥99 %, ACS reagent)

All reagents were used without further purification. Solutions were prepared using ultrapure deionized water (Millipore Direct Q3-UV, 18.2 MΩ cm). All glassware was cleaned with aqua regia.

Electrochemical characterization and product quantification

- Sodium sulfate (Na₂SO₄, ≥ 99% VWR)
- Sodium hydrogen carbonate (NaHCO₃, 99.7, VWR)
- Potassium hydrogen carbonate (KHCO₃, 99.7, VWR)
- Deuterium oxide (D₂O, 99.9 atom% D, Sigma-Aldrich)
- Phenol (C₆H₆O, 99.5%, Sigma-Aldrich)

- Isopropanol (C₃H₈O, 99%, VWR)
- Acetone (C₃H₆O, 99.5%, VWR)
- Ethanol (C₂H₆O, 99%, VWR)
- Dimethyl sulfoxide (DMSO, C₂H₆SO, 99.8% Alfa Aesar)
- Carbon dioxide (¹³CO₂, 99 atomic% ¹³C, Sigma-Aldrich)
- NaH¹³CO₃ (98 atomic% ¹³C, <3 atom% ¹⁸O, Sigma-Aldrich)
- KH¹³CO₃ (98 atomic% ¹³C, <3 atom% ¹⁸O, Sigma-Aldrich).
- Carbon dioxide (CO₂, 99.995%, Messer)
- Helium (He, 99.9999%, Messer)
- Argon (Ar, 99.999%, Messer)
- Nitrogen (N₂, 99.995%, Messer)
- Compressed air (20.5% O₂, 79.5% N₂, Messer)

All reagents were used without further purification. Solutions were prepared using ultrapure deionized water (Millipore Direct Q3-UV, 18.2 MΩ cm)

The Au-based bimetallic NPs were synthesized with different compositions and uniform morphology using chemical reduction methods. A detailed description of the synthesis procedure is given in the following sections.

4.2. Au-Sn Bimetallic NPs

4.2.1. Synthesis of Au NPs

Gold NPs were prepared using a modified method reported elsewhere [97]. In a 250 cm³ round-bottom flask, 100 cm³ (0.25 mM) HAuCl₄ solution was added and heated under moderate stirring. When the solution started to boil, 0.7 cm³ of 0.23 M sodium citrate solution was added, and the solution color turned to wine red within a few seconds. Then the heating was stopped, and the colloid dispersion cooled down to room temperature. The molar ratio of HAuCl₄ to sodium citrate was adjusted to 1:6.

4.2.2. Synthesis of Au-Sn Bimetallic NPs

Bimetallic Au-Sn NPs with different nominal compositions (i.e., Au₂Sn₁, Au₁Sn₁, Au₁Sn₂, and Au₁Sn₄) were synthesized using an adopted two-step synthesis approach [98]. This method comprises the reduction of different amounts of tin precursor in the presence of premade gold

NPs, acting as nucleation seeds (**Figure 6**). In a typical procedure (for Au₁Sn₁ in this example), 5 cm³ aqueous solution of SnCl₄·5H₂O (5 mM) and 0.1 g of PVP were added to 100 cm³ of colloidal gold dispersion and stirred for 20 min. Subsequently, 10 cm³ of 0.26 M NaBH₄ solution was added to the reaction solution at room temperature. The color of the solution changed from wine red to deep brown, which implies the formation of Au-Sn bimetallic NPs. After stirring for 30 min, the product was centrifuged and washed with water and ethanol three times. For the other compositions, the amount of SnCl₄·5H₂O was adjusted to prepare the desired compositions.

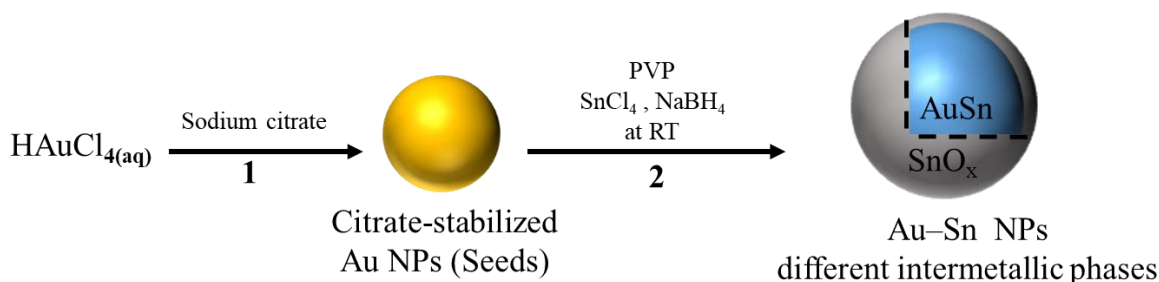


Figure 6. Schematic illustration of the synthesis of Au-Sn bimetallic NPs using a two-step approach.

4.3. Au-Ag Bimetallic NPs

4.3.1. Synthesis of Au-Ag Alloy NPs

Au-Ag NPs with different compositions (i.e., Au₈₀Ag₂₀, Au₆₀Ag₄₀, Au₄₀Ag₆₀, and Au₂₀Ag₈₀) were synthesized by varying the initial Au:Ag molar ratio (**Figure 7**) [99]. In a typical preparation, HAuCl₄ solution (120 μL, 0.05 M) was diluted to 10 cm³ in the presence of 0.01 mmol sodium citrate and heated to boil. In another vial, 10 cm³ of AgNO₃ solution with the same concentration and containing also 0.01 mmol sodium citrate was brought to boil. When both solutions boiled, the appropriate volumes were mixed and tempered for 20 min. Then, the dispersion cooled down to room temperature under stirring.

4.3.2. Synthesis of Au-Ag Core-Shell NPs

Au NPs with an average size of 15 nm, which act as the core, were synthesized by the reduction of 10 cm³ (1 mM) of a boiling aqueous solution of HAuCl₄ with 1 cm³ of 0.04 M trisodium citrate. The solution was boiling under continuous stirring for 10 min. Subsequently, it cooled down to room temperature [100]. The Ag shell grew in the next step. An aliquot of 2.5 cm³ of pre-synthesized Au NPs was diluted by adding 8 cm³ of ultrapure water. Then the solution was

brought to boil and 1 cm³ of 100 mM trisodium citrate was added at vigorous stirring. Finally, 2 cm³ of 5 mM silver nitrate was added dropwise, while the solution was kept boiling for 10 min. The Au-Ag core-shell NPs solution was cooled and stored at room temperature. By adjusting the amount of Ag precursor, the growth of the Ag shell over Au core was tuned.

4.3.3. Synthesis of Ag NPs

Silver NPs were synthesized based on a modified method [101]. In a 250 cm³ three-neck round-bottomed flask, a 100 cm³ aqueous solution of sodium citrate (5 mM) and tannic acid (0.25 mM) was heated under vigorous stirring. When the solution started to boil, 1 cm³ of AgNO₃ (25 mM) was added to this solution. The solution turned dark yellow. After the solution cooled down to room temperature, Ag NPs were washed by centrifugation to remove the excess of tannic acid and then they were redispersed in water.

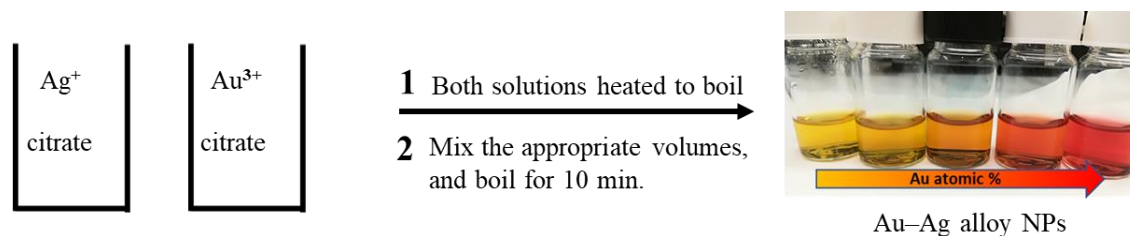


Figure 7. Schematic illustration of the synthesis of Au-Ag alloy NPs by varying the initial Au:Ag molar ratio.

4.4. Au-Pb Bimetallic NPs

4.4.1. Synthesis of Au-Decorated Pb NPs

A new protocol was developed for the synthesis of Au-Pb bimetallic NPs with different nominal compositions (i.e., Au₅Pb₉₅, Au₂₀Pb₈₀, Au₅₀Pb₅₀) using a two-step synthesis approach. Starting with the formation of metallic Pb NPs, which act as nucleation seeds, followed by the reduction of Au precursor (**Figure 8**). In a typical procedure for the synthesis of Au₅₀Pb₅₀, 0.05 g of Pb(NO₃)₂ was added to 30 cm³ of (0.25 mM) PVP. The solution was stirred under nitrogen atmosphere in a 100 cm³ round-bottomed flask for 20 min. Subsequently, 20 cm³ (50 mM) of NaBH₄ was added using a syringe pump at a rate of 0.2 cm³ min⁻¹. The solution was stirred for another 1 h to complete the reaction and decompose the remaining NaBH₄. Next, 6 cm³ (100 mM) of ascorbic acid was added, and the mixture temperature was adjusted to 50 °C. Then, 30 cm³ of (5 mM) HAuCl₄ solution was injected using a syringe pump at a rate of 0.2 cm³ min⁻¹. The solution was left stirring for 30 min and then allowed to cool down. The product was

collected by centrifugation at 10,000 rpm for 20 min and washed with ethanol/water mixture and then dried under nitrogen. Other compositions of Au-Pb bimetallic NPs were synthesized by changing the amount of Au precursor.

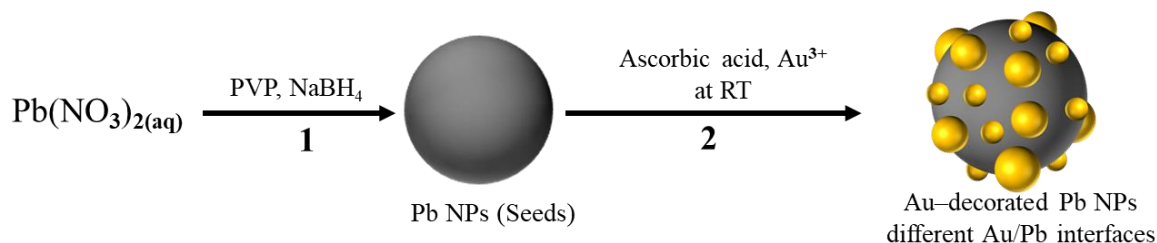


Figure 8. Schematic illustration of the preparation of Au-Pb bimetallic using a two-step approach.

4.4.2. Synthesis of Pb NPs

For the preparation of Pb NPs, 0.09 g of $\text{Pb}(\text{NO}_3)_2$ and 0.5 g PVP was added to 50 cm³ of ultrapure water in a 100 cm³ round-bottomed flask. The solution was stirred under nitrogen atmosphere for 20 min. Subsequently, 40 cm³ (50 mM) of NaBH_4 was added using a syringe pump at a rate of 0.2 cm³ min⁻¹. The solution was stirred for another 30 min to complete the reaction. The product was collected by centrifugation at 9,000 rpm for 20 min and washed with ethanol and then dried under nitrogen.

4.4.3. Synthesis of Pb-Decorated Au NPs ($\text{Pb}_{95}\text{Au}_5$ NPs).

0.5 g of PVP was added to 50 cm³ (0.25 mM) of pre-made Au NPs in a 250 cm³ round-bottomed flask and stirred at room temperature for 4 h. Then, 2 cm³ of 0.14 M $\text{Pb}(\text{NO}_3)_2$ was added and stirred under nitrogen. After 30 min, 30 cm³ of (50 mM) of NaBH_4 was added using a syringe pump at a rate of 0.2 cm³ min⁻¹. The stirring was continued for an additional 1 h, then the particles were collected by centrifugation at 10,000 rpm for 20 min and washed with ethanol/water mixture and then dried under nitrogen. The synthesis of small-sized Au seeds was carried out to keep the size of the $\text{Pb}_{95}\text{Au}_5$ sample similar to the other bimetallic particles as follows, 2 mL of 0.034 M trisodium citrate solution was added to a boiling solution of (100 mL, 0.25 mM) HAuCl_4 under moderate stirring. After a few seconds, the solution turned to deep red. Boiling and stirring were continued for 20 min. Finally, the dispersion cooled down under stirring to room temperature.

4.5. Morphological and Structural Characterization of Au-based NPs

Powder X-ray diffraction (XRD)

XRD measurements were carried out to determine the crystal structure of the Au-based NPs. XRD patterns were obtained by a Bruker D8 advance X-ray diffractometer with Cu K α ($\lambda = 1.5418 \text{ \AA}$) radiation, in the 2-theta range of 10–80°, with a scan rate of 0.4° min⁻¹. Rietveld refinement of the diffraction patterns was carried out to quantify the phase compositions.

Transmission electron microscopy (TEM)

TEM images were used to study the morphology of the synthesized bimetallic NPs and estimate the average particle size. The size distribution histograms were conducted from the analysis of at least 300 particles. TEM images were collected on a FEI Tecnai G² 20 X-Twin type instrument, working at an accelerating voltage of 200 kV.

Scanning electron microscopy (SEM)

The bulk composition was analyzed with a SEM equipped with an Energy dispersive X-ray spectroscopy (EDX). A Hitachi S-4700 field emission scanning electron microscope was for the measurements, operating at an accelerating voltage of 10 kV).

UV–vis absorption spectroscopy

UV–Vis absorption spectra were recorded using Agilent 8453 UV–Vis spectrophotometer to study the plasmonic properties.

X-ray photoelectron spectroscopy (XPS)

XPS was employed to characterize the chemical state of the elements at the NPs surface. The XPS spectra were obtained by a SPECS instrument equipped with a PHOIBOS 150 MCD 9 hemispherical analyzer. The analyzer was in FAT mode with 20 eV pass energy. The Al K α radiation ($h\nu = 1486.6 \text{ eV}$) of a dual anode X-ray gun was used as an excitation source and operated at 150 W power. Ten scans were averaged to get a single high-resolution spectrum. Charge neutralization was carried out during spectra acquisition, where the position and width of the adventitious carbon peak were monitored. The adventitious carbon peak was at 284.8 eV in all cases. Ar⁺ sputtering was carried out to remove the upper layers of the sample where specified. The Ar⁺ ion gun was operated at 1.2 kV for 10 min. For spectrum evaluation, CasaXPS commercial software package was used.

4.6. Electrode Preparation

Au-Sn Electrode

A suspension of the catalyst was prepared in isopropanol (5 mg cm^{-3}). Ultrasonic agitation was used to homogenize the suspension for 30 min. The sample was spray-coated to a preheated ($140 \text{ }^\circ\text{C}$) glassy carbon electrode (which were polished with $0.05 \text{ }\mu\text{m}$ Micropolish Alumina (Buehler), rinsed and sonicated in acetone, ethanol, and ultrapure water), using an Alder AD320 type airbrush and a homemade spray-coater robot, operated with 1 bar compressed air.

The obtained layers were subjected to heat treatment in Ar atmosphere at $300 \text{ }^\circ\text{C}$ to get rid of the residual of both PVP and any traces of the solvent. The heat treatment that was carried out at $400 \text{ }^\circ\text{C}$ or higher, resulted in a decrease in the stability of the tin-rich samples. Linear sweep voltammetry (LSV) profiles were recorded for different loadings between $0.1\text{--}1.5 \text{ mg cm}^{-2}$. It was found that for all compositions, the current density reached its maximum value around the loading of 0.35 mg cm^{-2} (see an example in **Figure 9**). This loading was employed in all experiments.

Au-Ag Electrode

The obtained dispersion after the synthesis was concentrated by centrifugation and redispersed in 2 cm^3 of Milli-Q-water. This solution was drop-casted to a preheated ($80 \text{ }^\circ\text{C}$) glassy carbon electrode. LSV profiles were recorded with different loadings between $0.25\text{--}0.65 \text{ mg cm}^{-2}$. The current density reached its maximum value around the loading of 0.53 mg cm^{-2} in the case of each composition (see an example in **Figure 10**). The obtained Ag layer was subjected to heat treatment in Ar atmosphere at $250 \text{ }^\circ\text{C}$ to get rid of the tannic acid.

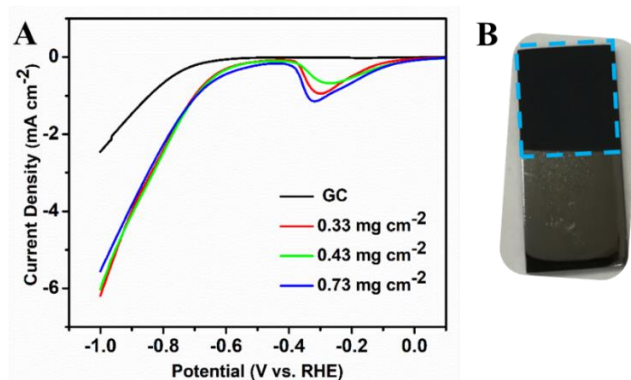


Figure 9. (A) LSV profiles of Au_2Sn_1 catalyst recorded with different loadings in CO_2 -saturated 0.1 M NaHCO_3 stabilized after multiple cycles. The black line indicates the activity of the bare glassy carbon substrate. Scan rate = 5 mV s^{-1} . (B) A photograph of the prepared electrode, which shows the deposited layer on glassy carbon.

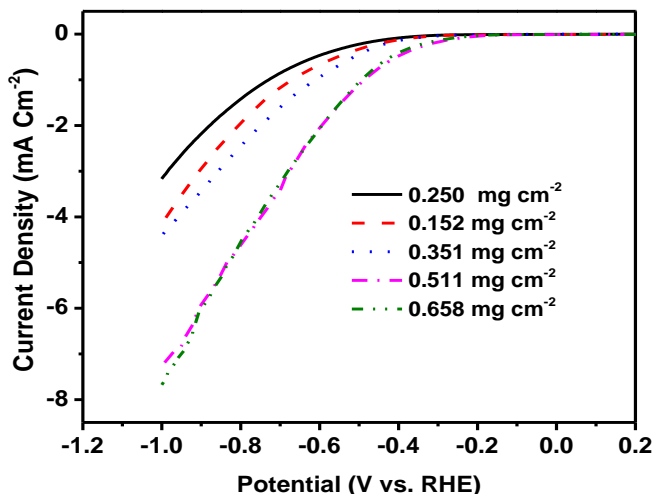


Figure 10. LSV profiles of Au₈₀Ag₂₀ catalyst recorded with different loadings in CO₂-saturated 0.1 M NaHCO₃ stabilized after multiple cycles. Scan rate = 5 mV s⁻¹.

Au-Pb Electrode

The suspensions of Au-Pb catalysts were prepared as described in the case of Au-Sn system. Then, the samples were spray-coated to a preheated (110 °C) glassy carbon electrode, using the previously mentioned setup, but 1 bar compressed N₂ was applied. The obtained layers were subjected to heat treatment in argon and air atmospheres at 280 °C to alter the quantity of Pb oxide species and to remove any traces of the solvent. The pure Au electrodes were prepared by drop-casting an aqueous concentrated dispersion to a preheated (80 °C) glassy carbon. The loading of 0.48 mg cm⁻² was employed in all experiments.

4.7. Electrochemical Measurements and CO₂ Reduction Products Analysis

A Metrohm Autolab PGSTAT302 type potentiostat/galvanostat was used for all electrochemical experiments. A typical three-electrode gastight two-compartment electrochemical cell was used to characterize the catalytic performance. The schematic diagram of the electrochemical cell is shown in **Figure 11**. A Nafion-117 proton exchange membrane was used as the compartment separator. A platinum foil (Alfa Aesar, 99.99%) and Ag/AgCl (3 M NaCl) were used as a counter electrode and a reference electrode, respectively. The measured potentials were converted to RHE reference scale using $E_{RHE} = E_{Ag/AgCl} + 0.210 \text{ V} + 0.0591 \times \text{pH}$. All currents were normalized to the geometric surface area of the electrodes. Each compartment was filled with HCO₃⁻¹ solution. The cathode compartment contained 35 cm³ of electrolyte with a ~25 cm³

headspace. Before electrolysis, the electrolyte in each compartment was purged with CO₂ gas for 30 min, and the pH of the electrolytes 0.1 M NaHCO₃ and 0.5 M KHCO₃ were 6.62 and 7.2, respectively after saturation. The electrolyte in the cathodic compartment was stirred at a rate of 1000 rpm. During chronoamperometry measurements, the effluent gas from the headspace of the cathodic compartment was fed into the online sampling loop of the gas chromatograph (GC) every 30 min for quantification of gas-phase CO₂ reduction products. The GC (SHIMADZU, GC-2010 plus) was equipped with a barrier discharge ionization detector. A ShinCarbon ST column was used for the separation, with helium (99.9999%) as the carrier gas. The liquid sample was collected at the same time and analyzed using a Bruker Avance Neo 500 NMR spectrometer. The sample (450 μL) was mixed with 50 μL D₂O containing phenol and dimethyl sulfoxide as internal standards. The one-dimensional ¹H spectrum was measured using a solvent presaturation method to suppress the water peak. The ratio of the peak areas of the products and the internal standards were used for the calibration. Peak areas of the products right to the water peak were compared to the peak area of dimethyl sulfoxide, while the peaks areas of the products left to water peak were compared to the peak area of phenol. FE values of the products were calculated from the amount of charge passed to produce each product divided by the total charge passed.

Cyclic voltammetry (CV) of Au-Sn bimetallic NPs was conducted in CO₂-saturated 0.1 M NaHCO₃ at different scan rates (10, 25, 50, 100 mV s⁻¹), in the potential range where no Faradaic event takes place to estimate the electrochemical active surface area (ECSA). The charge capacitance of the finely polished Sn foil was used to normalize the charge capacitance of the bimetallic NP electrodes. Subsequently, the total electrocatalytic currents were normalized by this relative electrochemically active surface area.

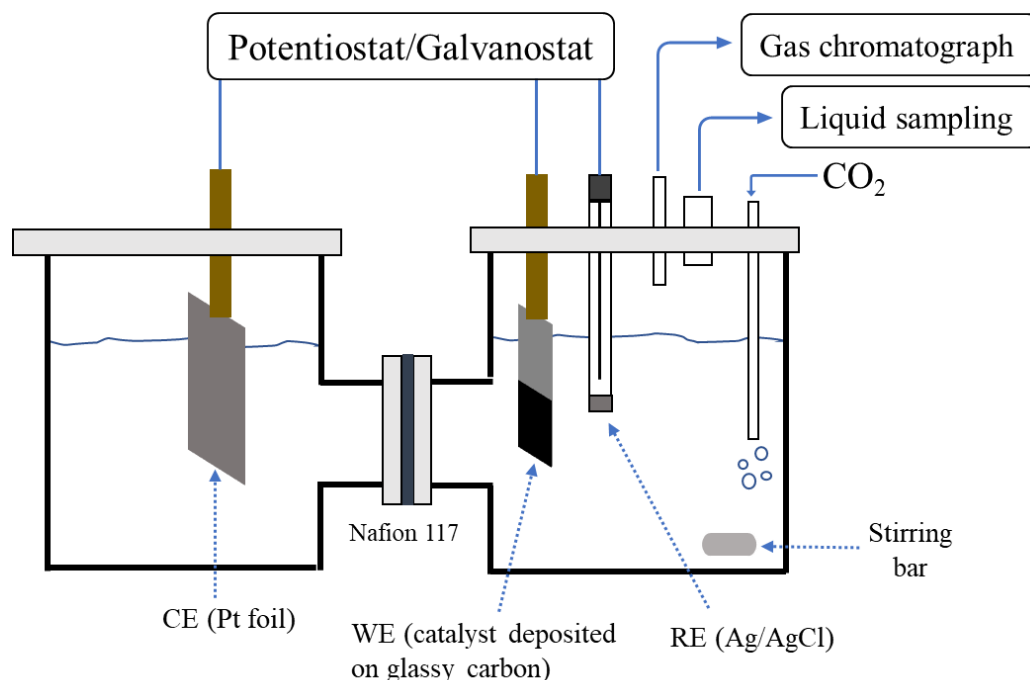


Figure 11. Schematic diagram of the electrochemical reduction of CO_2 in a two-compartment cell. (counter electrode (CE), working electrode (WE), reference electrode (RE)).

4.8. Isotopic Labeling Experiments

Au-Sn system

Selective isotopic labeling experiments were performed to gain insights into the mechanism of CO_2 reduction on Au-Sn bimetallic catalysts. The two carbon sources (CO_2 gas and NaHCO_3) were selectively labeled. When the bicarbonate was the labeled component, 35 cm^3 ultrapure water was added in the cathodic compartment and saturated with $^{12}\text{CO}_2$, and then an appropriate amount of labeled bicarbonate was dissolved in 5 cm^3 of the $^{12}\text{CO}_2$ -saturated water and quickly added to the cell. In the experiment when the CO_2 gas was the labeled component, at first, 35 cm^3 water was purged with Ar to remove all dissolved gases, and then $^{13}\text{CO}_2$ gas was purged (42.6 $\text{cm}^3 \text{ min}^{-1}$ flow rate for 11 min). Finally, the NaHCO_3 was dissolved in 5 cm^3 of the $^{13}\text{CO}_2$ -saturated water and quickly added to the cell. The electrolysis was started right after the addition of the bicarbonate ions to the cell, where the non-equilibrium condition is in effect and the isotopic composition of the CO_2 gas is different from that of bicarbonate. The isotopic composition of the CO product was monitored with gas chromatography-mass spectrometry (GC-MS, Shimadzu GC-MS QP2010 S, RT Molsieve 5 Å column), in selective ion monitoring

mode. The signal of the $m/z = 28$ and $m/z = 29$ molecule ions of the CO were used in the analysis. A gas sample of 200 μL was taken from the headspace of the cathodic compartment and injected into the GC–MS with a gastight syringe every 11 min. Analysis was carried out under the following parameters: $T_{\text{start}} = 90\text{ }^\circ\text{C}$ (0 min), $\Delta T_{\text{ramp}} = 10\text{ }^\circ\text{C min}^{-1}$, $T_{\text{end}} = 110\text{ }^\circ\text{C}$ (0 min), $\Delta T_{\text{ramp}} = 30\text{ }^\circ\text{C min}^{-1}$, $T_{\text{end}} = 150\text{ }^\circ\text{C}$ (3 min); injection temperature: $T = 200\text{ }^\circ\text{C}$; linear velocity was controlled by the pressure $p = 50\text{ kPa}$; and split ratio: 50. The NMR spectroscopy was employed for the identification and quantification of the produced formate in the liquid phase. The ^1H spectrum was measured under the same conditions mentioned in section 4.7.

Au-Pb system

The two carbon sources (CO_2 gas and KHCO_3) were labeled. 35 mL of 0.5 M $\text{KH}^{13}\text{CO}_3$ was purged at first with Ar for 45 min to remove all the dissolved gases, and then $^{13}\text{CO}_2$ gas was purged ($42.6\text{ cm}^3\text{ min}^{-1}$ flow rate for 11 min). The electrolysis was conducted at a constant potential of -1.07 V vs. RHE. GC–MS (Shimadzu GC-MS QP2010 S, RT Molsieve 5 \AA column) was employed for monitoring the isotopic composition of the CH_4 and CO Products, in selective ion monitoring mode. The signal of the $m/z = 17, 16, 15, 14, 13,$ and 12 molecule ions of the CH_4 were used in the analysis, and for CO, the signal of the $m/z = 28$ and $m/z = 29$ molecule ions of the CO were used. A gas sample of 300 μL was taken from the headspace of the cathodic compartment and injected into the GC–MS with a gastight syringe every 11 min. The analysis was carried out under the above-mentioned parameters.

4.9. In situ Raman Spectroelectrochemistry

Raman spectra were recorded with a SENTERRA II Compact Raman microscope, using 532 nm laser excitation wavelength by 2.5 mW power and a 50 \times objective. In situ electrochemical Raman experiments were performed using an ECC-Opto-Std electrochemical cell (EL-CELL GmbH) equipped with a sapphire window, and a potentiostat/galvanostat (Interface 1010E – GAMRY). The spectra were recorded after a 100 s potentiostatic conditioning at each potential. For the Au-Sn system, the working electrodes were prepared by spray-coating of 5 mg cm^{-3} suspensions of Au_1Sn_2 and pure Sn NPs in isopropanol and aqueous Au NP to a preheated ($140\text{ }^\circ\text{C}$) platinum mesh. All catalysts were studied in CO_2 -saturated 0.1 M NaHCO_3 electrolyte and a set of control experiments were performed on the Au_1Sn_2 catalyst in N_2 -saturated 0.1 M Na_2SO_4 . And for the Au-Pb system, the working electrodes were prepared by spray-coating of

5 mg cm⁻³ suspensions of Au₅₀Pb₅₀ and pure Pb NPs in isopropanol to a preheated (110 °C) carbon paper. The catalysts were studied in CO₂-saturated 0.5 M KHCO₃ electrolyte

4.10. Ambient Pressure Photoemission Spectroscopy Measurements

Ambient pressure UV-photoelectron spectroscopy (APS) measurements were conducted to determine the WF of the samples, using a KP Technology APS04 instrument. A 2 mm-diameter tip with gold alloy coating was approximately 1 mm apart from the sample. The sample surface was illuminated by UV light source with a spot size of approximately 3 × 4 mm and the energy of the incident photon (E_{ph}) ranged between 3–7 eV. Upon photon absorption ($E_{ph} \geq \Phi$, where Φ is sample WF), electron cloud is formed, and consequently, atmospheric ions such as N₂⁻ and O₂⁻ are generated because of inelastic scattering between ejected electrons and atmospheric molecules. These ions and/or electrons are collected by Kelvin probe tip, and thus the ion current is recorded as a function of photon energy. For metals, a linear relation is expected when the square root of photocurrent is plotted as a function of photon energy ($R^{1/2} = k (E_{ph} - h\nu_0)$ where R is photocurrent per absorbed photon, h is Planck's constant, and ν_0 is the threshold frequency [102]. The intersection of the straight line section with the zero-baseline gives the initial photoelectron threshold which is considered to be the metal WF.

4.11. Theoretical Calculations

We had regular meetings with prof. Núria López (ICIQ Tarragona, Spain) and her research group to discuss their theoretical efforts to the proposed mechanism of CO₂ reduction over Au-Pb catalysts. DFT calculations were performed with VASP 5.4.4 [103–106], the Perdew–Burke–Eenzerhof functional [107,108] was used with projected augmented wave pseudopotentials [109,110] and an energy cutoff the plane waves of 450 eV. Bulk calculations were done with 3 × 3 × 3 k-point sampling, whereas slabs calculations with 3 × 3 × 1. After geometry optimization of the bulks Au, Pb, Au₂Pb, PbAu₂, slabs calculations were performed with dipole corrections and van der Waals interactions were included with DFT-D2. For each alloy, the low index surfaces (100, 101, 111, 110, 001) were investigated. The representation of the diluted alloy Au (3%) in Pb structure was done by substitution of a Pb site with Au. The choice of using a surface with 3% Au concentration in the simulation instead of the experimental 5% was due to computational efficiency. Oxide contributions were analyzed by adding O either on the surface or subsurface position. Subsequent CO₂ reduction calculations were performed on the most

stable surfaces. The Computational Hydrogen Electrode (CHE) [29,67,111] was used for modeling the CO₂ reduction [112] and to compute the Gibbs free energies of the reaction. The final results of the PbAu 3% consistent with larger systems on a 2×2 supercell at Gamma point with an Au island instead of a single atom. The geometrical structures of the most stable surfaces where the reactions paths were computed are shown in **Figure 12**. Gibbs free energy for CH₄, HCOOH, CO, and H₂ paths and more about the proposed paths can be found in the third paper of the publication list. All structures and input and output files can be accessed at the ioChem-BD database[113] under this link:

<https://iochem-bd.iciq.es/browse/review-collection/100/22849/0ed1c88f8d705d4306cea07d>

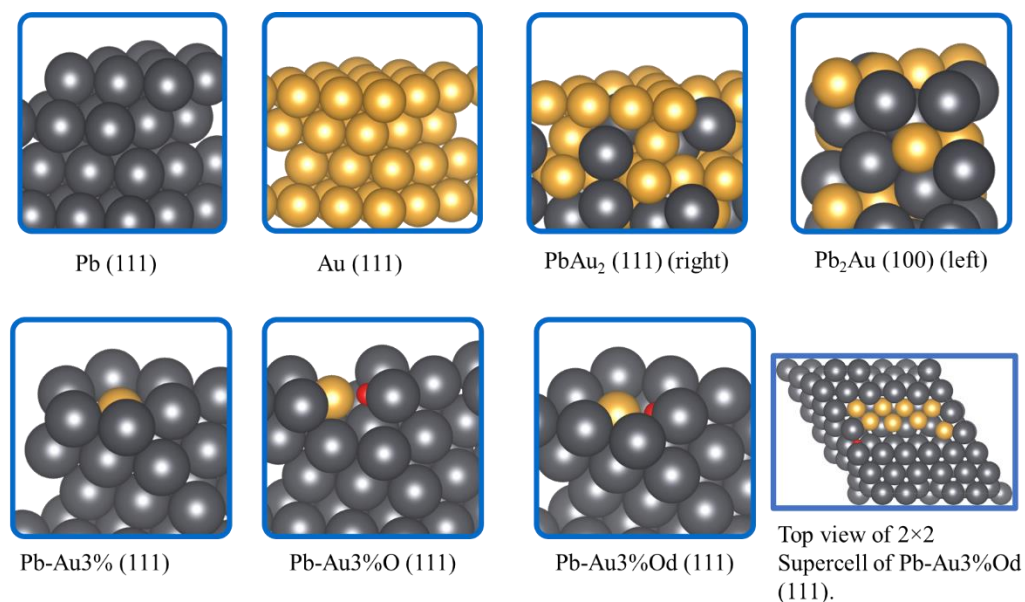


Figure 12. The optimized structures of the most stable surfaces. The difference between Pb-Au3%O (111) and Pb-Au3%Od (111) is that the O is lower in the subsurface of Pb-Au3%Od (111) and is more stable by 0.1 eV compared to Pb-Au3%O (111), O is on the surface.

5. Results and Discussion

This chapter describes the characterization of the synthesized combinations of Au with p-block elements (Pb and Sn) with different compositions and highlights the effect of the phase composition of Au-Sn bimetallic NPs on both catalytic activity and product distribution in CO₂RR. The influence of replacing Sn with Pb on the catalytic performance and selectivity was studied. The effect of tuning the electronic properties activity of Au-Ag nanoalloys was discussed and compared to the catalytic activity of the Au-Ag core-shell structure.

5.1. Au-Sn Bimetallic NPs Activity for CO₂RR

5.1.1. Synthesis and Characterization of Au-Sn Bimetallic NPs

Bimetallic Au-Sn NPs with different nominal compositions (i.e., Au₂Sn₁, Au₁Sn₁, Au₁Sn₂, and Au₁Sn₄) were synthesized using a two-step synthesis approach, where different amounts of tin precursor were reduced in the presence of premade NPs, acting as nucleation seeds. The crystal structure of the NPs was determined using powder XRD (**Figure 13A**). The pure gold showed peaks at $2\theta = 38.14^\circ$, 44.44° , 64.71° , and 77.73° corresponding to the face-centered cubic phase of gold. The bimetallic phases showed distinctly different XRD patterns, confirming that new phases were formed (and not simple alloying occurred). The Au₂Sn₁ sample had additional peaks at 2θ of 23.67° , 28.74° , and 40.53° assigned to the hexagonal AuSn intermetallic phase. The AuSn phase became more predominant with a further increase in Sn⁴⁺ concentration (sample Au₁Sn₁), and even the formation of phase-pure AuSn was obtained (sample Au₁Sn₂). A different diffraction pattern was observed at the highest Sn content (sample Au₁Sn₄), associated with the orthorhombic intermetallic AuSn₂ phase. The pure tin exhibited a tetragonal phase. Rietveld refinement of the diffraction patterns was carried out to quantify these trends (**Figures 13 B – C and Table 4**). The percentage of the AuSn intermetallic phase increased from 44 to 88 and 100%, in the series of Au₂Sn₁, Au₁Sn₁, and Au₁Sn₂ samples, respectively.

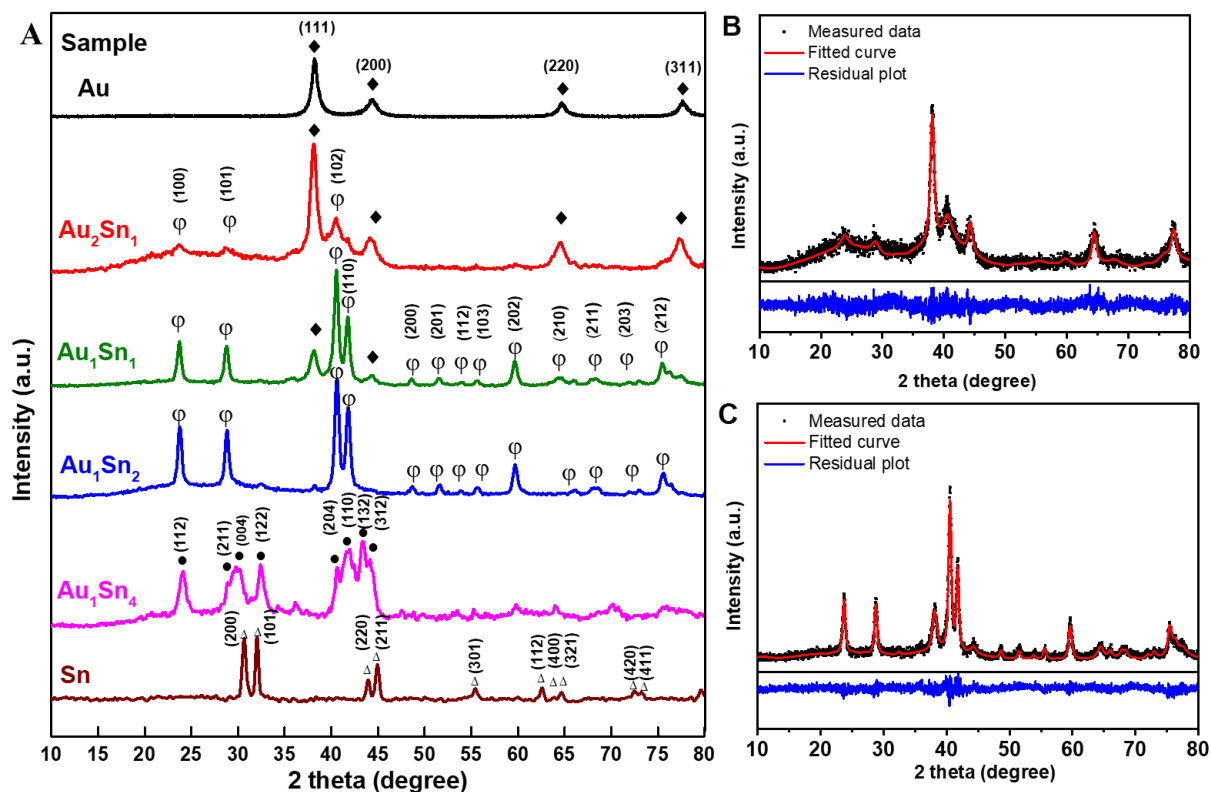


Figure 13. (A) X-ray diffraction patterns of Au-Sn bimetallic NPs and the parent metals. The diffractions corresponding to the respective crystal phases in the samples are indicated by these marks; ♦ Au, ⊕ AuSn, • AuSn₂, Δ Sn. Rietveld refinement of the XRD patterns recorded for samples: (B) Au₂Sn₁, (C) Au₁Sn₁.

Table 4. Phase composition of Au-Sn bimetallic NPs determined from Rietveld refinement.

Sample	Phase composition (w/w%)			
	Au	AuSn	AuSn ₂	Sn
Au	100	0	0	0
Au ₂ Sn ₁	56	44	0	0
Au ₁ Sn ₁	20	80	0	0
Au ₁ Sn ₂	0	100	0	0
Au ₁ Sn ₄	0	0	100	0
Sn	0	0	0	100

The morphology of the Au-Sn bimetallic NPs and their monometallic counterparts was characterized by TEM. Au NPs are mainly spherical and crystalline, with an average diameter of 22.4 ± 2.2 nm (**Figure 14**). After the incorporation of Sn, the synthesized bimetallic NPs retained the spherical shape and with narrow size distribution. The size of the samples was 23 ± 2.9 , 31.8 ± 3.9 , 32.4 ± 3.7 , and 33 ± 2.5 nm, in the series of samples with increasing Sn content (**Figures 15–16**). HR-TEM images of Au₂Sn₁ showed two lattice fringes with d-spacings of 0.23 and 0.22 nm, assigned to (111) plane of gold and (102) plane of AuSn, respectively (**Figure 15E**) [114]. Based on a careful analysis of 50 particles, a core was detected in the center, and a few of the trigonally-shaped Au NPs were among these particles (**Figure 17**), which is in good agreement with the XRD results (i.e., Au₂Sn₁ was a mixture of gold and AuSn phases). For Au₁Sn₁, two d-spacing values were determined (0.31 and 0.37 nm) corresponding to (101) and (100) planes of AuSn (**Figure 15F**). Sample Au₁Sn₂ exhibits lattice fringes with a d-spacing of 0.31 nm that can be assigned to (101) plane of AuSn (**Figure 15G**), whereas Au₁Sn₄ shows two d-spacing values of 0.27 and 0.38 nm corresponding to (122) and (117) planes of AuSn₂, respectively (**Figure 15H**). Based on the XRD and HR-TEM results, the gradual phase transformation of gold NPs into intermetallic compound phases during the increase of tin content was confirmed and an amorphous layer on the surface of bimetallic NPs was also detected.

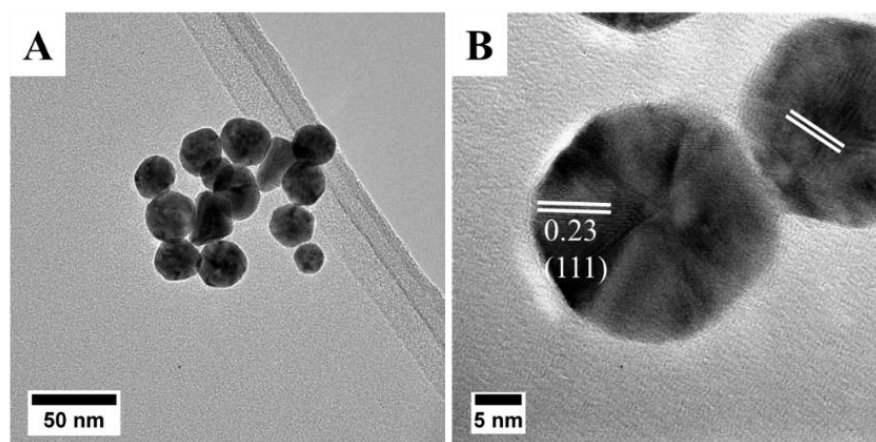


Figure 14. (A) TEM and (B) HR-TEM images of gold seeds. The lattice fringes of the sample were observed clearly showing a d-spacing value of 0.23 nm corresponding to (111) plane of fcc Au.

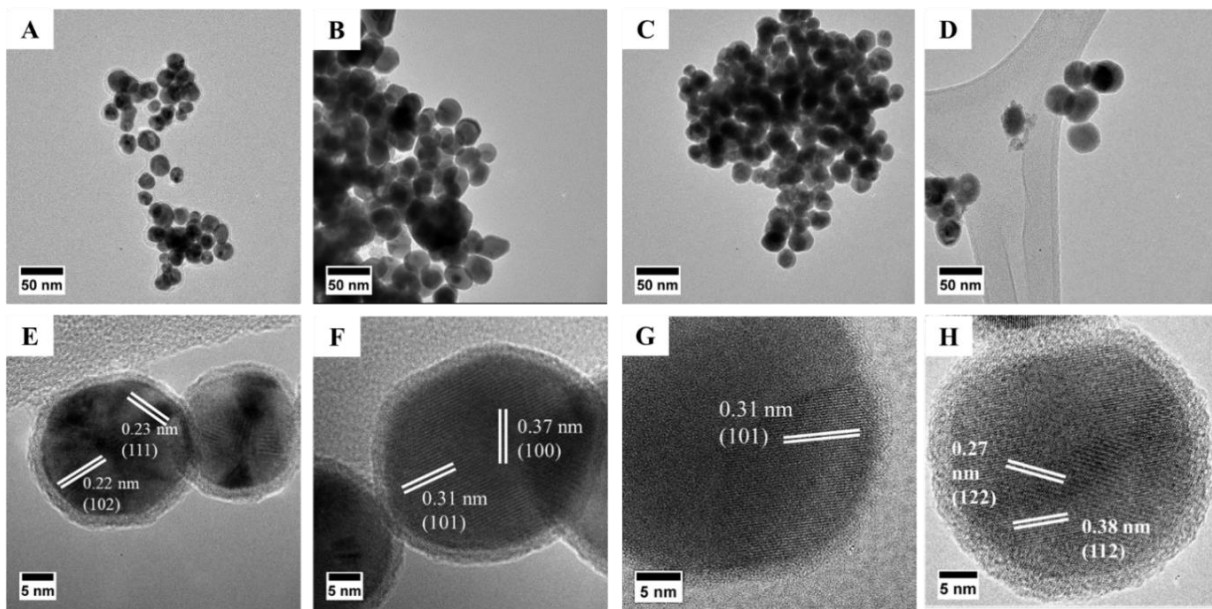


Figure 15. TEM images of Au-Sn bimetallic NPs. (A) Au_2Sn_1 , (B) Au_1Sn_1 , (C) Au_1Sn_2 , and (D) Au_1Sn_4 . (E–H) corresponding HR-TEM images. Lattice fringes are highlighted together with the corresponding crystal facets. The thickness of the amorphous layer increased, in the series of samples with growing tin content as follows; 1.5 ± 0.19 , 1.8 ± 0.32 , 2.45 ± 0.25 , and 2.75 ± 0.23 nm.

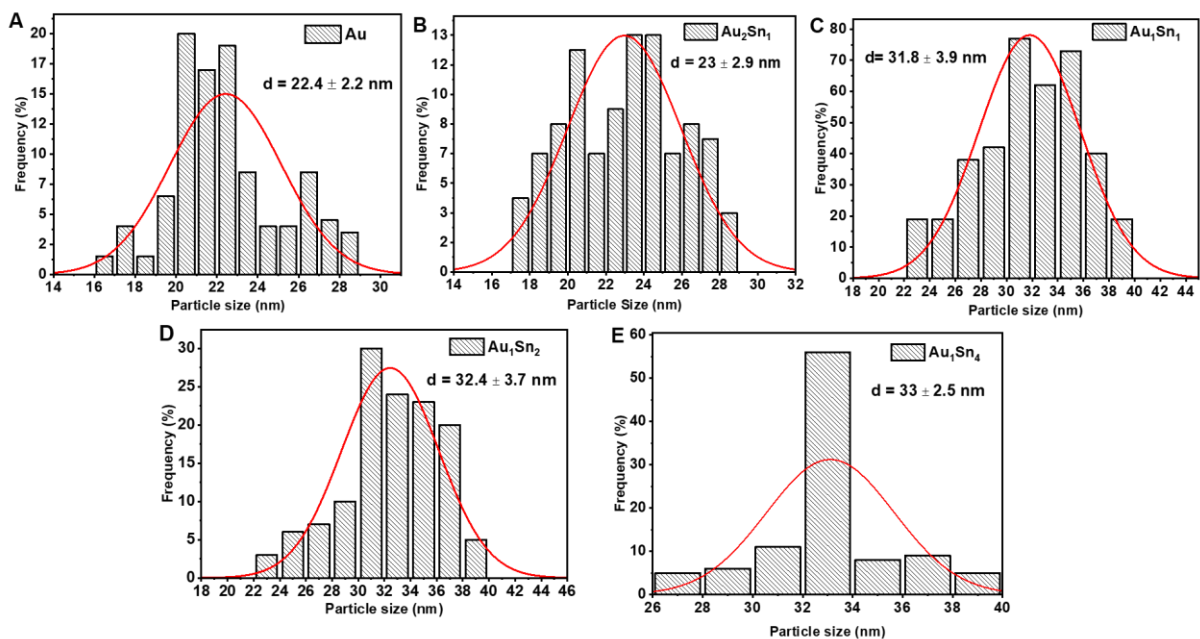


Figure 16. Size distribution of Au-Sn bimetallic NPs (a) Au seeds, (B) Au_2Sn_1 , (C) Au_1Sn_1 , (D) Au_1Sn_2 , and (E) Au_1Sn_4 .

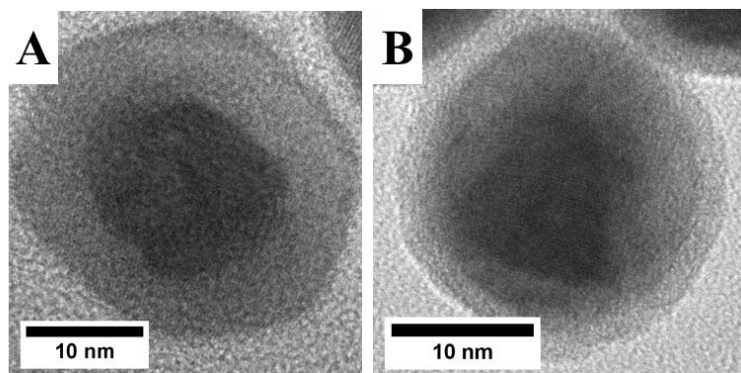


Figure 17. (A) and (B) TEM images of Au_2Sn_1 bimetallic NPs with a core-shell structure suggesting the diffusion of Sn.

The chemical nature of the NP surface was characterized by XPS. **Figure 18.** shows the XPS fitting of Au 4f and Sn 3d spectra of the four bimetallic samples. The Au 4f spectrum of Au_2Sn_1 shows two peaks at 87.02 and 83.33 eV that can be assigned to the $4f_{5/2}$ and $4f_{7/2}$ peaks of Au^0 [44]. The corresponding Sn 3d spectrum showed the presence of $\text{Sn}^{4+/2+}$ (494.65 and 485.45 eV) and Sn^0 (492.88 and 483.97 eV). The amount of the partially oxidized tin species (SnO_x) on the surface increased gradually with the total Sn concentration: the sample with the highest tin content (Au_1Sn_4) exhibited only a single Sn 3d doublet at 494.81 and 486.15 eV that corresponding to $\text{Sn}^{4+/2+}$. A minor, but significant shift in the Au 4f peaks to higher binding energy was observed with increasing Sn content as a result of alloying [115]. The bulk composition was analyzed by EDX. The atomic percentages of Au and Sn are listed in **Table 5**, together with the surface composition obtained from XPS. The atomic ratios of constituent metals are close to the stoichiometric molar ratio in the bulk, but not on the surface. It seems that there is always an excess Sn on the surface, regardless of the bulk phase composition. Since there was no sign of oxidized gold detected by XPS, therefore the amorphous layer identified by TEM measurements is most likely consists of partially oxidized tin (SnO_x). Note the good agreement between the increase in thickness of the amorphous shell (see HR-TEM images in **Figure 15**) and the increasing SnO_x amount on the surface (**Table 5**).

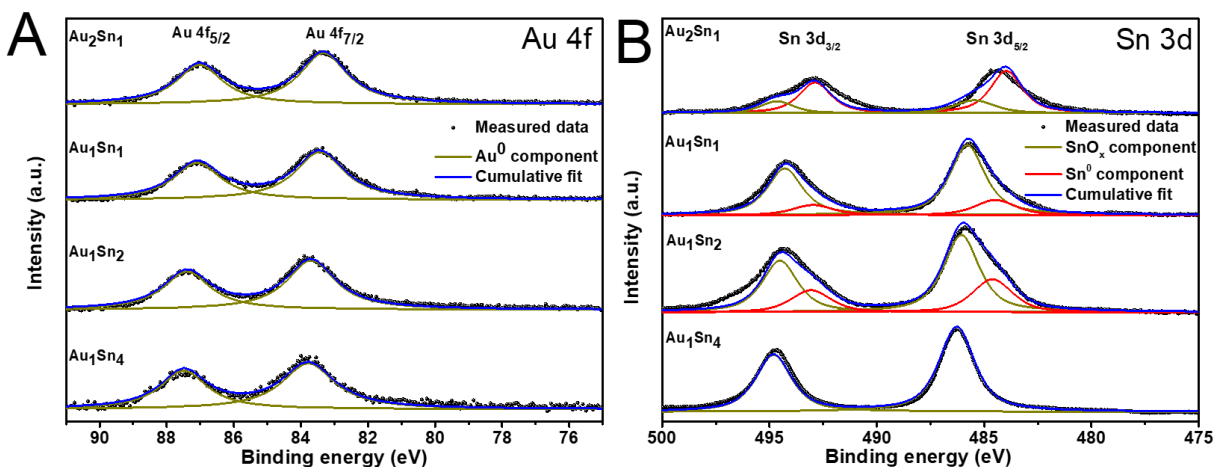


Figure 18. High-resolution XP spectra of Au-Sn bimetallic NPs: (A) Au 4f spectrum, and (B) Sn 3d spectrum.

Table 5. Bulk and surface composition of Au-Sn bimetallic NPs.

Sample	EDX Bulk composition (atomic %)		XPS Surface Composition (atomic %)		
	Au	Sn	Au	Sn	SnO _x
Au₂Sn₁	75.1	24.9	27.5	53.9	18.6
Au₁Sn₁	54.4	45.6	19.4	14.7	65.9
Au₁Sn₂	39.4	60.6	15.0	26.0	59.0
Au₁Sn₄	34.6	65.4	4.6	0.0	95.4

5.1.2. Electrocatalytic CO₂ Reduction Activity

The electrochemical reduction of CO₂ was first studied by LSV to identify the potential window of CO₂RR. The onset potential in the CO₂-saturated solution was notably less negative compared to that in N₂-saturated solution ($E = -0.37$ V in CO₂ and -0.65 V in N₂ vs. RHE (**Figure 19A**)). This observation indicates that an additional process occurred in the CO₂-saturated solution, which requires less overpotential, compared to the one occurring in N₂-saturated solution (i.e., HER) [85]. When comparing the voltammetric curves recorded in CO₂-saturated 0.1 M NaHCO₃ for the different Au-Sn electrodes, a clear shift in the onset potentials was observed (**Figure 19B**). Importantly, the trend in the onset potential values does not exactly reflect the change in the composition. This can be explained by the fact that new bimetallic phases are formed (rather than simple alloying), which in turn results in a non-linear change in the bulk and surface energetics, dictating the CO₂ reduction properties. Also note that these differences in the onset potential are rather substantial, since the total range spans through 440 mV.

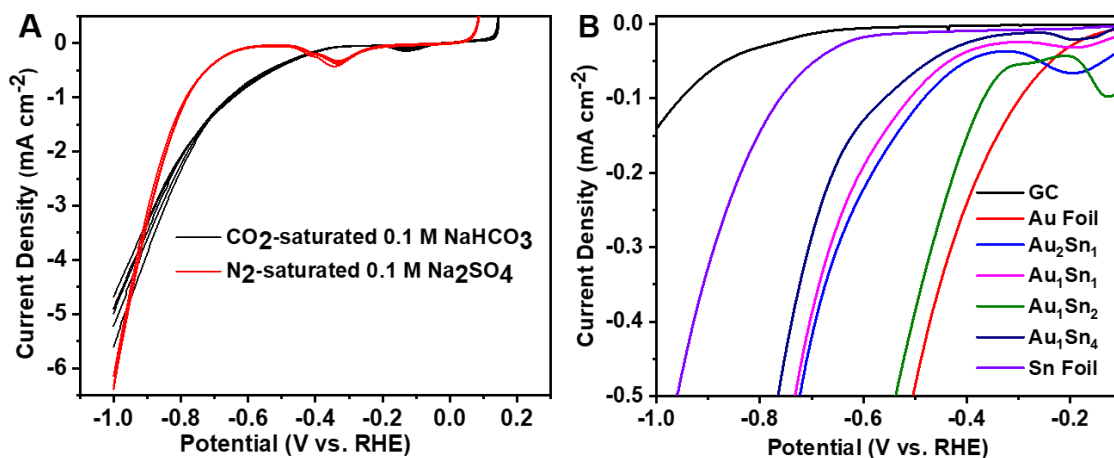


Figure 19. (A) LSV profiles of Au₁Sn₂ catalyst recorded in CO₂-saturated 0.1 M NaHCO₃, and N₂-saturated 0.1 M Na₂SO₄. Scan rate = 5 mV s⁻¹. (B) LSV profiles of Au-Sn NPs and Au and Sn foils, recorded in CO₂-saturated 0.1 M NaHCO₃ stabilized after multiple cycles. The black line indicates the activity of the bare glassy carbon substrate. Scan rate = 5 mV s⁻¹. The loading was 0.35 mg cm⁻² in all cases.

The CO₂ reduction performance of the bimetallic NPs was explored under chronoamperometric conditions. Analysis of the reduction products confirmed the formation of CO and HCOOH, while the remaining charge was accounted for the HER. The total current density values recorded for the Au₁Sn₂ catalyst at different potentials are presented in **Figure 20**, together with the partial current density values for the various products. Relatively stable currents were measured during the electrolysis for all compositions, and its value increased with the overpotential (**Figure 22**). At -1.1 V vs RHE, a stable current of 11 mA cm⁻² was achieved with a FE_{HCOOH} of 42%, whereas the decrease in the current and FE_{HCOOH} was seen at lower overpotentials (with the parallel rise of HER activity). Tuning the composition altered this trend (**Figure 22**), as a FE_{HCOOH} of 51% was observed at -0.9 V vs. RHE over Au₁Sn₄ catalyst, which decreased to 29% at more negative potential (-1.1 V vs. RHE). In addition to summarizing the abovementioned trends for the Au₁Sn₂ catalyst, **Figure 20B** also depicts that the formation of CO was rather independent from the potential, which translates to a CO/H₂ ratio of 1:6–7. The stability of Au₁Sn₂ catalyst was investigated using a two-compartment cell. The current (8 mA cm⁻²), remained stable within the 10 h electrolysis (**Figure 21**). In fact, a slight increase was witnessed in the current, due to surface roughening of the catalyst. TEM analysis confirmed that the catalyst particles retained their morphology and only a partial reduction of the SnO_x shell was observed from the TEM-EDX analysis (**Figure 23**), where the initial O/Sn ratio (0.26) dropped to 0.15 after electrolysis (while the Au/Sn ratio remained constant). These data confirm

that the crystalline bimetallic core and the amorphous shell are both stable under the reduction conditions, although the latter one undergoes partial reduction.

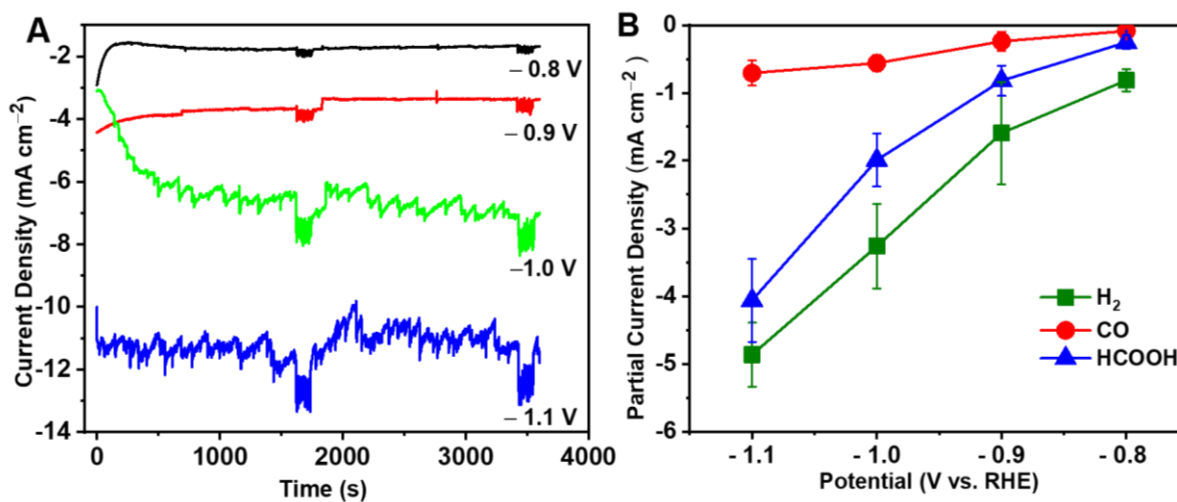


Figure 20. Electrochemical CO₂ reduction performance of the Au₁Sn₂ catalyst: (A) total current density as a function of time at various potentials, (B) HCOOH, CO, and H₂ partial current densities. Error bars represent the standard deviation, obtained by studying three different electrodes.

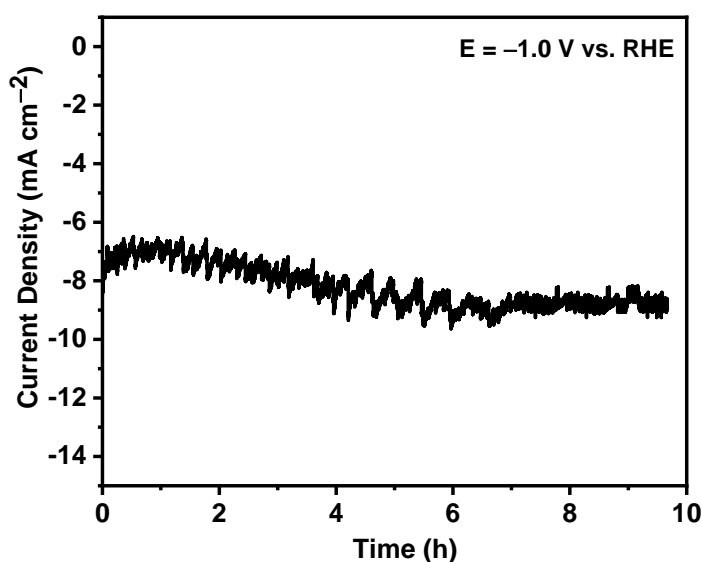


Figure 21. Long-term stability performance of Au₁Sn₂ catalyst measured in CO₂-saturated 0.1 M NaHCO₃ at -1.0 V vs. RHE.

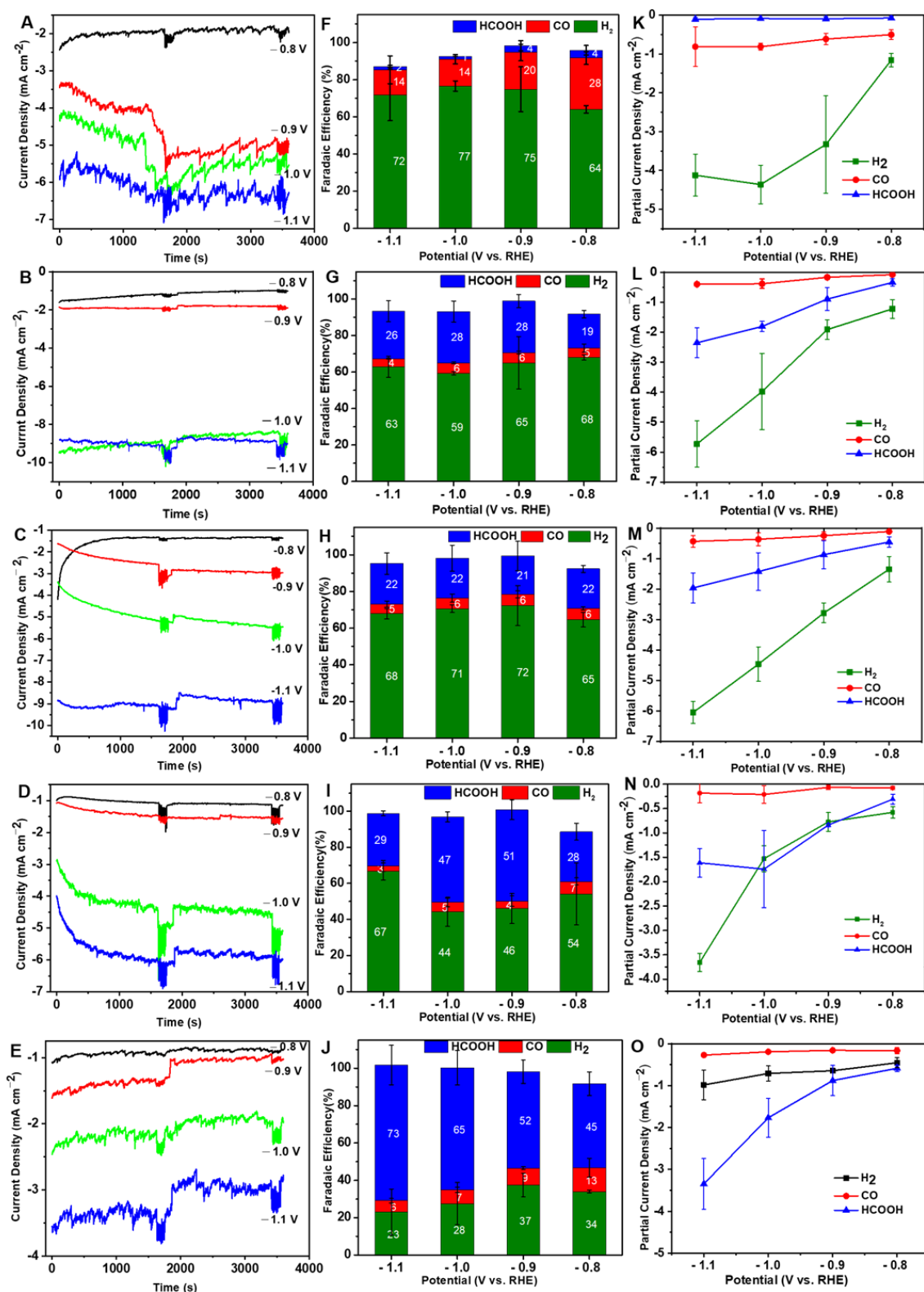


Figure 22. CO₂ reduction activity of Au-Sn bimetallic NPs at -0.8 V, -0.9 V, -1.0 V, and -1.1 V vs. RHE: total current density as a function of time (A) Au foil, (B) Au₂Sn₁, (C) Au₁Sn₁, (D) Au₁Sn₄, and (E) Sn foil. (F-J) the corresponding FE of CO, HCOOH, and H₂. (K-O) the corresponding partial current densities of CO, HCOOH, and H₂.

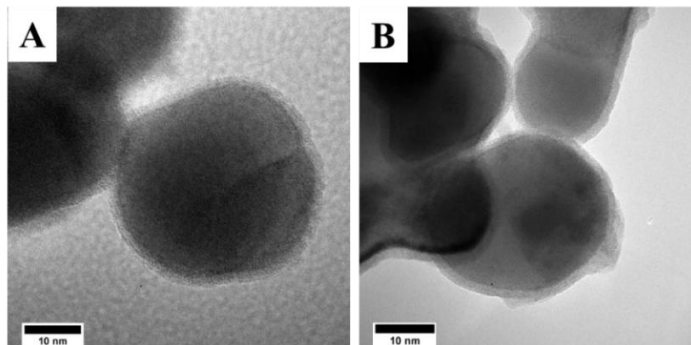


Figure 23. TEM images of Au_1Sn_2 catalyst: (A) before and (B) after 10 h electrolysis in CO_2 -saturated 0.1 M NaHCO_3 at -1.0 V vs. RHE.

The current density values recorded for the Au-Sn NPs as well as the parent metals are shown in **Figure 24A**. At less negative potentials (i.e., -0.9 V vs. RHE), the Au foil exhibited the largest total current density, while at more negative potentials the bimetallic samples outperformed both Au and Sn. The three samples where the AuSn phase was present (see XRD analysis) showed significantly higher current densities. This trend was further magnified when the current density was normalized with the ECSA (**Figure 24B**).

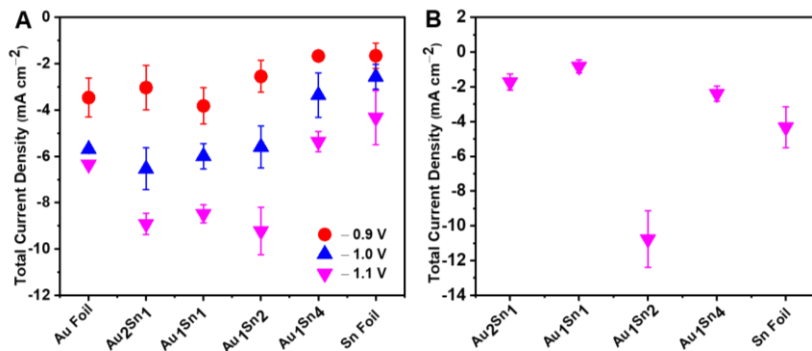


Figure 24. Electrochemical CO_2 reduction activity of Au-Sn NPs, and parent metals. (A) Total current density, (B) normalized total current density measured at -1.1 V vs. RHE. Error bars represent the standard deviation obtained by studying three different electrodes.

Figure 25 shows product distribution as a function of compositions at -1.0 V vs. RHE. Au foil produces about 80 % H_2 , while CO and HCOOH are produced in relatively small amounts. The Au-Sn NPs produced a considerable amount of HCOOH as the dominant CO_2 R product. A relatively linear correlation was observed between the Sn concentration and the FE_{HCOOH} , while HER was gradually suppressed to about 44 % (incorporation of Sn into Au resulted in a slower kinetics towards H_2 production). The FE_{CO} , on average, was about 10 % and there it showed very little composition dependence at this potential. Generally, the H_2/CO ratio

varies in a broad range between 2.5 and 10, depending on the composition and the applied potential (**Figure 22**).

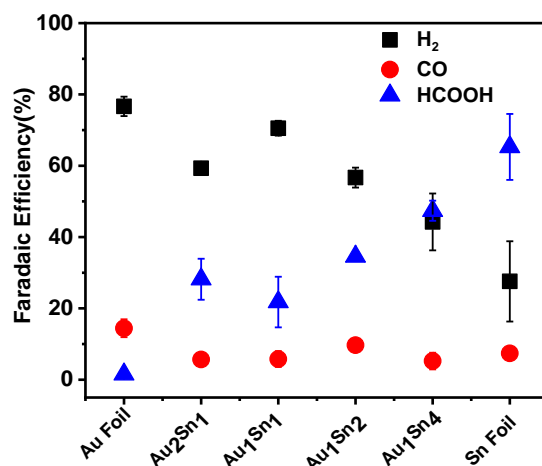


Figure 25. Electrochemical CO₂ reduction activity of Au-Sn NPs, and parent metals. Faradaic efficiency values as a function of composition at -1.0 V vs. RHE. Error bars represent the standard deviation obtained by studying three different electrodes.

We performed a series of control experiments, where electrodes were prepared from physical mixtures of Au and Sn NPs. A physically mixed Au+Sn electrode (1:2 molar ratio) with similar loading exhibited a much lower current density at all potentials and CO₂R selectivity (**Figure 26**), directly highlighting the importance of the AuSn phase. Note, for example, the difference in the FE_{HCOOH} 15% vs. 42% at -1.1 V vs. RHE. And the FE_{HCOOH} was independent from the potential in this case, unlike in the case of the alloy. Finally, the FE_{CO} was smaller than in any other studied cases. To understand the effect of the electronic properties on the catalytic behavior, we determined the WF of the different catalysts Kelvin probe measurements proved that the bimetallic nanoparticles are new chemical entities, having distinctly different electronic properties (**Figure 27**). Notably, the trend in the WF does not completely mirror that of the overpotential values (**Figure 19B**). This also means that the reducing power (WF) alone cannot explain the trends in the catalytic activity, but there are additional factors to consider [116].

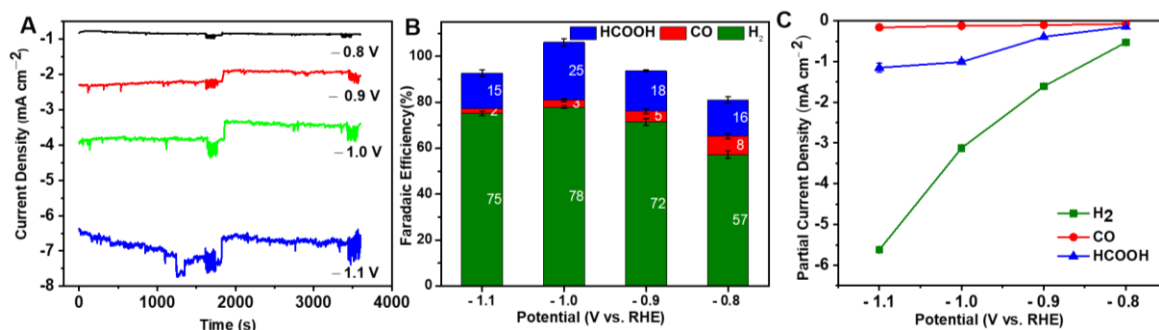


Figure 26. Electrochemical CO₂ reduction performance of physically mixed Au and Sn electrode: (A) total current density as a function of time at various potentials, (B) Reduction potential dependence of Faradaic efficiency and (C) partial current density.

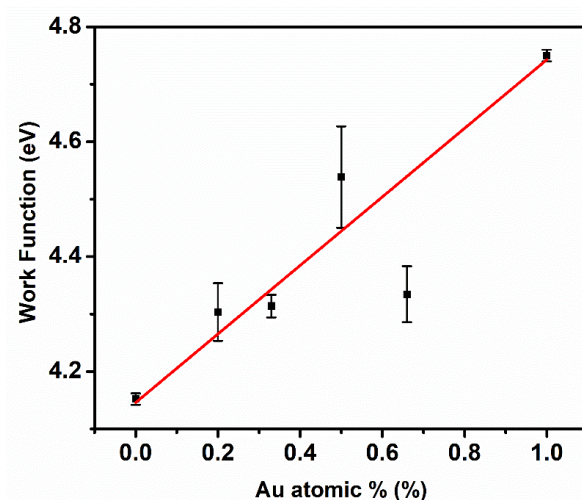


Figure 27. Variation of the work function of Au-Sn bimetallic NPs as a function of composition. Error bars represent the standard deviation obtained by studying three different samples for each composition.

Selective isotopic labeling experiments were performed to gain insights into the mechanism of CO₂ reduction on Au-Sn catalysts. We found that the produced CO and HCOOH originate from the aqueous CO₂ supplied primarily through fast equilibrium with the bicarbonate ions in the close vicinity of the electrode, rather than the purged CO₂ (**Figure 28**). Although the obtained trends are similar to those observed for CO₂ reduction on Au, Cu, and N-doped carbon surfaces [117–119], here we confirmed a similar pattern for the production of HCOOH.

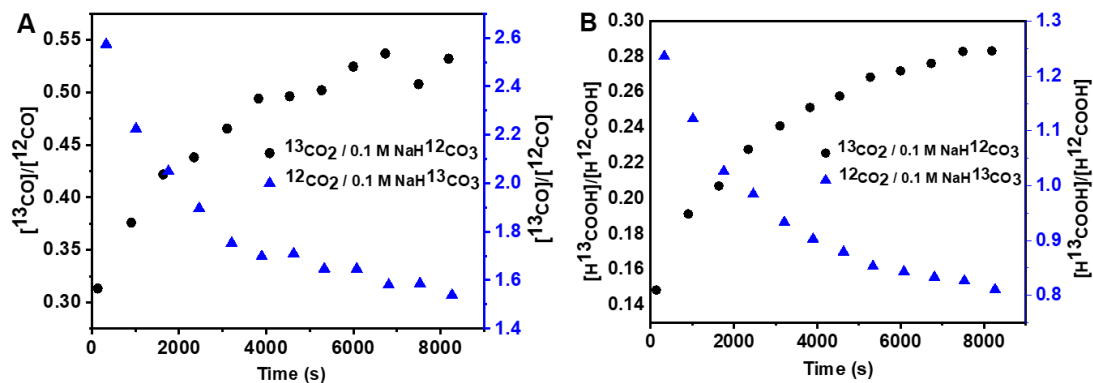


Figure 28. The ratio of the products formed during potentiostatic electrolysis at -1.1 V vs. RHE in a $^{12}\text{CO}_2$ -saturated 0.1 M $\text{NaH}^{13}\text{CO}_3$ electrolyte (right axis), and in a $^{13}\text{CO}_2$ -Saturated 0.1 M $\text{NaH}^{12}\text{CO}_3$ electrolyte (left axis) under non-equilibrium conditions. The products are (A) ^{13}CO and ^{12}CO , (B) H^{13}COOH and H^{12}COOH .

To gain further insights into the mechanism of the CO_2 reduction process, Raman spectra were collected under electrochemical control. This allows the direct observation of reaction intermediates and/or products, as well as monitoring of the changes in the chemical nature of the electrocatalysts during the electrochemical reaction [120]. The spectra collected between the open circuit potential (OCP) and -0.2 V vs. RHE exhibit only bands belonging to SnO_x (482 , ~ 623 , ~ 772 cm^{-1}) [121] and the O–H stretching mode of the adsorbed water (3000 – 3700 cm^{-1} , note that this band was almost independent of the potential) [122]. At -0.4 V vs. RHE, new bands started to appear, and their intensities gradually increased at more negative potentials. The SnO_x bands became more intense and slightly shifted due to surface defects as a result of partial reduction [123,124]. At potentials more negative than -0.8 V, it was quite difficult to collect Raman spectra because of the intense gas evolution. The assignments of all bands are shown in **Figure 29A**. At -0.8 V, the spectrum showed a strong band at 2880 cm^{-1} and several bands of medium and weak intensity in the region of 900 – 1774 cm^{-1} . These bands are similar to those observed during adsorption of formic acid on silver colloids and Cu [125,126], indicating the presence of formate-related and adsorbed bicarbonate species. While the spectra recorded for Au_1Sn_2 and Sn NPs were similar (**Figures. 29B and 30A**), higher overpotential was required for developing the bands on Sn NPs (**Figure 30B**), consistently with the observed shift in the onset potential on the LSV profiles. Importantly, none of these bands observed in N_2 -saturated 0.1 M Na_2SO_4 electrolyte, (**Figure 31A**) and on Au surfaces in CO_2 -saturated 0.1 M NaHCO_3 electrolyte (**Figure 31B**).

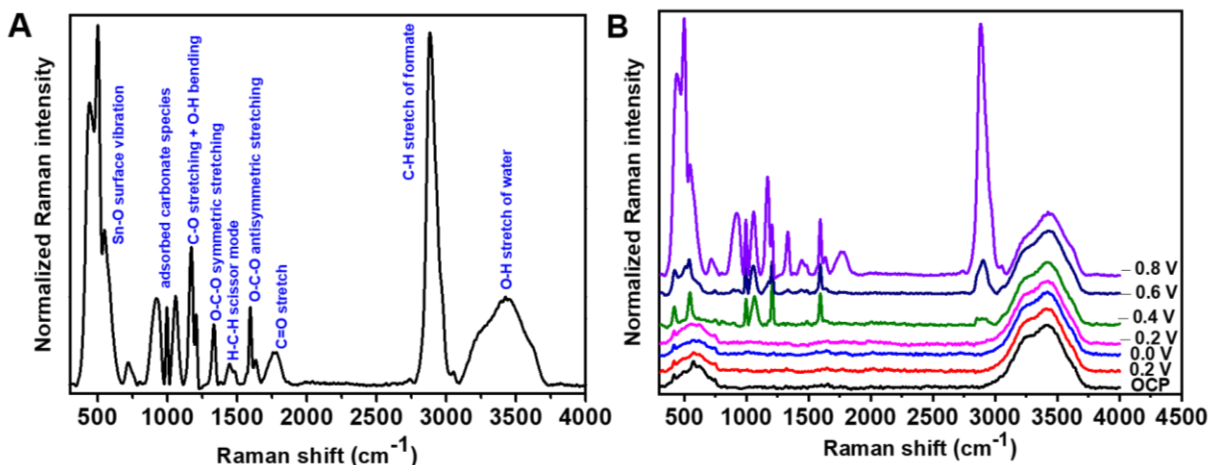


Figure 29. Raman spectra collected on Au_1Sn_2 catalyst in CO_2 -saturated 0.1 M NaHCO_3 : (A) at a potential of -0.8 V vs. RHE, (B) as a function of the employed bias potential.

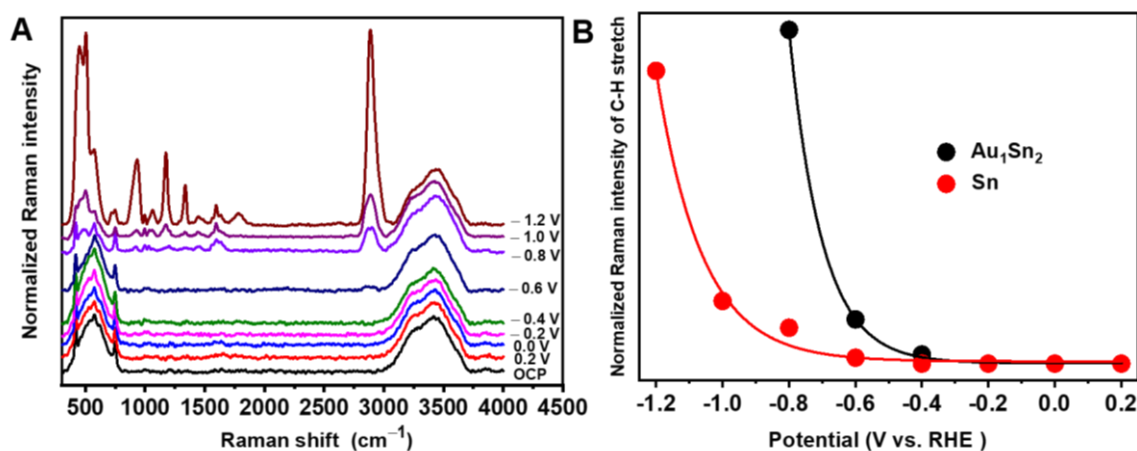


Figure 30. (A) Raman spectra collected on Sn NPs-coated electrode in CO_2 -saturated 0.1 M NaHCO_3 . (B) Potential dependence for the $\nu(\text{C-H})$ of formate anion at 2880 cm^{-1} band intensity on Au_1Sn_2 and Sn NPs-coated electrodes as a function of the employed bias potential.

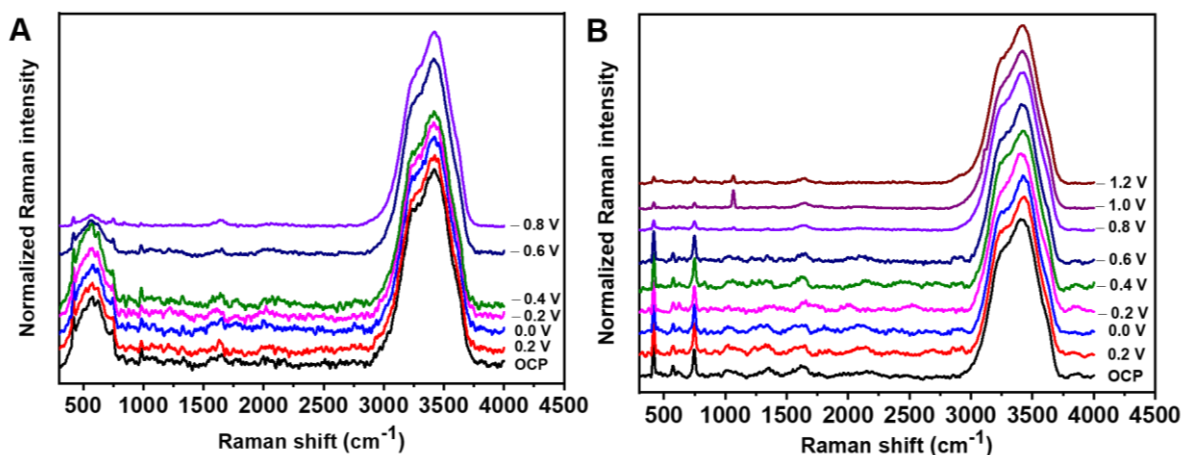


Figure 31. (A) Raman spectra collected on Au₁Sn₂ catalyst-coated electrode in N₂-saturated 0.1 M Na₂SO₄ at different potentials. (B) Raman spectra collected on Au NP-coated electrode in CO₂-saturated 0.1 M NaHCO₃ at different bias potentials.

5.2. Au-Ag Nanoalloys Activity for CO₂RR

5.2.1. Synthesis and Characterization of Au-Ag Alloy NPs

The morphology of the Au-Ag NPs and their monometallic counterparts was characterized by TEM. Monometallic Au and Ag NPs are spherical with an average diameter of 22.5 ± 2.2 and 25.8 ± 3.1 nm, respectively (**Figure 32**). **Figure 33** shows TEM images of Au-Ag NPs, where all particles are spherical. The average size increased from 24.5 ± 1.8 to 26.6 ± 2.4 , 31.5 ± 1.3 , and 32.1 ± 3.8 nm, in the series of the samples, as the amount of Ag increased. Ag@Au core-shell particles have also been prepared for comparison. The Au seed particles were smaller in this case, to keep the size of the core-shell NPs similar to their alloyed counterparts. TEM images of the core-shell NPs revealed an average size of 29.2 ± 4.2 nm (**Figure 34**).

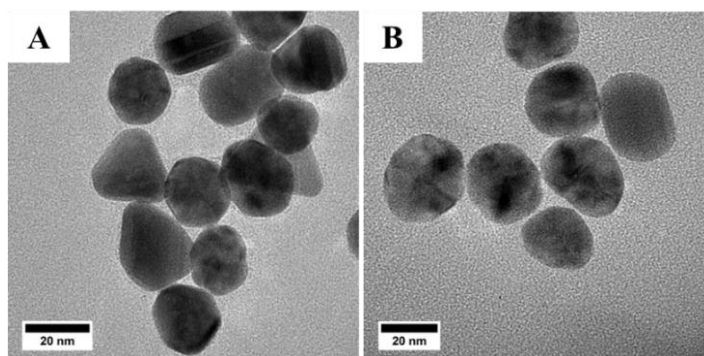


Figure 32. TEM images of (A) Au NPs and (B) Ag NPs.

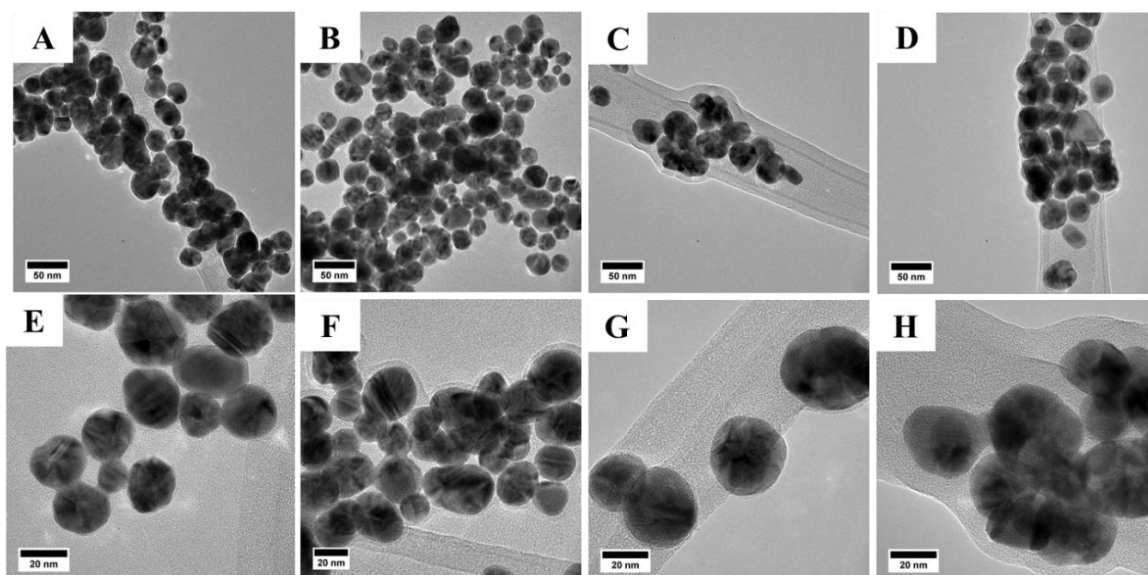


Figure 33. TEM images of Au-Ag alloy NPs with different compositions. (A) Au₈₀Ag₂₀, (B) Au₆₀Au₄₀, (C) Au₄₀Ag₆₀, and (D) Au₂₀Ag₈₀. (E–H) The corresponding magnified TEM images.

The crystal structure of the Au-Ag NPs was determined by XRD (**Figure 35**). The Au-Ag NPs exhibited similar patterns since gold and silver have almost the same lattice constant [127]. The peaks observed at $2\theta = 38.2^\circ$, 44.4° , 64.71° , and 77.7° can be assigned to the diffraction of the (111), (200), (220), and (311) planes from the fcc structure of gold and silver. As noted on the XRD patterns, the peak broadening gradually decreased with increasing Ag content in the alloy NPs, indicating an increase in the size of the crystalline domains. This observation was further confirmed by TEM images (**Figure 33**). The bulk composition of Au-Ag NPs was analyzed by EDX. The atomic ratios are consistent with the nominal values (**Table 6**).

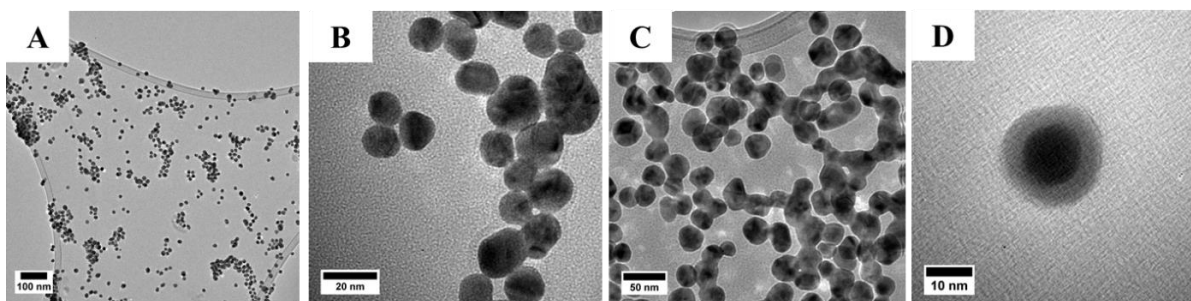


Figure 34. (A) TEM image of Au NPs (core) and (B) corresponding magnified TEM image with an insight figure of the size distribution histogram. (C) TEM image of Ag@Au core-shell NPs and (D) corresponding magnified TEM image of a single particle.

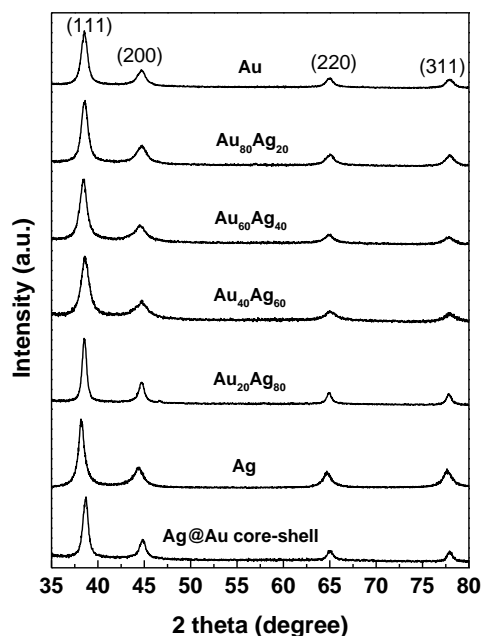


Figure 35. XRD patterns of Au-Ag alloy NPs with different compositions, Ag@Au core-shell NPs and the monometallic Au and Ag NPs.

Table 6. Bulk composition of Au-Ag bimetallic NPs as determined by EDX analysis.

Sample	Bulk composition (atomic %)	
	Au	Ag
Au₈₀Ag₂₀	81.8 ± 0.6	18.2 ± 0.6
Au₆₀Ag₄₀	59.4 ± 1.0	40.6 ± 1.0
Au₄₀Ag₆₀	40.0 ± 1.3	60.0 ± 1.3
Au₂₀Ag₈₀	21.3 ± 0.87	78.7 ± 0.87
Ag@Au core-shell	19.9 ± 0.70	80.1 ± 0.73

UV–vis spectroscopy was employed to characterize the optical properties of Au-Ag bimetallic NPs, thus proving the alloy formation. The monometallic NPs exhibit absorption bands at 520 nm and 413 nm, which are consistent with the characteristic localized surface plasmon resonance (LSPR) bands of Au and Ag, respectively (**Figure 36A**) [127]. UV–vis spectra of the Au-Ag NPs show only one absorption band for each of the bimetallic composition, located in between the LSPR band positions of Au and Ag NPs (**Figure 36A**). As the Au content increased in the NPs, their LSPR red-shifted in a linear fashion with the composition (**Figure**

36B). This indicates the formation of homogeneous Au-Ag alloys [127]. The absorption spectra of Ag@Au core-shell NPs showed an absorption band with a maximum at 408 nm (**Figure 36C**), which corresponds to the LSPR band of pure Ag NPs. Notably, at low Ag content, a weak band (shoulder) appeared at ~ 490 – 520 nm. This may be attributed to the irregular formation of Ag shell around the Au core, while at higher Ag concentration, the shoulder vanished. These observations suggest the formation of a thicker and uniform Ag shell.

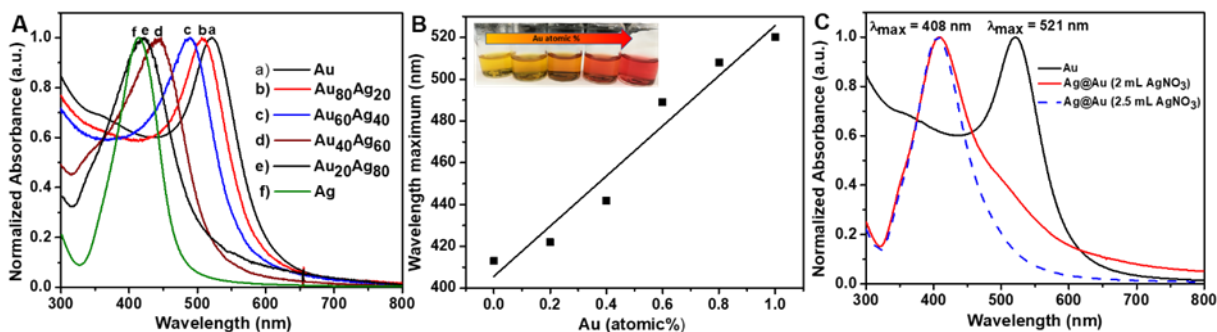


Figure 36. (A) Normalized UV–vis absorption spectra of Au, Ag, and Au-Ag alloy NPs with different compositions. (B) LSPR band maximum as a function of the Au content in the bimetallic NPs. The photograph in the inset shows the color change with the composition. (C) Normalized UV–vis absorption spectra of Ag@Au core-shell NPs.

5.2.2. Electrocatalytic CO₂ Reduction Activity

The electrochemical CO₂ reduction performance of Au-Ag NPs was first investigated by LSV, to identify the potential region of the reduction process. The onset potential in the CO₂-saturated 0.1 M NaHCO₃ was less negative than that in N₂-saturated Na₂SO₄ ($E = -0.38$ V in CO₂ and -0.62 V in N₂ vs. RHE, see **Figure 37A**). This indicates that an additional process occurs at less negative potential in the CO₂-saturated electrolyte, which is catalytically favored over the HER. Additionally, it competes with the CO₂R and in N₂-saturated electrolyte, only the HER takes place [85]. There was a monotonous shift in the onset potentials in the series of samples, which spans through a 300 mV range (**Figure. 37B**). To gain further insights into the mechanistic pathway of CO₂ reduction to CO on the Au₆₀Ag₄₀ electrocatalyst, it was further studied under various applied potentials and a Tafel plot of the CO partial current density (j_{CO}) was constructed (**Figure. 38**). A Tafel slope of 168 mV dec⁻¹ was obtained for Au₆₀Ag₄₀ catalyst in the low overpotential (kinetically controlled) regime, which indicates that the rate-determining step is the first electron transfer to CO₂ to form an adsorbed CO₂⁻ [128]. Previous studies on

polycrystalline Au and Ag electrodes in CO₂ saturated bicarbonate solution yielded Tafel slopes of 114 and 140 mV dec⁻¹ for polycrystalline Au and Ag electrodes, respectively which is similar to the value obtained for the alloyed sample in this study [129].

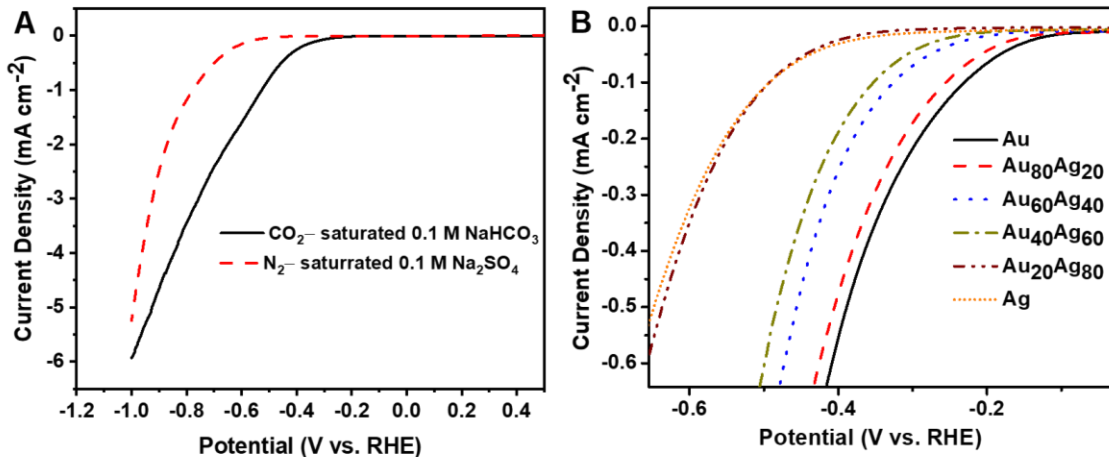


Figure 37. (A) LSV profiles of Au₆₀Ag₄₀ catalyst in CO₂-saturated 0.1 M NaHCO₃ (pH = 6.62) and N₂-saturated 0.1 M Na₂SO₄ (pH = 6.88), scan rate = 5 mV s⁻¹. (B) LSV profiles of Au-Ag alloys with different compositions in CO₂-saturated 0.1 M NaHCO₃ (pH = 6.62), scan rate = 5 mV s⁻¹. The loading was 0.53 mg cm⁻² in all cases.

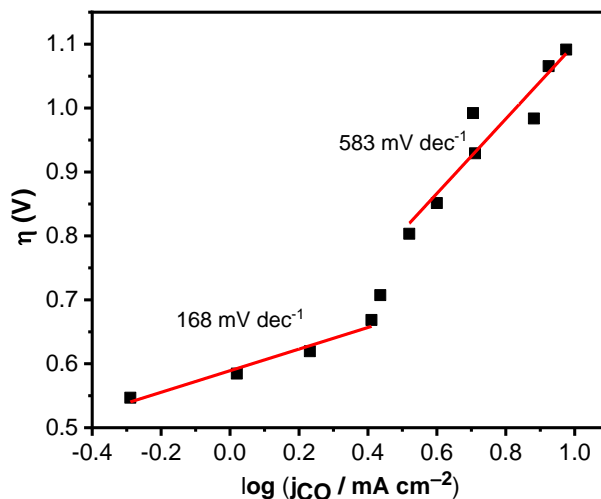


Figure 38. Tafel plot of the partial current density for CO on Au₆₀Ag₄₀ catalyst.

The currents measured during the CO₂ electrolysis on the Au-Ag electrocatalysts were stable over the time at all applied potentials (**Figure 39A**). Pure Ag showed the lowest total current density, while it increased with the Au content for the alloys up to the point where Au₆₀Ag₄₀ exhibited the highest value (**Figure 39B**). Furthermore, alloying resulted in a noticeable improvement in the stability at higher overpotentials. The major products were CO

and H₂ in all cases, with some minor traces of HCOOH. The FE values of CO and H₂, are shown as a function of the composition in **Figure 40**. The highest FE_{CO} of ~80% was observed at the Au NPs. For Au-Ag alloys, the conversion of CO₂ to CO improved with increasing Au content, while the FE of H₂ evolution simultaneously decreased. This indicates that the CO:H₂ ratio can be tuned by controlling the composition of the catalyst particles.

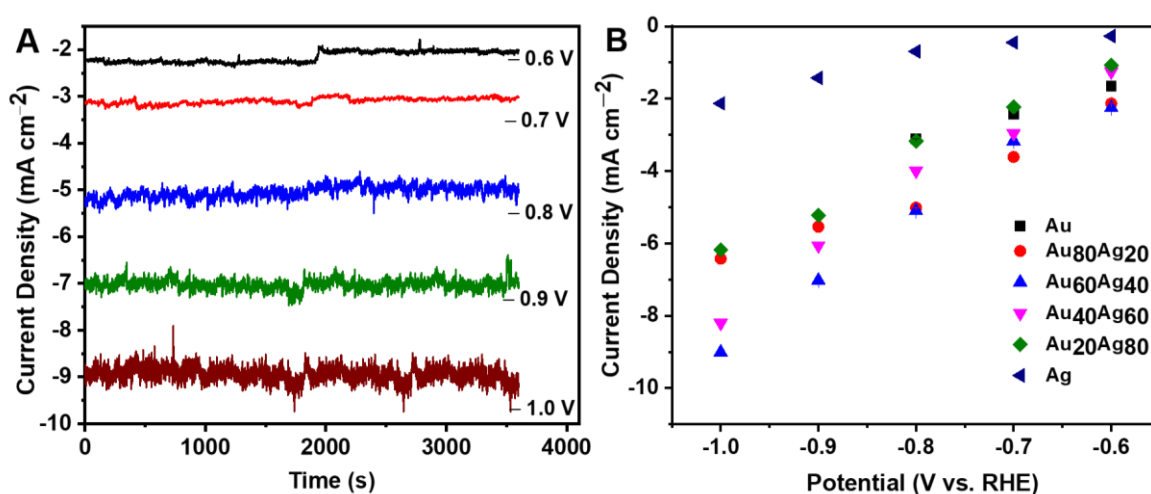


Figure 39. (A) Total current density for Au₆₀Ag₄₀ NPs as a function of time, a representative of electrolysis experiment at different potentials. At higher overpotentials, the current data becomes noisy because of the intense gas evolution that fluctuates the current. (B) Total current density for Au, Ag and Au-Ag alloy NPs as a function of applied potential. (C) Faradaic efficiency of CO and H₂ formation on Au-Ag alloy NPs with different compositions at -0.7 V vs. RHE.

As the next step, we studied the effect of the overpotential on the product distribution. Pure Au produced mostly CO (FE \geq 70%) even at less negative potentials, although with decreasing FE (**Figure 41A**). Interestingly, for the Au-Ag alloys, the product distribution showed very little dependence from the potential. The FE_{CO} stabilized between 55% and 60% at all applied potentials for Au₆₀Ag₄₀ catalyst (**Figure 41B**). On pure Ag, CO is produced with 16% FE at -0.6 V vs. RHE, which increased to 68.5% at more negative potential (-1.0 V vs. RHE) (**Figure 41C**) [130].

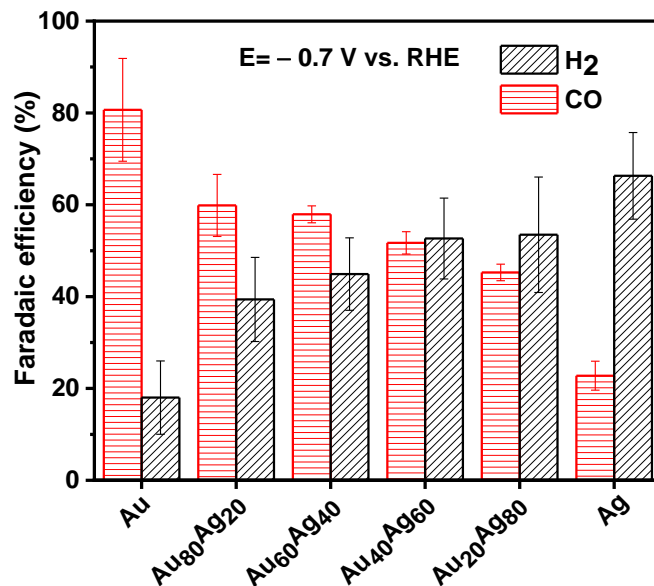


Figure 40. Faradaic efficiency of CO and H₂ formation on Au-Ag alloy NPs with different compositions at -0.7 V vs. RHE.

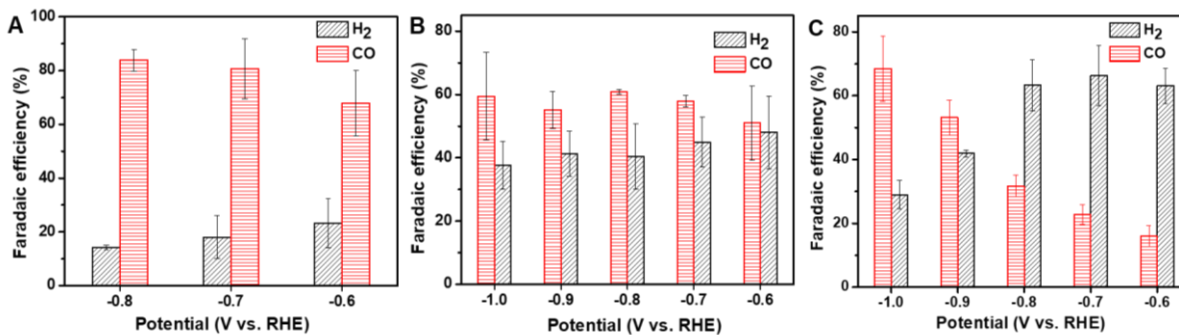


Figure 41. Faradaic efficiency of CO and H₂ on (A) Au, (B) Au₆₀Ag₄₀, and (C) Ag NPs as a function of the applied potential.

Partial current densities for CO and H₂ formation were plotted as a function of applied potential (to further analyze the activity of the different catalysts. j_{CO} gradually increased with increasing overpotentials **Figure 42A**). The trend for pure Au generally mirrors that of Au₈₀Ag₂₀ and Au₆₀Ag₄₀ at less negative potentials. In addition, the observed trends for j_{CO} followed the increase of Au incorporation up to -0.9 V vs. RHE, and then j_{CO} decreased for some alloys with further increasing the overpotential. This observation confirms that at more Au-rich alloys, the CO formation rates are higher. Importantly, the j_{H_2} was always higher for the alloyed samples, compared to the parent metals (**Figure 42B**). In addition, only very little composition dependence was seen in the HER currents.

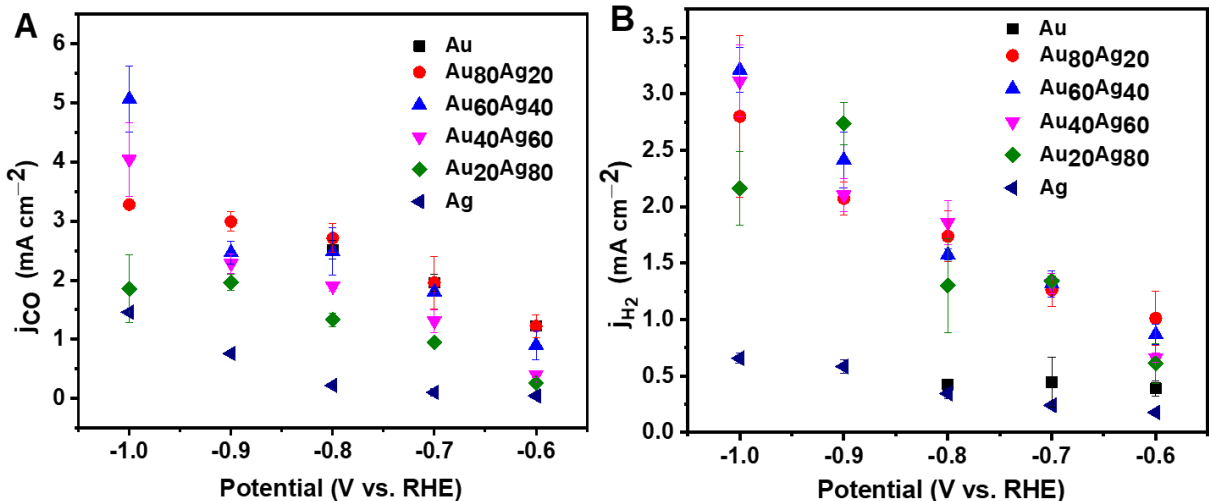


Figure 42. Electrochemical CO₂ reduction performance of Au-Ag alloys with different compositions. Partial current densities for (A) CO and (B) H₂ as a function of the applied potential.

To gain further insight on the factors behind the effect of composition on the electrocatalytic activity, we investigated the change of the electronic properties and correlated the electronic effects with the trends observed in the FE for CO and H₂. For transition metals, the interaction between the d-states (that are close to the E_F) and the intermediates of the CO₂RR determines the binding strength [131]. The higher the energy of d-states is, the stronger the interaction with the adsorbed species [132]. APS measurements were employed to determine the absolute WF and study the variation of d-states (energy of d-electrons) on Au-Ag alloys (**Figure 43**) [102]. The WF is defined as the minimum energy necessary to remove an electron from the E_F to the vacuum level (E_{VAC}). The electrons (d-electrons for transition metals) closest in energy to E_{VAC} are those at the E_F , thus in a metal, E_F marks the boundary between occupied and unoccupied states in a continuum of states [133]. The position of E_F of Au-Ag alloy NPs was determined and plotted versus the composition in **Figure 44**. The WF of pure Au and Ag NPs were 4.82 eV and 4.63 eV, respectively (**Figure 45A**), which is consistent with the reported values [102]. The E_F of Au-Ag alloys shifts downwards with increasing Au content; this is consistent with the j_{CO} trend. The pure silver particles are out of the linear trend, most likely because of differences in the surface oxide formation.

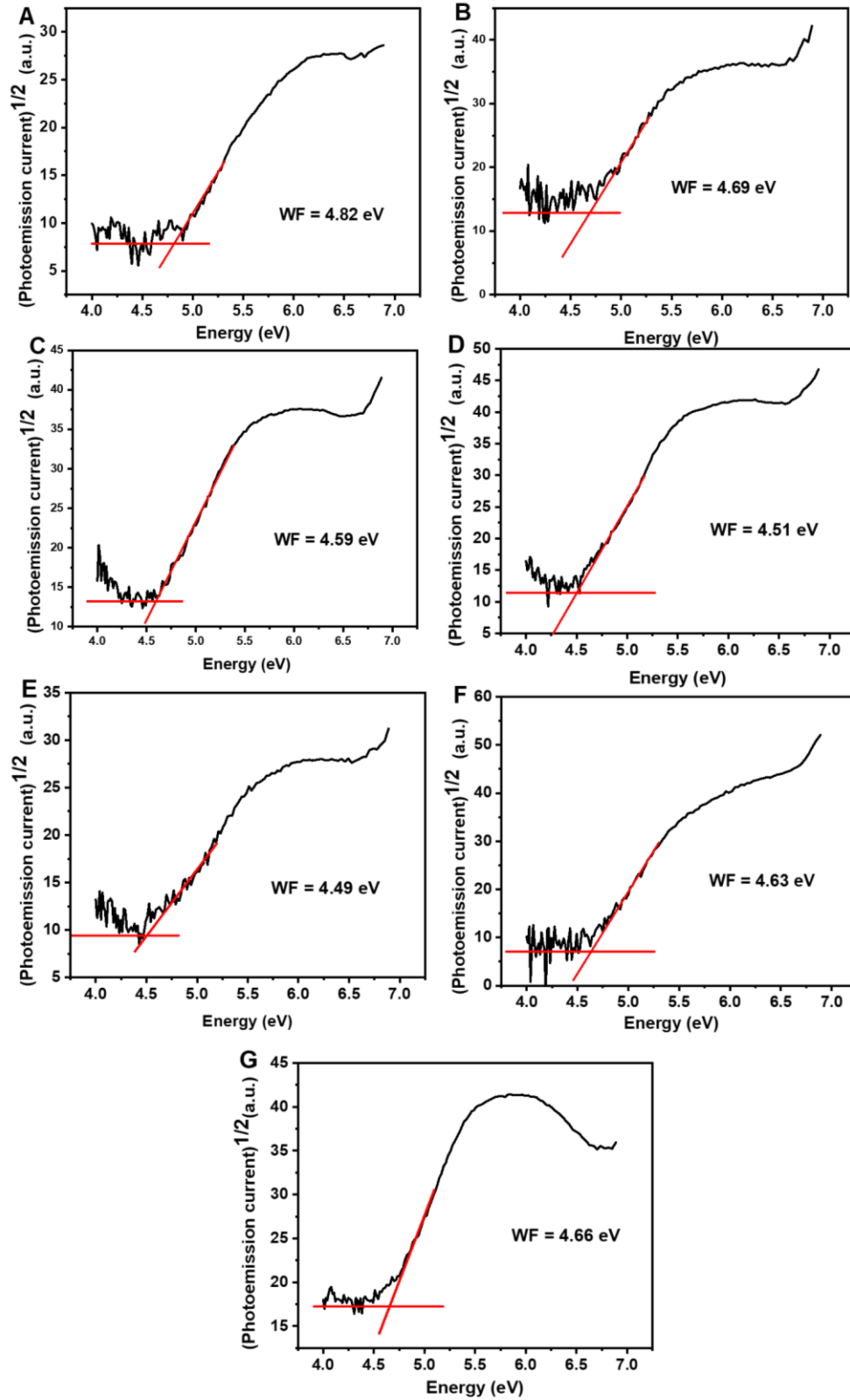


Figure 43. Square root photoemission curves for (A) Au, (B) Au₈₀Ag₂₀, (C) Au₆₀Ag₄₀, (D) Au₄₀Ag₆₀, (E) Au₂₀Ag₈₀, (F) Ag, and (G) Ag@Au core-shell NPs.

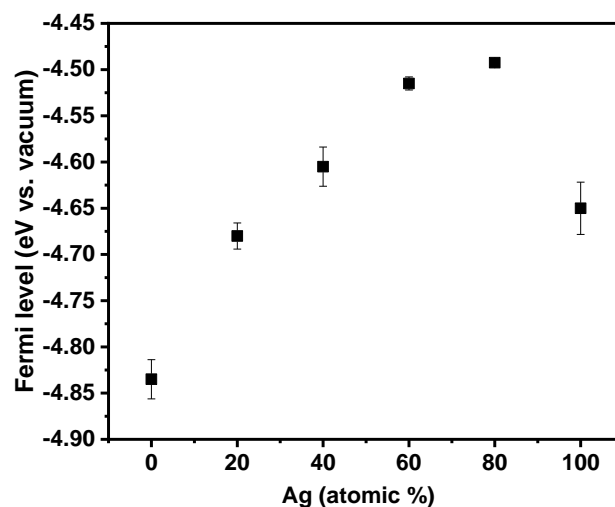


Figure 44. Electronic properties of Au-Ag alloys. Position of Fermi level of Au-Ag alloys as a function of Ag content.

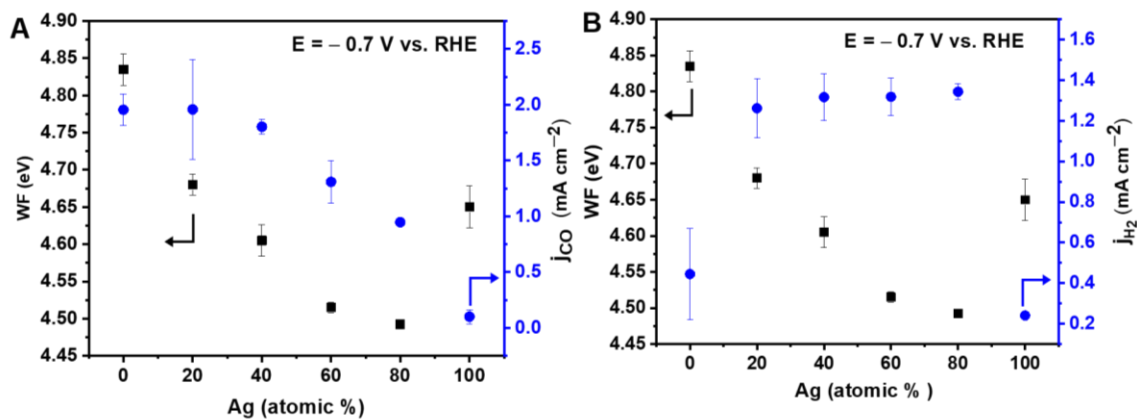


Figure 45. Electronic properties of Au-Ag alloys. (A) Work function of Au-Ag alloys versus Ag content (left axis) and CO partial current density versus Ag content (right axis). (B) Work function of Au-Ag alloys versus Ag content (left axis) and H₂ partial current density versus Ag content (right axis).

Based on the observed trend in the WF, the binding energy of *COOH and *CO on Au-Ag alloy surfaces might also decrease as the Au content increases, which facilitates the desorption of CO and resulting in the gradually increased CO₂R activity to CO (**Figure 45A**). The highest WF (the most downshifted E_F) was detected for pure Au NPs. Au is generally considered to have an optimal binding strength [134], which in turn results in the highest catalytic activity for CO formation. What is equally important, the HER activity was almost independent of the composition (**Figure 45B**). The Ag@Au core-shell catalyst produced CO with a FE of 68.7 %, versus 45.0% for alloy (Au₂₀Ag₈₀) NPs with the same bulk composition

(Table 6), at -0.7 V vs. RHE (Figure 46). Compared to pure Ag, the Ag@Au with Ag shell (with similar electronic structure) exhibited a different activity (68.7 % versus 25 % for FE_{CO} at -0.7 V vs. RHE). These trends indicate that neither electronic nor geometric effect *alone* can determine the electrocatalytic properties.

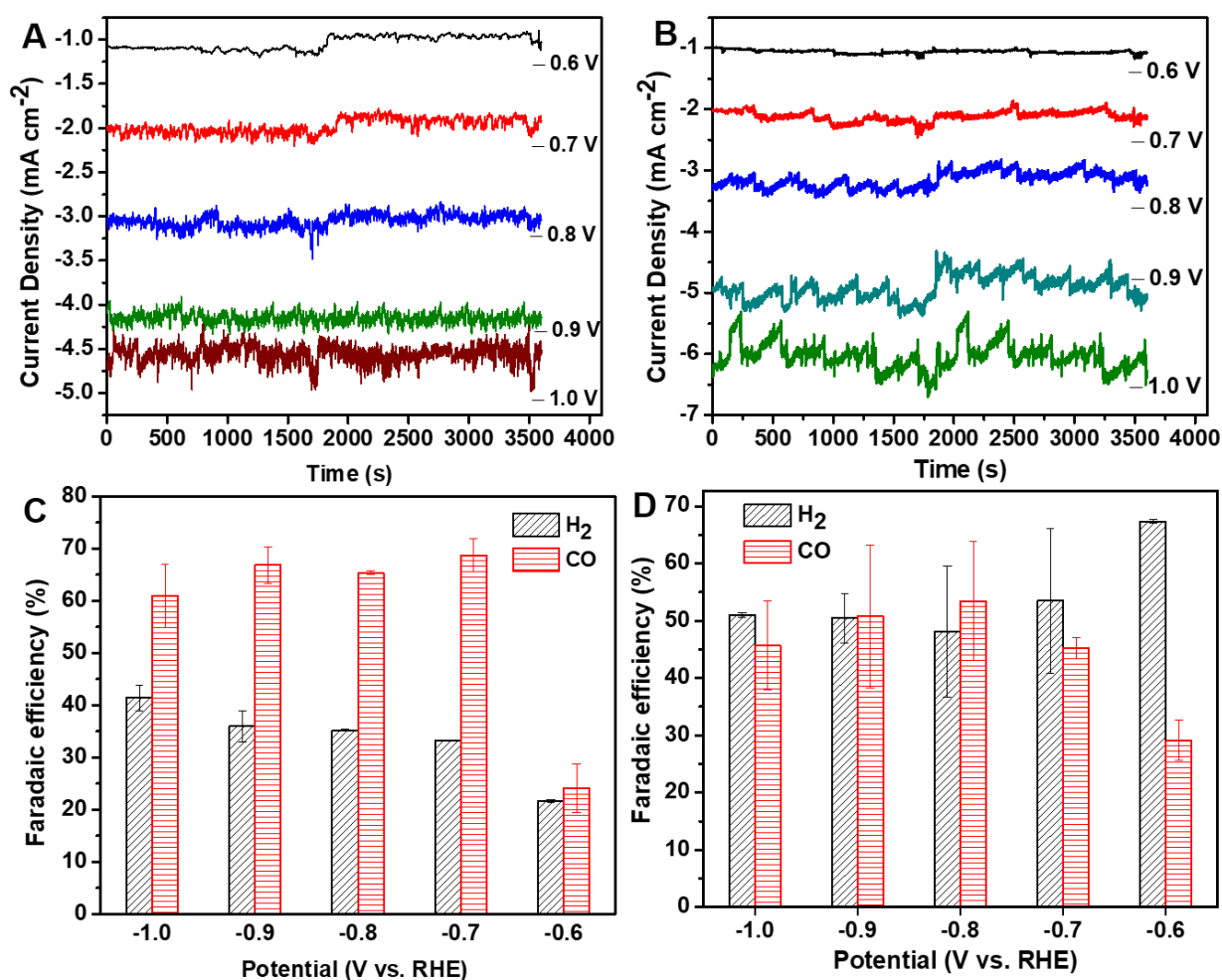


Figure 46. Comparison of CO₂ reduction activity of Ag@Au core-shell with that of Au₂₀Ag₈₀ alloy NPs. Total current density vs time for (A) Ag@Au core-shell, and (B) Au₂₀Ag₈₀ alloy NPs. Faradaic efficiency for CO and H₂ production vs applied potential on (C) Ag@Au core-shell, and (D) Au₂₀Ag₈₀ alloy NPs.

5.3. Au-Pb Bimetallic NPs Activity for CO₂RR

5.3.1. Synthesis and Characterization of Au-decorated Pb NPs

Au-Pb bimetallic NPs with different nominal compositions (i.e., Au₅Pb₉₅, Au₂₀Pb₈₀, Au₅₀Pb₅₀) were synthesized using a two-step synthesis approach. Starting with the formation of metallic Pb NPs, which act as nucleation seeds, followed by the galvanic replacement of Pb with Au. XRD measurements were carried out to determine the crystal structure of the Au-Pb NPs. The pure Pb showed diffraction peaks at $2\theta = 31.36, 36.34, 52.26, 62.26,$ and 65.33° corresponding to a face-centered cubic phase of Pb (JCPDS No.: 02-0799), and peaks at $2\theta = 28.68, 35.74, 44.41,$ and 54.93° for α -PbO (JPDS No.: 78-1666), as well as reflections for α -PbO₂ at $25.43,$ and 48.88° (JCPDS No.: 75-2414) (**Figure. 47**). The intensities of Pb, PbO, and PbO₂ peaks decreased notably with increasing Au concentration to 20 %, while the Au phase became more prevalent with further increasing the Au content (sample Au₅₀Pb₅₀). The pure Au exhibited a face-centered cubic phase. Importantly, these bimetallic samples are not-alloys (but rather particles containing nanosized domains of both metals); therefore, there is no shift in the reflection positions with an increase of the Au content (unlike for example, in the case of Au-Pt alloys [74]). Notably, the small relative intensity of the Pb-related diffractions suggests that the majority of these species are present in an amorphous phase (e.g., non-stoichiometric oxide).

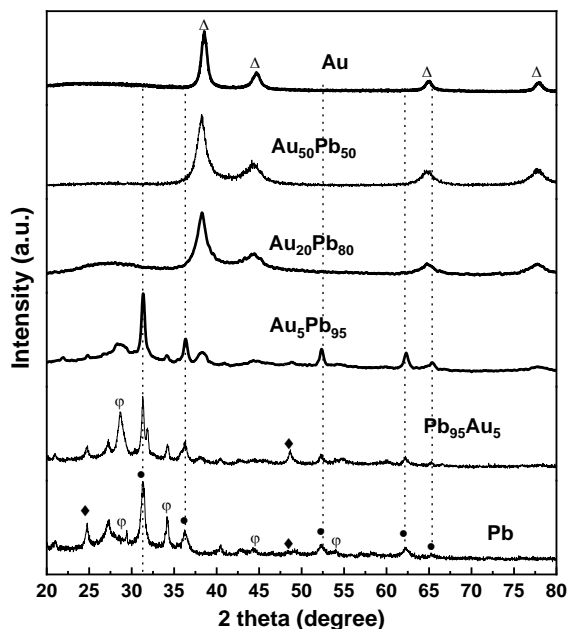


Figure 47. X-ray diffraction patterns of Au-Pb NPs and the parent metals. These marks indicate the diffractions corresponding to the respective crystal phases in the samples: (♦) α -PbO₂, (φ) α -PbO, (●) Pb (dot line), (Δ) Au (JCPDS No.: 04-0784).

TEM images of the as-prepared Au-Pb NPs show Au dots that are well-distributed on the surface of the Pb particles (**Figures 48A–C**) confirming the suggested formation mechanism. The average size of the bimetallic particles was 42 ± 5 nm for all compositions, slightly larger than that of the pure Pb NPs (40 ± 3.5 nm, **Figure 49A**). For the Au₅Pb₉₅ sample, which has the lowest Au content, the deposited Au NPs are mainly surrounding the Pb NPs (**Figure. 48D**).

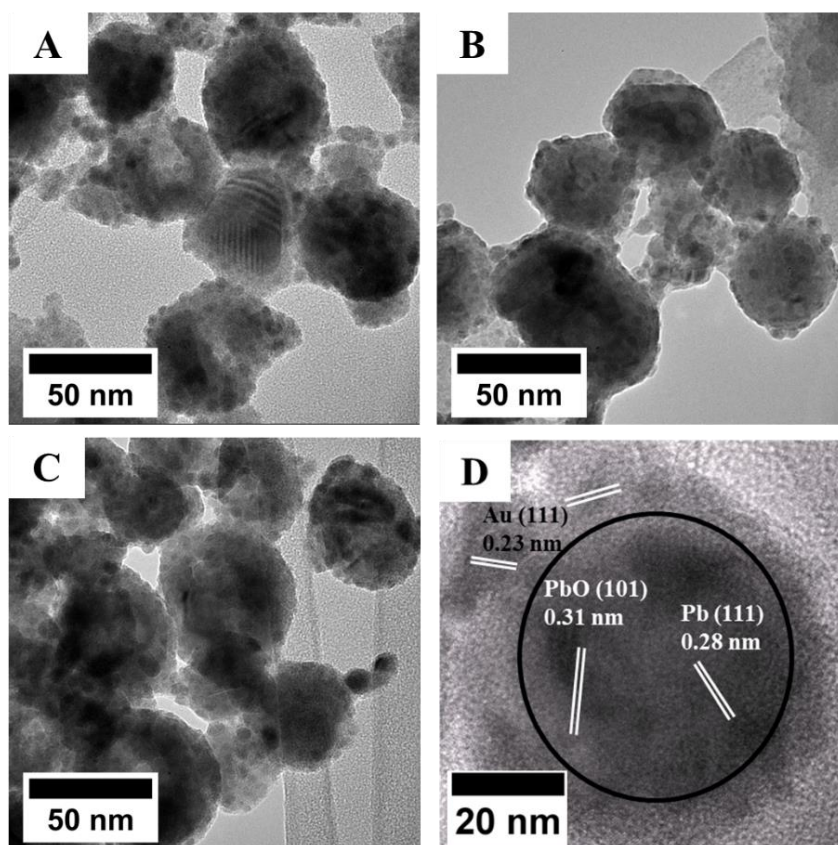


Figure 48. TEM images of (B) Au₅Pb₉₅, (C) Au₂₀Pb₈₀, (D) Au₅₀Pb₅₀ NPs, and (D) single particle of Au₅Pb₉₅, showing lattice fringes with a d spacing of 0.28 nm corresponding to the (111) plane of fcc Au, which are located around a core, which features lattice fringes with d-spacing values of 0.31 and 0.28 nm corresponding to (101) and (111) planes of α -PbO and Pb, respectively. The nominal compositions were used for the notation of the Au-Pb bimetallic system.

The Au-coverage on the top of Pb particles increases with increasing the Au content, thus more Au/Pb interfaces (**Figure 50**). The inverse structure (i.e., Au core, Pb shell, denoted as Pb₉₅Au₅) was also prepared with a similar composition to the most Pb-rich sample (Au₅Pb₉₅), and similar crystal phases were identified (**Figure 49C**).

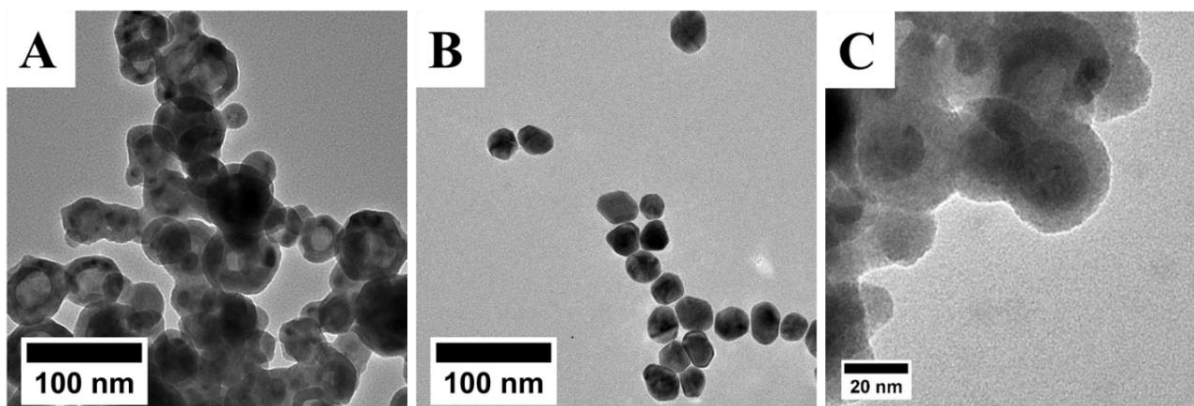


Figure 49. TEM images of: (A) Pb NPs ($d = 40 \pm 3.5$ nm), (B) Au NPs ($d = 29 \pm 3$ nm), and (C) Pb₉₅Au₅ ($d = 32.3 \pm 6$ nm).

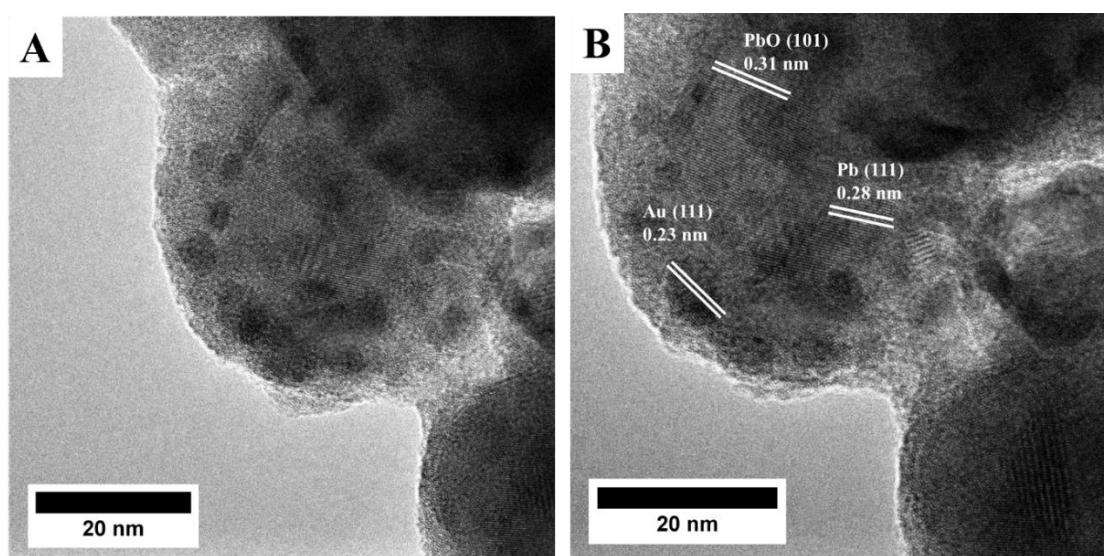


Figure 50. (A) TEM image of Au₅₀Pb₅₀ showing the deposited Au NPs on the surface of Pb NPs. (B) High-resolution TEM image of Au₅₀Pb₅₀ showing lattice fringes with a d spacing of 0.23 nm corresponding to the (111) plane of fcc Au, which are located on the top of Pb NPs, which features lattice fringes with d spacing values of 0.31 and 0.28 nm corresponding to (101) and (111) planes of α -PbO and Pb, respectively.

XPS was employed to characterize the chemical state of the elements at the NPs surface. The XPS survey scans show only Pb, Au, O, and C peaks (**Figure 51**).

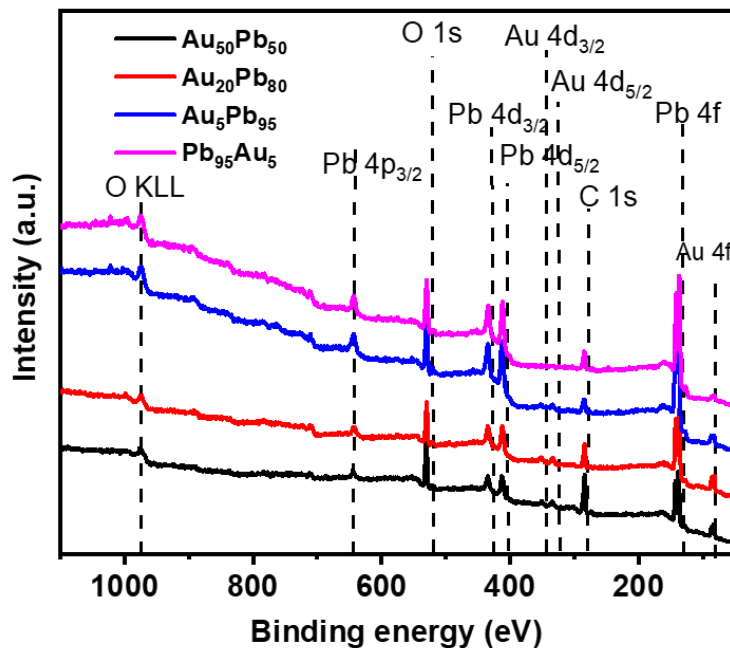


Figure 51. XPS survey scans of the Au-Pb bimetallic catalysts: Au₅₀Pb₅₀, Au₂₀Pb₈₀, Au₅Pb₉₅, and Pb₉₅Au₅.

The fitting of the high-resolution Pb 4f spectra shows that the native oxide is the predominant lead component on the surface of all four samples (**Figure 52**). The relative amount of the native Pb oxide (PbO_x) decreased from 94 to 91, and 72 % in the series of the samples with increasing the Au content (see also **Table 7**). The Au₅₀Pb₅₀ NPs heated in air exhibited only a Pb 4f peak at 138.45 eV (**Figure 53A**) that corresponds to Pb^{4+/2+}, which is likely due to the native oxide layer [45]. Besides, the lattice oxygen, carbonate, and hydroxide related oxygen were also detected (**Figure 53B**). While discussed in detail below, we already mention here that after a 10 h electrolysis experiment, there was no shift in the Pb 4f peak, indicating no change in the oxidation state. The percentage of PbO_x decreased from 77 to 70 %, and the Au content increased from 23 to 30 %. When mild Ar⁺ sputtering was employed, the metallic Pb⁰ 4f peak at 136.86 eV became visible, and the amount of lattice oxygen increased at the expense of carbonate (**Figure 53B**). This confirms the presence of the metallic Pb and some non-stoichiometric PbO_x structures beneath the surface layer. EDX data describing the bulk composition are listed in **Table 7**, together with the surface composition obtained from XPS.

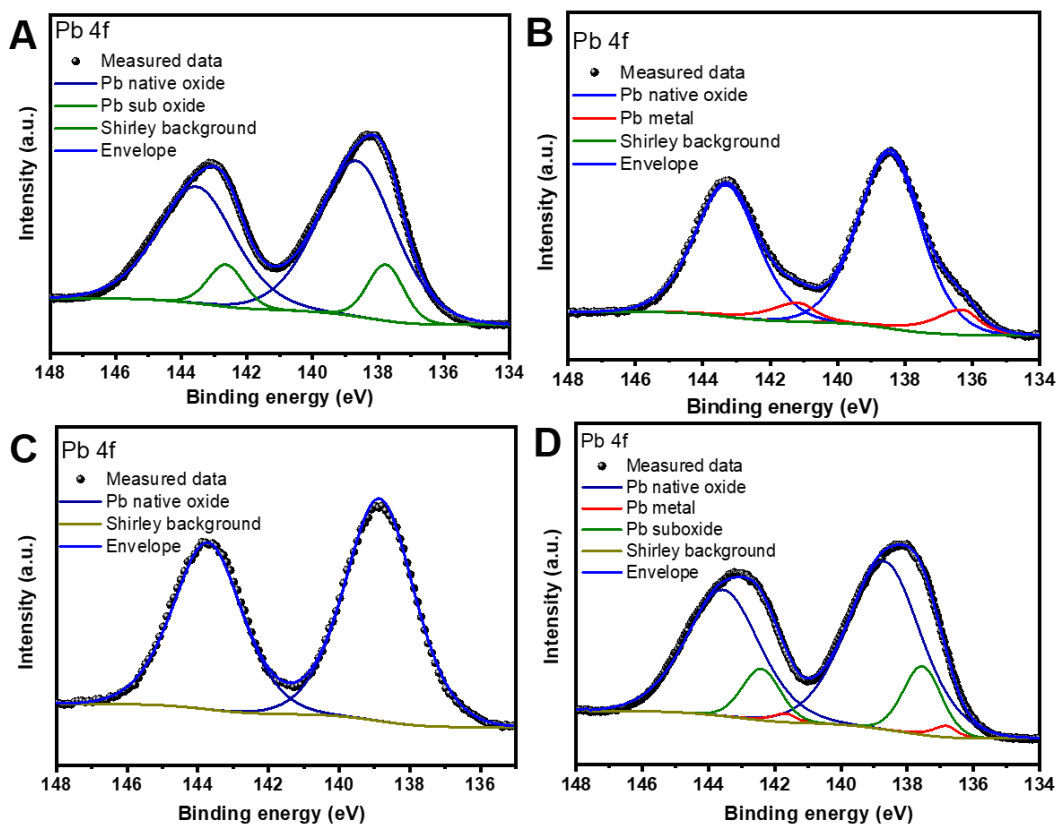


Figure 52. High-resolution XPS spectra of the Pb 4f peaks: (A) Au₅Pb₉₅ (B) Au₂₀Pb₈₀ (C) Au₅₀Pb₅₀, and (D) Pb₉₅Au₅.

Table 7. Bulk and surface composition of Au-Pb bimetallic NPs.*

Sample	EDX Bulk composition (atomic %)		XPS Surface Composition (atomic %)		
	Au	Pb	Au	Pb ⁰	PbO _x
Pb ₉₅ Au ₅	3.9	96.1	3.8	1.8	94.4
Au ₅ Pb ₉₅	5.1	94.9	8.8	0.0	91.2
Au ₂₀ Pb ₈₀	21.4	78.6	20	8.2	71.8
Au ₅₀ Pb ₅₀	60.1	39.9	23	0.0	77

*XPS shows the ratio between Au and Pb-oxide species on the surface.

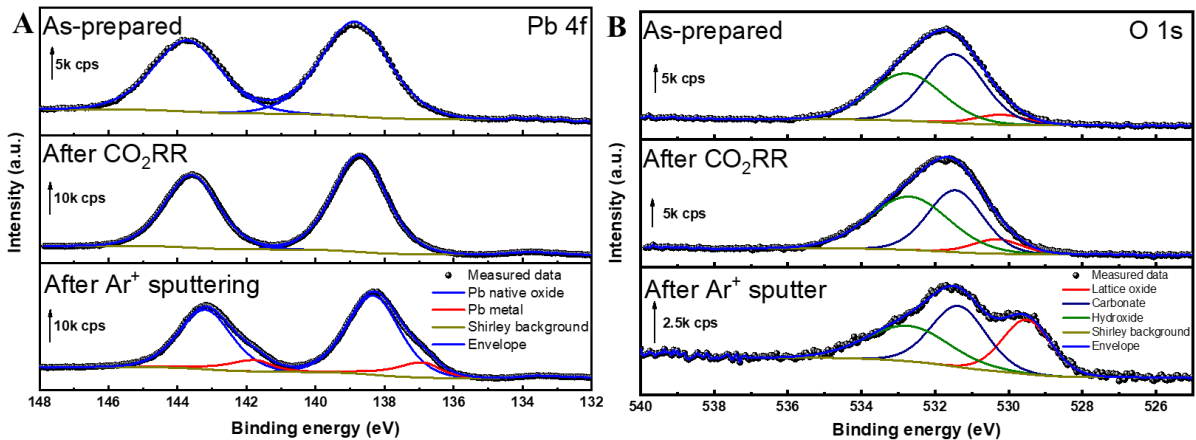


Figure 53. High-resolution XP spectra of the (A) Pb 4f peaks and (B) O 1s peaks for Au₅₀Pb₅₀ catalyst; before and after CO₂ electrolysis in CO₂-saturated 0.5 M KHCO₃ (pH = 7.2) at -1.07 V vs. RHE for 1 h, and after Ar⁺ sputtering.

5.3.2. Electrocatalytic CO₂ Reduction Activity

The electrochemical reduction of CO₂ on Au-Pb NPs was investigated first by LSV to identify the onset potential of the reduction process. LSV curves were recorded in CO₂-saturated 0.5 M KHCO₃ (pH = 7.2) and N₂-saturated 0.5 M Na₂SO₄ (pH = 7.5) to ensure a similar pH. The onset potential in the CO₂-saturated 0.5 M KHCO₃ was less negative compared to that in N₂-saturated solution ($E = -0.73$ V in CO₂ vs. -0.88 V in N₂ vs. RHE, see **Figure 54**). This indicates that in the CO₂-saturated electrolyte, an additional process besides the HER occurs at a less negative potential.

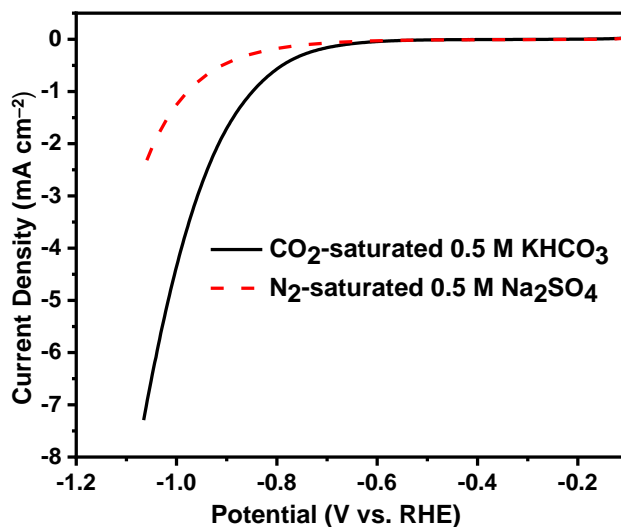


Figure 54. Representative LSV profiles of Au₅₀Pb₅₀ catalyst in CO₂-saturated 0.5 M KHCO₃ (pH = 7.2) and N₂-saturated 0.5 M Na₂SO₄ (pH = 7.5), scan rate = 5 mV s⁻¹.

The comparison of the voltammetric curves of the different Au-Pb NPs is presented in **Figure 55A**. There is a clear trend in the onset potentials in the series of samples, following the change in the composition. The least negative potential was witnessed for Au, while the most negative for Pb (all the bimetallic electrodes lied in between). In the case of the samples heat-treated in Ar, no clear trend was observed, and the onset potential values of the Au-rich catalysts (Au₅₀Pb₅₀ and Au₂₀Pb₈₀) were more negative than those recorded for samples heated in air (Figure 55B). This observation can be rationalized by the catalytically active nature of PbO_x sites. CVs profiles were also recorded for all samples to characterize the surface qualitatively. For example, the CV traces of the Au₂₀Pb₈₀ electrode showed the characteristic oxidation and reduction peaks of both Pb and Au, confirming the presence of both elements on the surface (Figure 56).

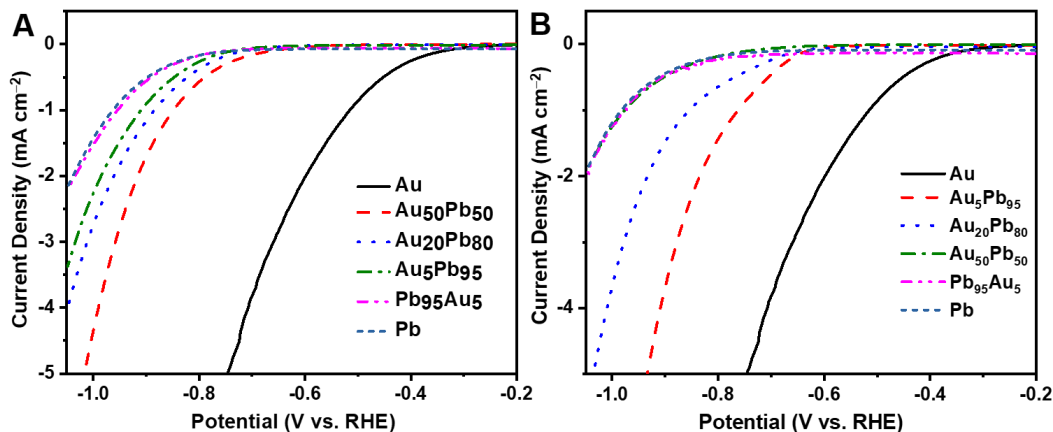


Figure 55. LSV profiles of Au-Pb NPs with different compositions in CO₂-saturated 0.5 M KHCO₃ (pH= 7.2) stabilized after multiple cycles. Scan rate = 5 mV s⁻¹. (A) The layers were heated in air atmosphere at 280 °C, and (B) The layers were heated in Ar atmosphere at 280 °C. The loading was 0.48 mg cm⁻² in all cases.

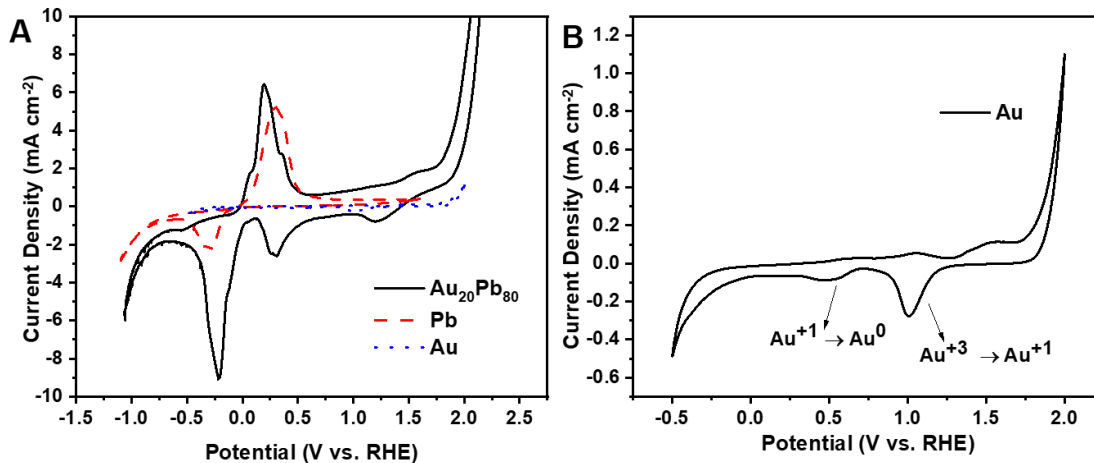


Figure 56. Cyclic voltammograms of the Au₂₀Pb₈₀, Pb, and Au NPs used for the qualitative characterization in CO₂-saturated 0.5 M KHCO₃ with a scan rate of 50 mV s⁻¹, the potential was scanned between -1.1 and 2.0 V vs. RHE. Each cycle starts with an anodic scan followed by a cathodic scan.

The CO₂ reduction performance of the bimetallic NPs was explored under chronoamperometric conditions. Analysis of the electrolysis products confirmed the formation of CH₄ (highly reduced C₁ product) besides CO and HCOOH, whereas the remaining charge was attributed to the HER. First, we investigated the effect of the overpotential on the product distribution. Pure Au produced mainly CO (FE ≥ 70 %) with very little dependence on the applied potential, and some minor traces of HCOOH was also detected (**Figure 57B**). Pure Pb generated HCOOH and H₂, and the maximum FE_{HCOOH} was 78 % at -1.07 V vs. RHE, while the FE_{H₂} was 22 % (**Figure 57D**).

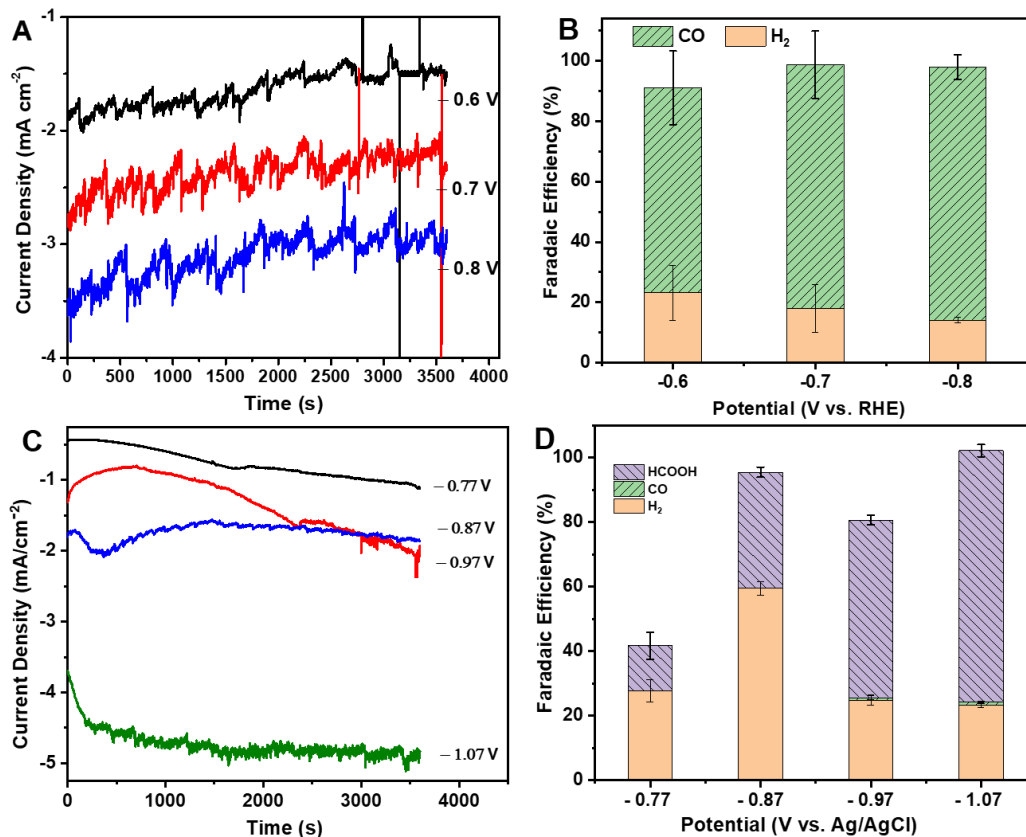


Figure 57. Electrochemical CO₂ reduction activity of Au NPs (A) total current density as a function of time at various potentials, (B) H₂, and CO Faradaic efficiencies. Electrochemical CO₂ reduction activity of air-heated Pb: (C) total current density as a function of time at various potentials, and (D) H₂, CO, and HCOOH Faradaic efficiencies measured in CO₂-saturated 0.5 M KHCO₃.

The current density values recorded for the Au₅₀Pb₅₀ catalyst at different potentials are shown in **Figure 58** as an example, together with the FE values for the various products. At -1.07 V vs. RHE, CH₄ with a FE of 2.8% was produced. At more negative potentials (-1.17 V vs. RHE), we did not observe a further increase in the FE_{CH₄}, but HER activity increased. Three parallel long-term electrolysis experiments were carried out at -1.07 V vs. RHE (**Figure 59A**). A stable current of -10.8 ± 0.5 mA cm⁻² was achieved with CO, HCOOH, and CH₄ FEs of 25.7 ± 8.0 , 25.5 ± 0.7 , and 2.8 ± 0.4 %, respectively, during the 3 h electrolysis. Smaller FE values were seen at the same potential for the Au₅₀Pb₅₀ catalyst heated in Ar (with the parallel rise of the competing HER), for all CO₂ reduction products (**Figure 59B**).

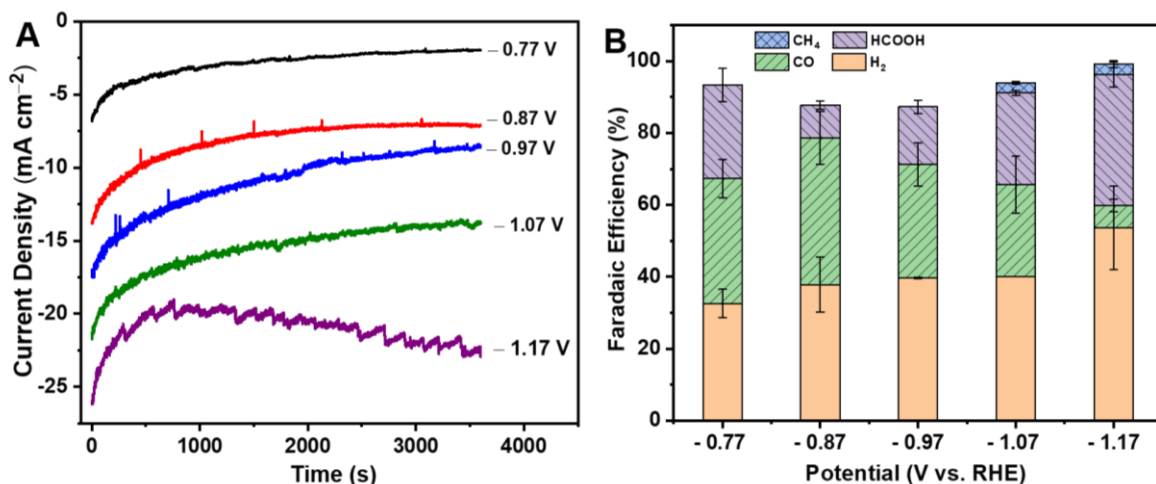


Figure 58. Electrochemical CO₂ reduction activity of the Air-heated Au₅₀Pb₅₀ catalyst: (A) total current density as a function of time at various potentials, and (B) H₂, CO, HCOOH, and CH₄ Faradaic efficiencies at different applied potentials.

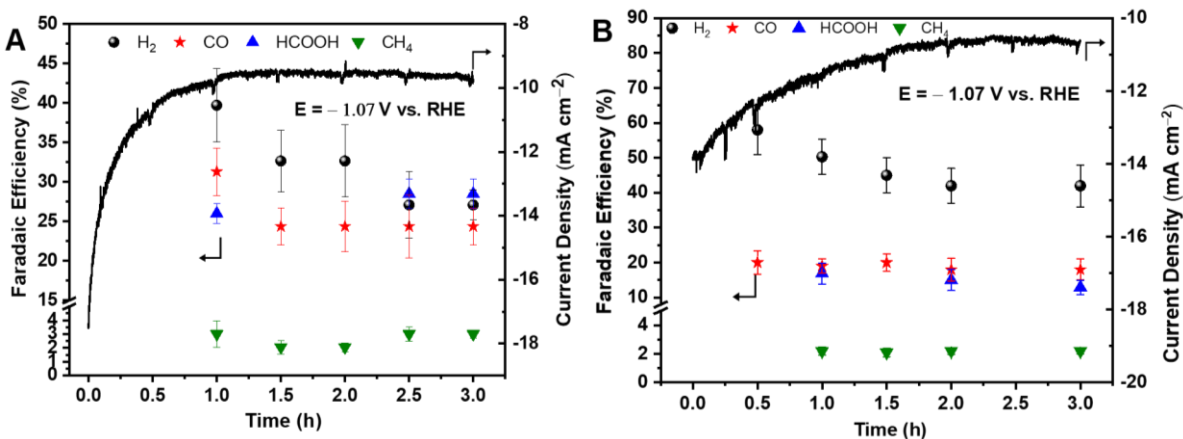


Figure 59. Electrochemical CO₂ reduction activity of the Au₅₀Pb₅₀ catalyst, 3 h CO₂ electrolysis measured in CO₂-saturated 0.5 M KHCO₃ at -1.07 V vs. RHE: (A) The layers were heated in Ar atmosphere at 280 °C, and (B) The layers were heated in Ar atmosphere at 280 °C.

By changing the composition to $\text{Pb}_{95}\text{Au}_5$ (**Figure 60**), low current densities $< -0.5 \text{ mA cm}^{-2}$ were achieved in the less negative potential region (-0.77 to -0.87 V vs. RHE), associated mainly to HER. At potentials more negative than -0.87 V vs. RHE , not only the FE_{HCOOH} increased but also CH_4 was produced with 4.8% FE, achieving a FE_{tot} of $\sim 100 \%$ (at -1.07 V vs. RHE). For $\text{Au}_5\text{Pb}_{95}$ and $\text{Au}_{20}\text{Pb}_{80}$ catalysts (**Figure 61**). CO was generated with a FE of 1 – 2 % at different potentials. The FE_{HCOOH} increased with increasing the potentials, but H_2 evolution exhibited an opposite trend on $\text{Au}_5\text{Pb}_{95}$ electrode. $\text{Au}_{20}\text{Pb}_{80}$ electrode shows a very little dependence of the potential. CH_4 was not detected at potentials less negative than -1.07 V vs. RHE .

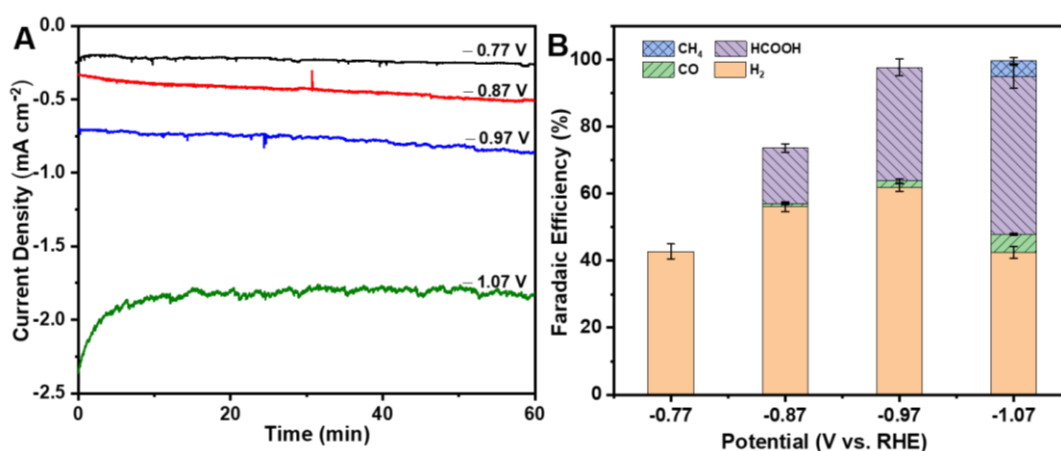


Figure 60. Electrochemical CO_2 reduction activity of the $\text{Pb}_{95}\text{Au}_5$ catalyst: (A) total current density as a function of time at various potentials, and (B) H_2 , CO, HCOOH, and CH_4 Faradaic efficiencies in CO_2 -saturated 0.5 M KHCO_3 . The layers were heated in air atmosphere at $280 \text{ }^\circ\text{C}$.

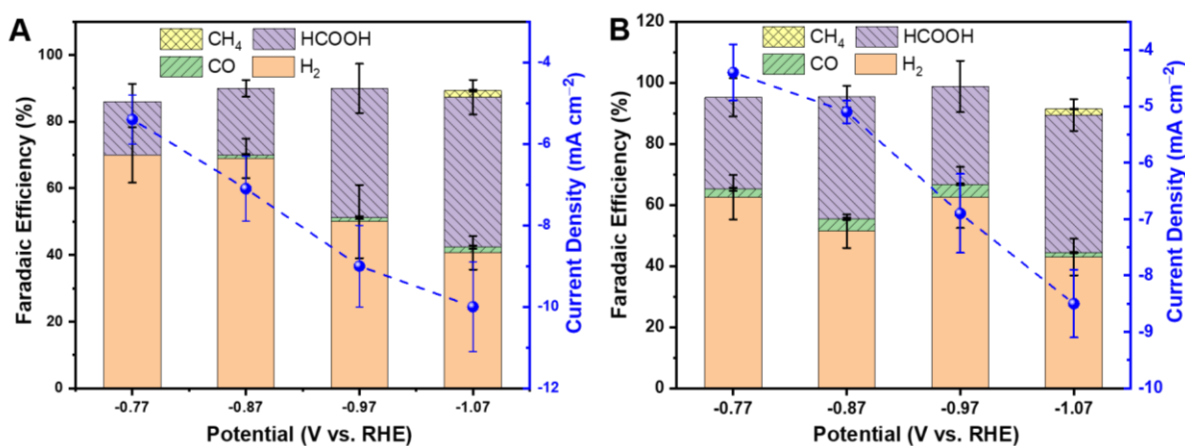


Figure 61. Electrochemical CO_2 reduction activity of (A) $\text{Au}_5\text{Pb}_{95}$ and (B) $\text{Au}_{20}\text{Pb}_{80}$ catalysts: showing total current density and H_2 , CO, HCOOH, and CH_4 Faradaic efficiencies at different applied potentials for 1h CO_2 electrolysis measured in CO_2 -saturated 0.5 M KHCO_3 . The layers were heated in air atmosphere at $280 \text{ }^\circ\text{C}$.

To investigate the effect of electrode composition (especially on CH_4 formation which represents the reduction process that requires the transfer of 8 electrons), we compared the product distribution and partial current densities during CO_2 electrolysis at -1.07 V vs. RHE. A relatively stable current density was measured in all cases, and its value increased with increasing the Au content (**Figure 62A** and **Figure 63**). The j_{CO} reached -3.2 mA cm^{-2} on $\text{Au}_{50}\text{Pb}_{50}$ heated in air (**Figure 62C**), whereas for the other catalysts, the CO formation dropped to ~ -0.16 mA cm^{-2} . The j_{H_2} declined linearly with increasing the Pb content, which is characteristic of Pb [86]. The j_{CH_4} increased from -0.15 to -0.16 , -0.24 , and -0.33 mA cm^{-2} for $\text{Pb}_{95}\text{Au}_5$, $\text{Au}_5\text{Pb}_{95}$, $\text{Au}_{20}\text{Pb}_{80}$, and $\text{Au}_{50}\text{Pb}_{50}$, respectively (**Figure 62B**). This trend suggests that comparable amounts of Au and Pb are needed at the surface to ensure high reaction rates (see also **Table 7**). Notably, the formation rate of CH_4 was always higher on samples heated in Air, compared to their Ar-heated counterparts.

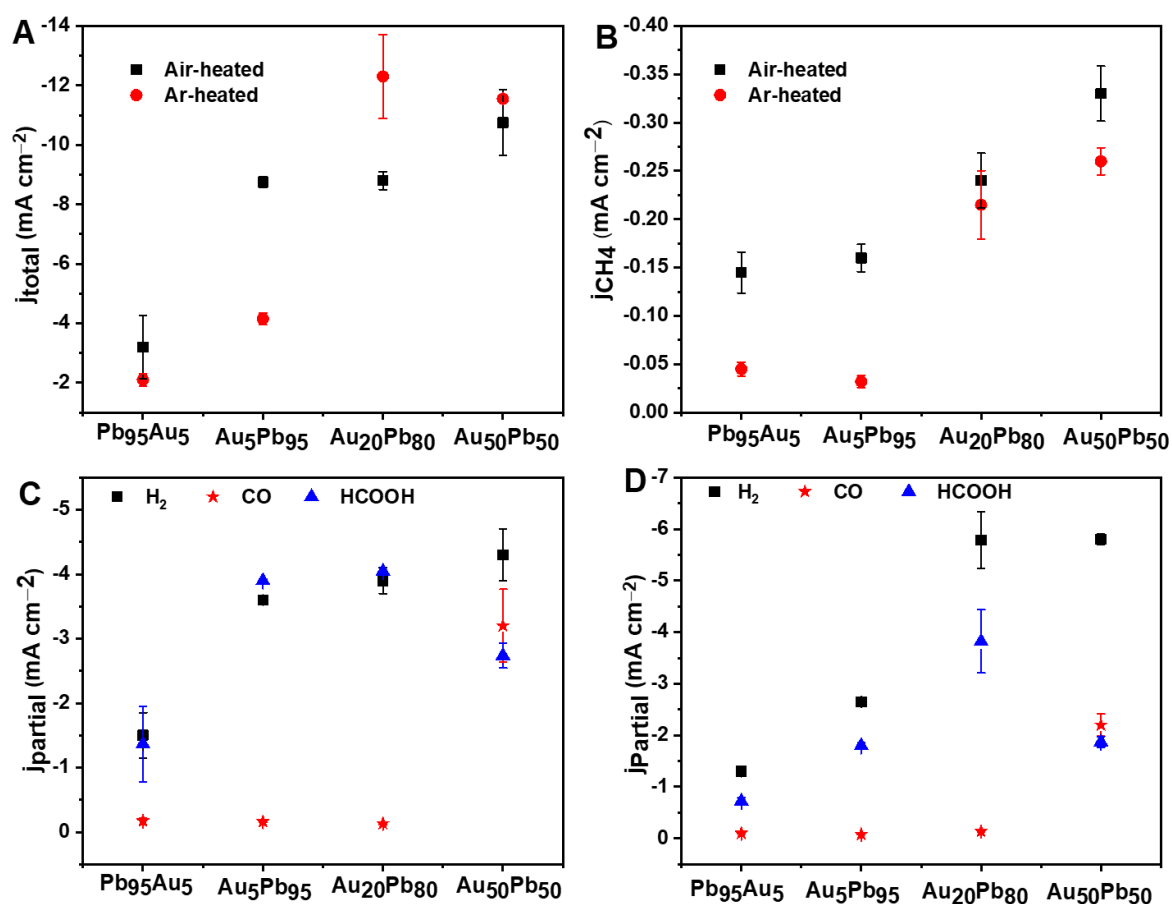


Figure 62. Electrochemical CO_2 reduction activity of the Au-Pb catalysts at -1.07 V vs. RHE: (A) Total current density, (B) the partial current density of CH_4 as a function of composition. The partial current density of H_2 , CO , and HCOOH on (C) Air-heated catalysts, and (D) Ar-heated samples.

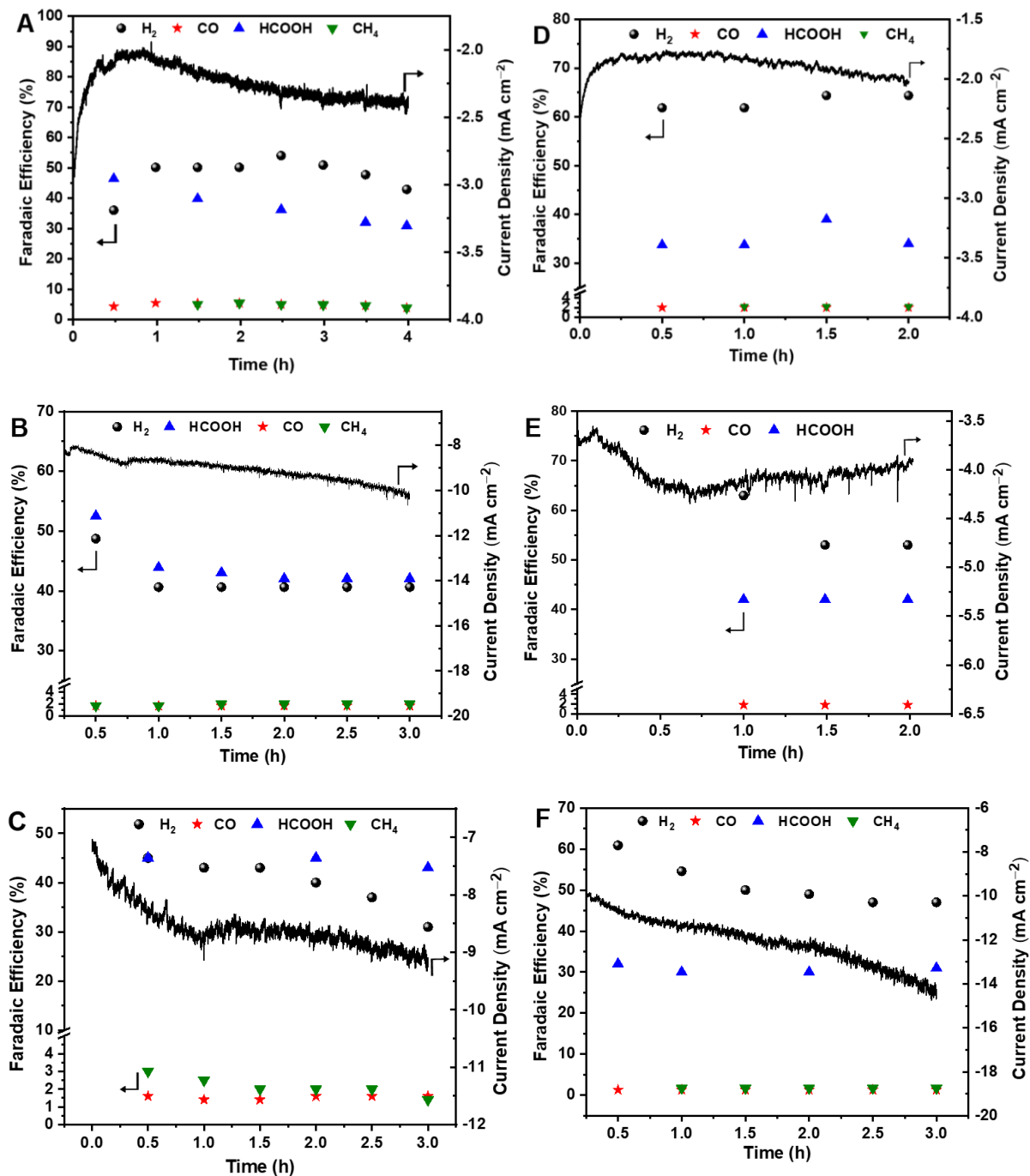


Figure 63. Electrochemical CO₂ reduction performance of the Au-Pb catalysts: Faradaic efficiency for H₂, CO, HCOOH, and CH₄, and total current density values measured during 3 h electrolysis at -1.07 V vs. RHE in CO₂-saturated 0.5 M KHCO₃ for air-heated samples; (A) Pb₉₅Au₅, (B) Au₅Pb₉₅, (C) Au₂₀Pb₈₀. (D – F) corresponding Ar-heated samples.

A ten-hour electrolysis was performed at -1.07 V vs. RHE to assess the stability of $\text{Au}_{50}\text{Pb}_{50}$ catalyst and verify the continuous production of CH_4 (**Figure 64**). The total current density stabilized at -13 mA cm^{-2} after 1 h and remained constant. The FE_{CH_4} varied within 2.8 – 2.1%. There was a drop in FE_{CO} to 17 % after 5 h. This might be due to the decrease in the reactant (CO_2) concentration, where the gas chromatography curve showed that the areas of CO and CO_2 peaks became comparable. The electrolyte was purged with CO_2 for 30 min, and then the flow was stopped before electrolysis. We performed an additional experiment with labeled $^{13}\text{CO}_2$ and $\text{KH}^{13}\text{CO}_3$, and the almost exclusive formation of $^{13}\text{CH}_4$ and ^{13}CO was verified (deduced from the $m/z = 17$ signal and the $m/z = 29$ signal, respectively), confirming that the detected CH_4 and CO both came from CO_2 reduction (**Figure 65**).

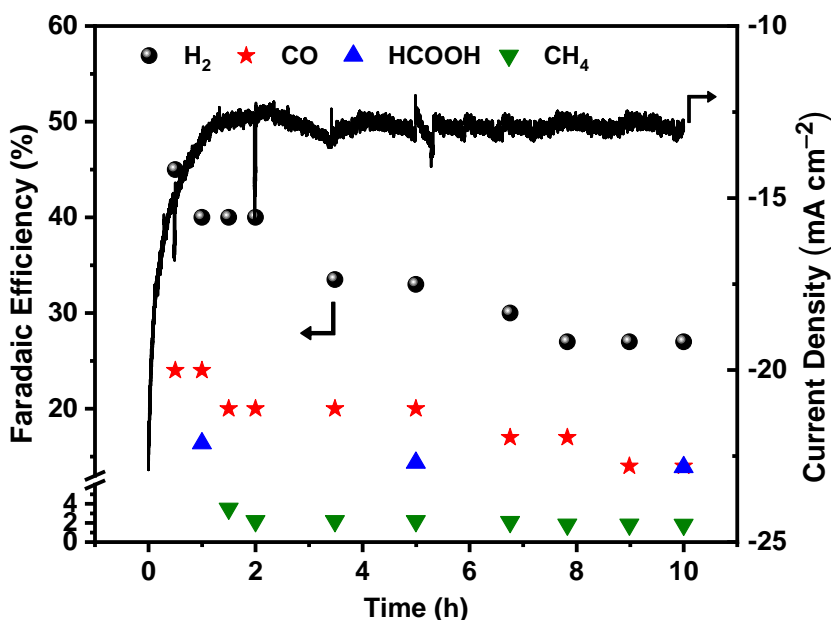


Figure 64. Stability of $\text{Au}_{50}\text{Pb}_{50}$ catalyst measured in CO_2 -saturated 0.5 M KHCO_3 at -1.07 V vs. RHE. Total current density and FE for H_2 , CO, HCOOH, and CH_4 versus time. The layer was heated in an air atmosphere at 280 °C.

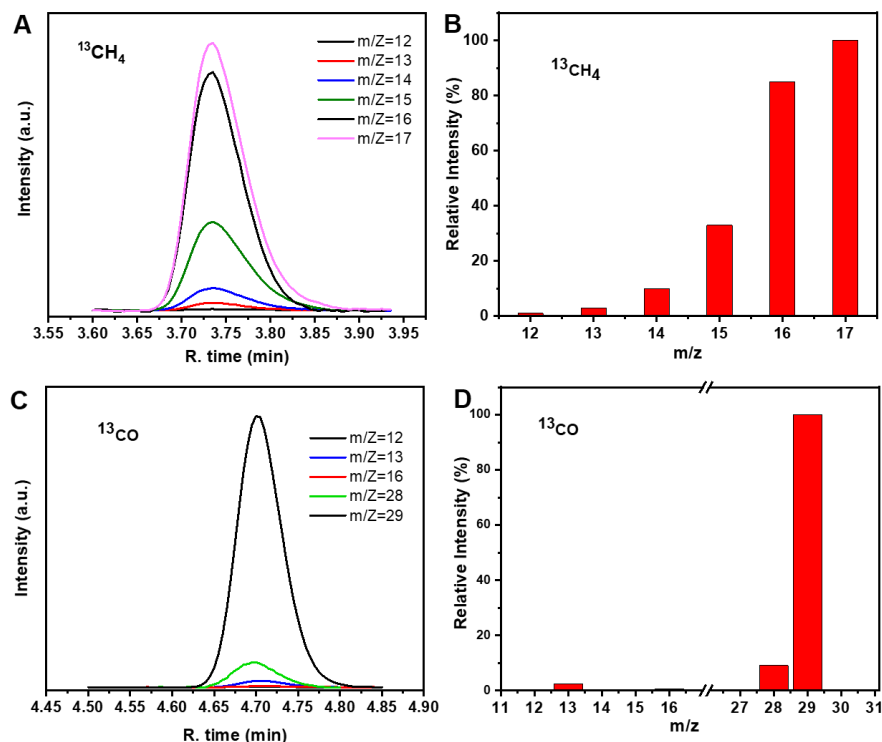


Figure 65. Isotopic labeling experiment. Mass spectra of the obtained products: (A-B) $^{13}\text{CH}_4$ and (C-D) ^{13}CO during electrolysis at -1.07 V vs. RHE on $\text{Pb}_{95}\text{Au}_5$ catalyst when both CO_2 and KHCO_3 were ^{13}C labeled.

We also performed a set of controlled experiments in which the electrodes were prepared from a physical mixture of Au and Pb NPs. A physically mixed electrode (60 at.% Au + 40 at.% Pb) with a composition similar to that of the $\text{Au}_{50}\text{Pb}_{50}$ catalyst (as confirmed by EDX analysis, **Table 7**) was prepared and investigated at -1.07 V vs. RHE (**Figure 66** and **Figure 59**). A current density of -6 mA cm^{-2} was achieved (note the -10.8 mA cm^{-2} value recorded for the respective bimetallic catalyst). The CO and CH_4 FEs significantly dropped to 2 % and < 0.5 %, respectively, whereas, the FE_{HCOOH} increased to 50 %. This suggests that the interfaces among the monometallic domains are the plausible active sites for CO_2 reduction to CH_4 . In the Au-Pb system, the monometallic domains are more adjacent through nanostructured Au/Pb interfaces, whereas the physically mixed system contains much less interfaces. We performed a CO electrolysis experiment, and CH_4 was generated with a 4.9 % FE, which is comparable to that in CO_2 reduction, and detected at an earlier time (the first 30 min). This proves that the bimetallic Au-Pb electrodes can reduce CO and suggests CO to be a key intermediate in the proposed mechanism (**Figure 67**).

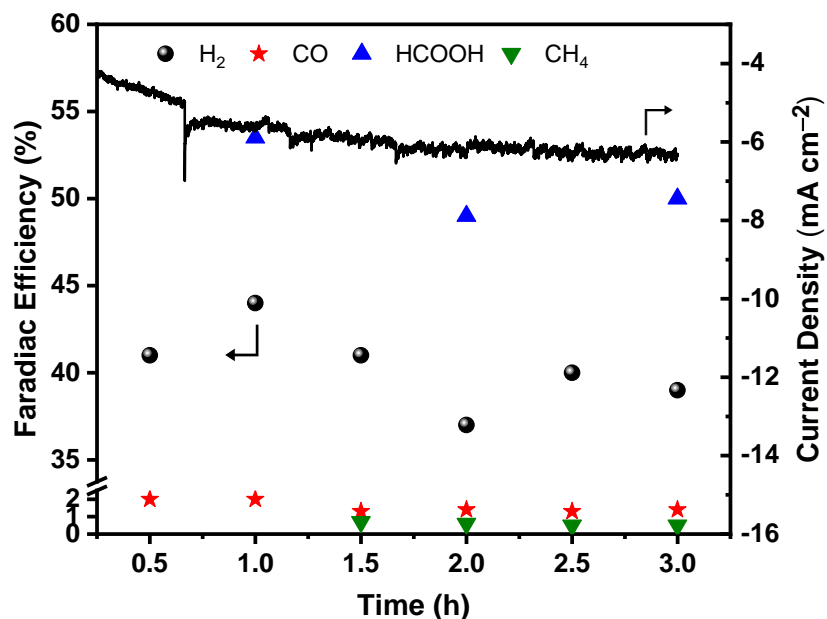


Figure 66. Electrochemical CO₂ reduction performance of the physically mixed (Au+Pb) electrode: Faradaic efficiency for H₂, CO, HCOOH, and CH₄, and total current density values measured during 3 h electrolysis at -1.07 V vs. RHE in CO₂-saturated 0.5 M KHCO₃. The layer is heated in an air atmosphere.

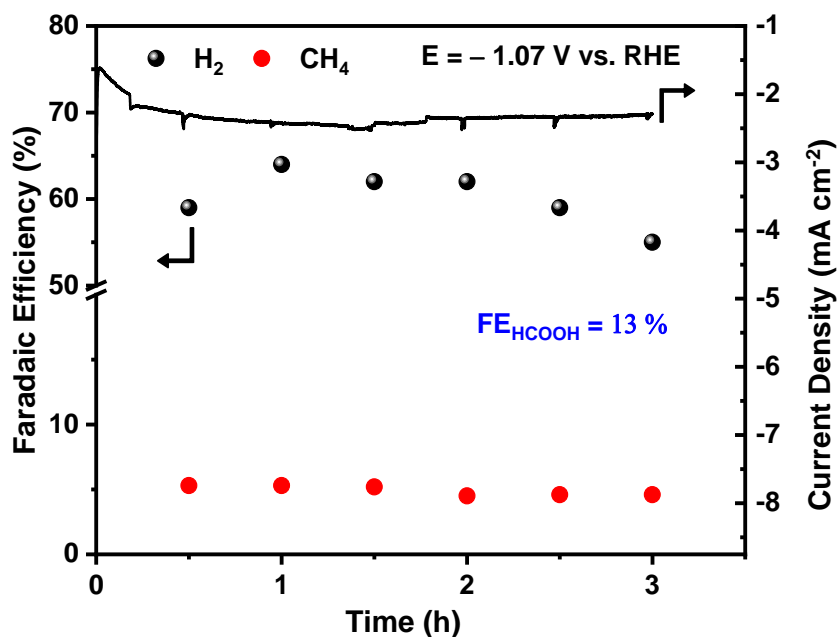


Figure 67. Faradaic efficiency for H₂, HCOOH, and CH₄ and total current density values measured during 3 h electrolysis at -1.07 V vs. RHE in CO-saturated 0.5 M KHCO₃ using Pb₉₅Au₅ catalyst. The layer is heated in an air atmosphere.

To gain further insights on the mechanism of the CO₂ reduction process, Raman spectra were collected under electrochemical control. This allows the direct monitoring of both the changes in the chemical state of the electrocatalysts and the formation of certain reaction intermediates and products during the electrolysis [120]. The spectra collected between the OCP and -0.6 V vs. RHE exhibit only bands associated to tetragonal PbO (84 and ~ 144 cm⁻¹) and orthorhombic PbO (280 cm⁻¹) [135] and the O–H stretching mode of the adsorbed water (3000 – 3700 cm⁻¹, this band was almost independent of the potential) [120]. At a moderate negative potential (-0.8 V vs. RHE), new bands appeared, and their intensities show a slight potential dependence (**Figure 68A**). The PbO bands became more intense and slightly shifted at more negative potentials because of the formation of surface defects as a result of partial reduction (**Figure 68B**) [124]. This shift indicates that the CO₂ reduction proceeds at potentials where PbO_x is present. At potentials more negative than -1.5 V vs. RHE, it was difficult to collect Raman spectra due to the intense gas evolution. The bands' assignment is presented in **Figure 68A** and summarized in **Table 8**, a band at 2950 cm⁻¹ and several bands of moderate intensity in the region of 900 – 1715 cm⁻¹ were observed. These bands are similar to those we observed during CO₂R on Au-Sn bimetallic NPs, and adsorption of HCOOH on silver colloids and Cu [125,126], indicating the formation of HCOOH and the presence of adsorbed bicarbonate species.

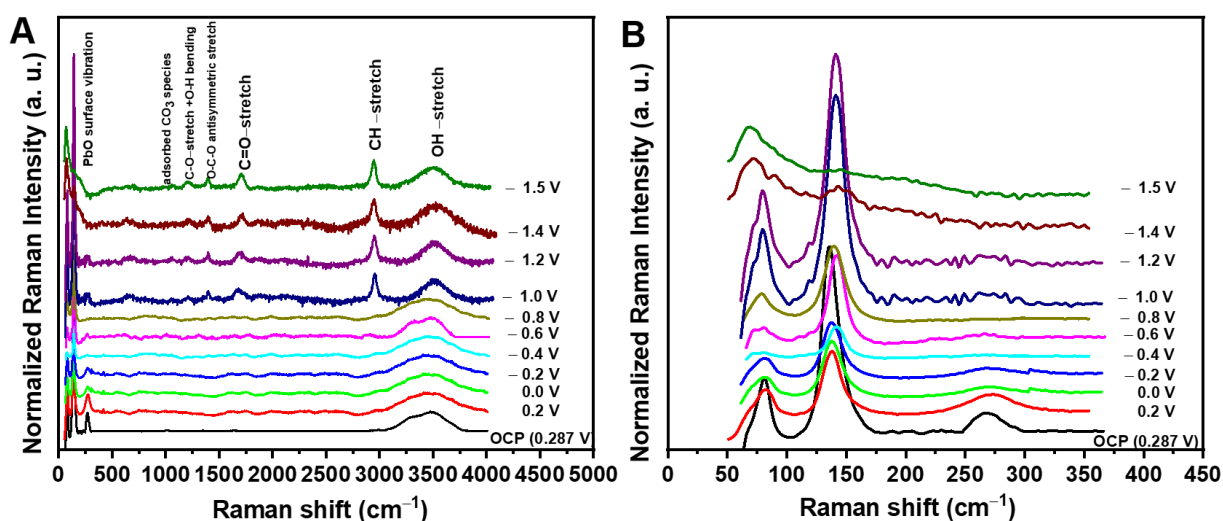


Figure 68. (A) Raman spectra collected in CO₂-saturated 0.5 M KHCO₃ as a function of the applied potential on Au₅₀Pb₅₀ catalyst, and (B) a magnified graph showing the PbO bands. The potential is versus RHE scale.

Table 8. Assignment of Raman bands observed during CO₂ electroreduction on Au₅₀Pb₅₀ catalyst in CO₂-saturated 0.5 M KHCO₃.

Frequency / cm ⁻¹	Assignment	Ref.
3000-3700	O-H stretching mode of water	[122,136]
~2930	C-H stretching mode of formate	[122,126,136]
~1770	carbonyl stretching mode of formate	[126]
~1595	O-C-O antisymmetric stretching mode of formate	[122]
~1335	O-C-O symmetric stretching mode of formate	[122]
1170-1210	C-O stretching + O-H bending mode	[126]
~925, ~1000, ~1060	adsorbed carbonate species	[125,126,136]
~84, ~144	Tetragonal PbO	[135]
~280	Orthorhombic PbO	[135]

The spectra recorded for pure Pb show the formation of PbCO₃ at the beginning of the experiment, and there is an instant and considerable decrease in the intensity of PbO band (**Figure 69**). Interestingly enough, PbO_x seems to be better stabilized on Au-Pb bimetallic surfaces than pure Pb surface. This trend was already seen on the LSV traces, where the lower onset potential was observed only for those air-heated samples where higher amounts of Au was present, ensuring stability for the PbO_x phase. Furthermore, more negative potential was required for developing the bands on Pb NPs (**Figure 70**), consistent with the observed trend of the onset potential (**Figure 55A**). The presence of strong intensity bands of the adsorbed species on the Au-Pb bimetallic surface compared to Pb NPs could be attributed to the surface enhanced Raman scattering. This is most likely due to the presence of Au NPs, where the laser wavelength is compatible with the localized surface plasmon resonance band of Au [126].

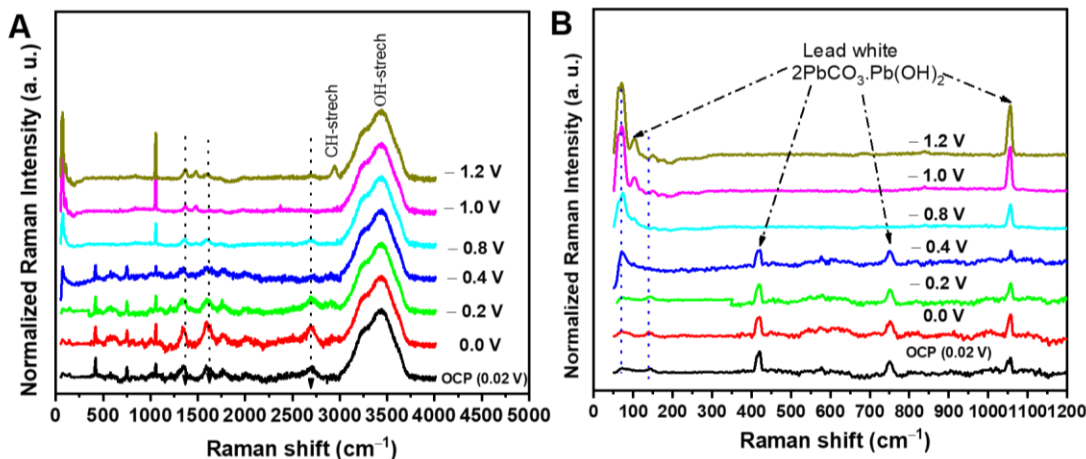


Figure 69. (A) Raman spectra collected in CO_2 -saturated 0.5 M KHCO_3 as a function of the applied potential on pure Pb, (dotted lines mark the bands from the substrate), and (B) a magnified graph of the spectra. The potential is versus RHE scale.

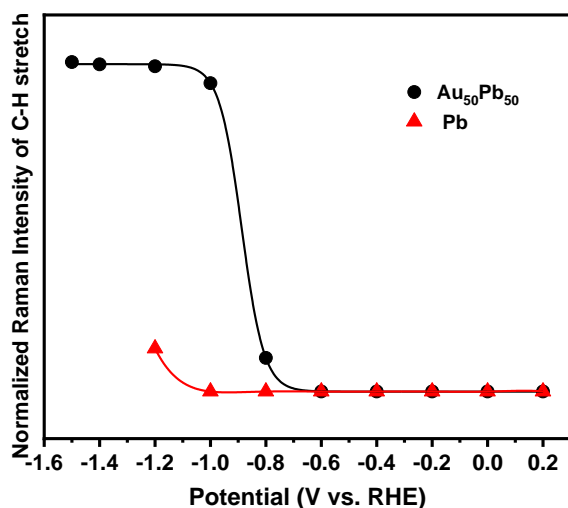


Figure 70. Potential dependence of (C–H -stretch) intensity of formate anion at 2950 cm^{-1} , on $\text{Au}_{50}\text{Pb}_{50}$ and Pb NPs, as a function of the applied potential.

5.3.3. Computational Simulations

The DFT simulations were performed to the CHE thermodynamics model to reproduce the multiple possible paths for producing CH_4 according to the literature [30,81,137]. We had a collaborative work for this theoretical study. Therefore, here, we summarized the main points that support the explanation of the obtained activity and selectivity trends. and the data of the calculated Gibbs energy and geometric structures are available in the third paper of the publication list.

1. $* + \text{CO}_2(\text{g}) + \text{H}^+ + \text{e}^- \rightarrow *\text{COOH}$
2. $*\text{COOH} + \text{H}^+ + \text{e}^- \rightarrow *\text{CO} + \text{H}_2\text{O} (\text{g})$

Alternative path for steps 1, 2

1. $* + \text{CO}_2(\text{g}) + \text{H}^+ + \text{e}^- \rightarrow *\text{HCOO}$
2. $*\text{HCOO} + \text{H}^+ + \text{e}^- \rightarrow *\text{CO} + \text{H}_2\text{O} (\text{g})$
3. $*\text{CO} + \text{H}^+ + \text{e}^- \rightarrow *\text{CHO}$
4. $*\text{CHO} + \text{H}^+ + \text{e}^- \rightarrow *\text{CHOH}$

Alternative path for steps 3, 4

3. $\text{CO} + \text{H}^+ + \text{e}^- \rightarrow *\text{COH}$
4. $*\text{COH} + \text{H}^+ + \text{e}^- \rightarrow *\text{CHOH}$
5. $*\text{CHOH} + \text{H}^+ + \text{e}^- \rightarrow *\text{CH} + \text{H}_2\text{O}(\text{g})$
6. $*\text{CH} + \text{H}^+ + \text{e}^- \rightarrow *\text{CH}_2$
7. $*\text{CH}_2 + \text{H}^+ + \text{e}^- \rightarrow *\text{CH}_3$
8. $*\text{CH}_3 + \text{H}^+ + \text{e}^- \rightarrow \text{CH}_4(\text{g}) + *$

Where * represents the active site where the fragment is bound. After surface energy evaluations the Au(111), Pb(111), PbAu₂(111) and Pb₂Au(100) surfaces were retained for reactivity evaluation as they have the lowest energy surfaces. From the simulations ran on these systems, a few general conclusions can be drawn: (1) CH₄ cannot be formed in the absence of O in the lattice, because the reaction would be blocked at the first intermediate already while forming COOH or HCOO (see the analogy with the samples heat treated in Ar). (2) Without O inside the lattice, the intermediates containing O bind too strongly to Pb and therefore the reaction cannot progress further. (3) If O is already present inside the lattice, the intermediates containing O are less bound and the reaction can evolve towards CH₄. The calculations performed without O have a positive ΔG at the first step (formation of COOH or HCCO). This would suggest that the inclusion of O is necessary, to get through this first step. (4) If the system contains O but Au is not present, the reaction cannot proceed after the third step because the O in the lattice would capture the H of CHOH preventing the formation of CH. This suggests that the role of Au is crucial to provide the right sites in the final steps from CH to form CH₄ that allow methane production.

As shown in the reaction profile (**Figure 71**), the combination of Pb, Au, and O allows the formation of CH₄ as the green path has a negative ΔG for every step and is therefore exergonic; however, this does not mean that the process has to go all the way to CH₄. The reaction can terminate early by forming HCOOH (blue path in **Figure 71**), which in fact was observed experimentally. It can be noticed that there is actually a more energetically favorable path to formate not shown in **Figure 71** that involves *HCOO instead of *COOH⁴⁹.

Furthermore, the position and orientation of the intermediates during the transition from CHOH to CH are crucial. If the intermediate CHOH is too close to the O* sites on the surface, it could easily lose an H rendering adsorbed CHO* and OH*. This would lead to an alternative CO reduction path that prevents the formation of CH₄ (red path in **Figure 71**). This destabilizing path is even more visible on the simulations with a larger cell with an Au island (**Figure 12**) as the interface between Au and Pb can present some gaps due to the lattice mismatch between Au and Pb, making it easier intermediates to be stuck there.

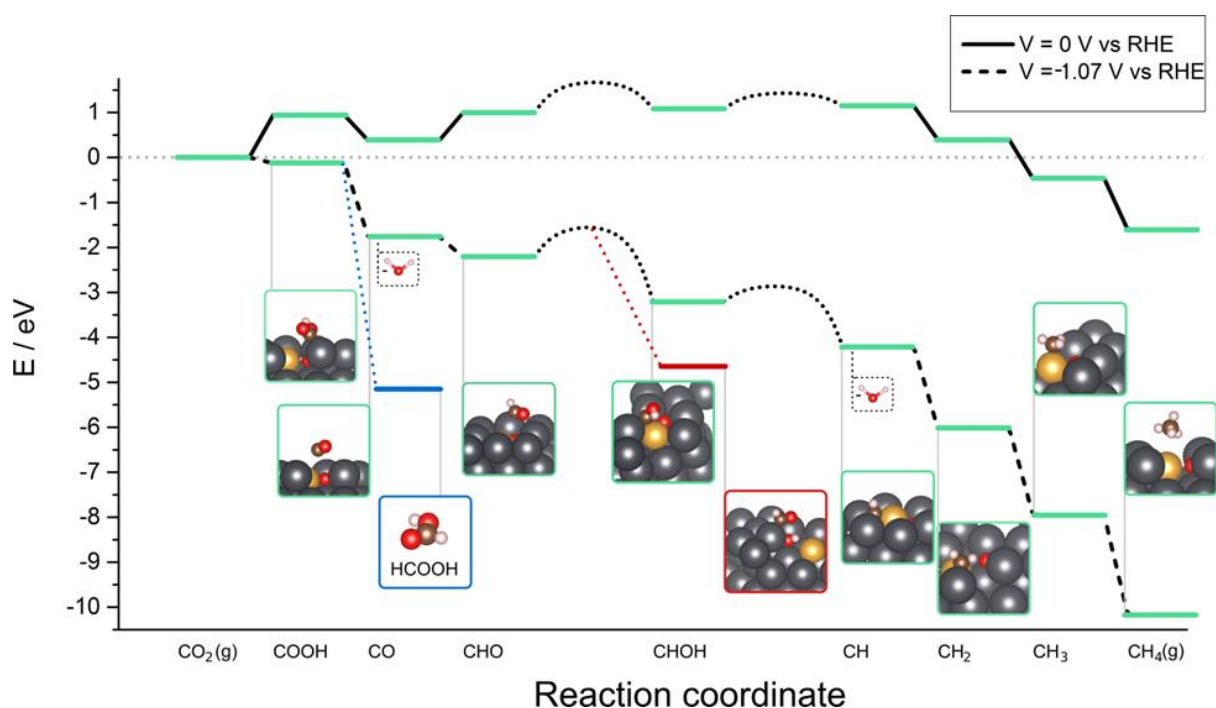


Figure 71. Energy profile on Pb-Au system with 3% Au and O impurities inside the surface. Each step involves a H⁺ and e⁻ transfer. In green is the full CH₄ path. The reaction can be stopped early in the HCOOH path in blue. The transition from CHOH to CH can be stopped if the intermediate CHOH is too close to the O site in the lattice (partial oxide phase) in the red path that could lead to CO reduction.

In summary, the Pb (111) with O in the lattice and Au in the surrounding appearing at the interface between the Pb and Au domains can form CH₄, H₂, CO, HCOOH as observed experimentally. This synergetic site allows simultaneously the first steps as the oxygen in the lattice (partial oxide) limits the formation of HCOOH, while at the end of the cycle the low adsorption of the Au sites enhances CH₄ formation/desorption. Therefore, fine-tuning of the binding energies is needed. In our case, this was obtained by reducing the energy of oxygenated intermediates to Pb (due to the oxygen poisoning) and providing enough desorption sites in the form of Au containing sites. Meeting all these conditions is only possible at the interface and therefore would explain the low amount of CH₄ produced.

6. Conclusions

The synthesis of Au-based bimetallic NPs with different compositions and uniform morphology was the first step to provide a systematic study on their electrocatalytic activity toward CO₂RR, which is the objective of my doctoral work. We decided to explore the combination of Au with Sn, Pb, and Ag, as three bimetallic systems which have not been employed in CO₂R yet. Due to the difference in the reduction potentials, the simultaneous reduction of Au ions and the precursor of the p-block metals (Sn or Pb), resulted in the formation of individual particles of both metals. Therefore, a two-step synthesis approach was developed and employed to combine Au with p-block elements (Sn and Pb). Au-Sn bimetallic NPs with different intermetallic phase compositions were synthesized via the gradual diffusion of Sn into the premade Au NPs, acting as seeds. This system revealed the advantage of the intermetallic phase compared to the monometallic counterparts for both the activity and product distribution. Whereas, Au-Pb catalysts consisting of Au NPs deposited on the top of Pb NPs with a native Pb oxide (PbO_x) were synthesized with different Au/Pb interfaces. We started with the formation of metallic Pb NPs, which act as nucleation seeds, followed by a controlled galvanic replacement of Pb with Au. These structural moieties worked synergistically to tune both activity and selectivity. A series of Au-Ag nanoalloys was synthesized with uniform morphology and tunable electronic properties (work function), as well as Ag@Au core-shell NPs were prepared with similar composition. This system highlighted the importance of both electronic and geometric effects for CO₂R performance and product distribution.

The most important results of my doctoral work can be summarized in the following points:

- We provided a strategy to synthesize Au-Sn electrocatalysts with a bimetallic core and an ultra-thin partially oxidized SnO_x shell. This two-step approach was demonstrated by a series of spherical-shaped Au-Sn nanoparticles with a narrow size distribution and tunable composition (i.e., Au₂Sn₁, Au₁Sn₁, Au₁Sn₂, and Au₁Sn₄) were successfully synthesized by the chemical reduction of different amounts of Sn precursor in the presence of the premade Au seeds at ambient conditions. The size of the particles was 23±2.9, 31.8±3.9, 32.4±3.7, and 33±2.5 nm, in the series of samples with increasing Sn content. The AuSn intermetallic phase became more prevalent with increasing Sn⁴⁺ concentration, achieving 100% at the Au₁Sn₂ sample. AuSn₂ intermetallic phase was observed at the highest Sn

content (sample Au₁Sn₄). The amount of the partially oxidized tin species (SnO_x) at the surface increased gradually with the total Sn concentration, and there was no sign of oxidized Au.

- The phase composition influences the electrocatalytic activity of Au-Sn NPs in CO₂R. While two high-value products (HCOOH and syngas) were formed in all cases, their ratio was dependent on the composition. The bimetallic samples outperformed both gold and tin and showed a good product distribution. The Au₁Sn₂ catalyst (containing almost pure AuSn phase) showed the lowest overpotential for CO₂R, 400 mV less negative compared to pure Sn. At -1.0 V vs. RHE, a current of 8 mA cm⁻² was achieved and remained stable for 10 h.
- Selective isotopic labeling experiments were performed under nonequilibrium condition, proved that CO₂ molecules supplied through fast equilibrium with the bicarbonate, rather than CO₂ in the bulk solution, are the primary source of the produced CO and HCOOH. In situ Raman spectroelectrochemistry confirmed the presence of bicarbonate anions on the electrode surface and the stability of SnO_x under the reaction conditions and proved the generation of formate anions at a notably less negative potential on the AuSn phase (-0.59 V vs. RHE) compared to the pure Sn electrode (-0.92 V vs. RHE).
- Au-decorated Pb NPs were synthesized with uniform morphology and various compositions (i.e., Au₅Pb₉₅, Au₂₀Pb₈₀, Au₅₀Pb₅₀). The first step is the formation of metallic Pb NPs, followed by the galvanic displacement of Pb with Au. This process allowed to tune the composition and thus the relative amount of Au/Pb interfaces. An inverse structure, Au-core -Pb-shell (Pb₉₅Au₅) NPs were also prepared with a similar composition to the most Pb-rich sample (Au₅Pb₉₅).
- Au-Pb bimetallic catalysts with different Au/Pb interfaces work synergistically to transform CO₂ to a > 2e⁻ reduction product (CH₄). The stability of PbO_x under the reduction condition was high on the bimetallic catalyst (unlike for bare Pb) which seems to be necessary for CH₄ formation. DFT calculations confirmed that the Au/Pb bimetallic interface, together with the subsurface oxygen possess a moderate binding strength for the key intermediates, which is indeed necessary for the CH₄ pathway. Experimental results indicated that comparable amounts of Au and Pb are needed at the surface to ensure high reaction rates.

- A series of monodisperse Au-Ag nanoalloys were prepared in the 25-30 nm range, with different compositions and uniform morphology. Tunable plasmonic properties were demonstrated, where the localized surface plasmon resonance band red-shifted in a linear fashion with increasing the Au content. Ag@Au core-shell NPs were successfully prepared with similar size and composition for comparative studies.
- The electronic properties of Au-Ag alloy electrocatalysts were tuned with the composition, while keeping other structural parameters fixed. The Fermi level shifts downwards linearly between 4.68 eV and 4.49 eV with the Au content, which was consistent with the observed trend of electrocatalytic properties (j_{CO} increases with Au content).
- The CO₂R activity of Ag@Au core-shell NPs was compared to that of nanoalloy (similar bulk composition) and pure Ag (similar electronic structure). Substantial differences were revealed in both comparisons, both the selectivity and the activity. These trends indicated that neither electronic nor geometric effect *alone* can determine the electrocatalytic properties.

References

- [1] N.S. Lewis, D.G. Nocera, Powering the planet: Chemical challenges in solar energy utilization, *PProc. Natl. Acad. Sci. U. S. A.* 103 (2006) 15729–15735. doi:10.1073/pnas.0603395103.
- [2] R. Song, W. Zhu, J. Fu, Y. Chen, L. Liu, J. Zhang, Y. Lin, J. Zhu, Electrode materials engineering in electrocatalytic CO₂ reduction: energy input and conversion efficiency, *Adv. Mater.* (2019) 1903796. doi:10.1002/adma.201903796.
- [3] J.A. Turner, A realizable renewable energy future, *Science*. 285 (1999) 687–689. doi:10.1126/science.285.5428.687.
- [4] D.T. Whipple, P.J.A. Kenis, Prospects of CO₂ utilization via direct heterogeneous electrochemical reduction, *J. Phys. Chem. Lett.* 1 (2010) 3451–3458. doi:10.1021/jz1012627.
- [5] B. Kumar, J.P. Brian, V. Atla, S. Kumari, K.A. Bertram, R.T. White, J.M. Spurgeon, New trends in the development of heterogeneous catalysts for electrochemical CO₂ reduction, *Catal. Today*. 270 (2016) 19–30. doi:10.1016/j.cattod.2016.02.006.
- [6] D. Ren, J. Gao, S.M. Zakeeruddin, M. Grätzel, Bimetallic electrocatalysts for carbon dioxide reduction, *CHIMIA* 73 (2019.) 928–935. doi:10.2533/chimia.2019.928.
- [7] W. Zhu, B.M. Tackett, J.G. Chen, F. Jiao, Bimetallic electrocatalysts for CO₂ reduction, *Top. Curr. Chem.* 376 (2018) 1–21. doi:10.1007/s41061-018-0220-5.
- [8] H. Bin Yang, S.F. Hung, S. Liu, K. Yuan, S. Miao, L. Zhang, X. Huang, H.Y. Wang, W. Cai, R. Chen, J. Gao, X. Yang, W. Chen, Y. Huang, H.M. Chen, C.M. Li, T. Zhang, B. Liu, Atomically dispersed Ni(i) as the active site for electrochemical CO₂ reduction, *Nat. Energy*. 3 (2018) 140–147. doi:10.1038/s41560-017-0078-8.
- [9] C. Graves, S.D. Ebbesen, M. Mogensen, K.S. Lackner, Sustainable hydrocarbon fuels by recycling CO₂ and H₂O with renewable or nuclear energy, *Renew. Sustain. Energy Rev.* 15 (2011) 1–23. doi:10.1016/j.rser.2010.07.014.
- [10] S. Chu, Y. Cui, N. Liu, The path towards sustainable energy, *Nat. Mater.* 16 (2017) 16–22. doi:10.1038/nmat4834.
- [11] S.J. Davis, N.S. Lewis, M. Shaner, S. Aggarwal, D. Arent, I.L. Azevedo, S.M. Benson, T. Bradley, J. Brouwer, Y.M. Chiang, C.T.M. Clack, A. Cohen, S. Doig, J. Edmonds, P. Fennell, C.B. Field, B. Hannegan, B.M. Hodge, M.I. Hoffert, E. Ingersoll, P. Jaramillo, K.S. Lackner, K.J. Mach, M. Mastrandrea, J. Ogden, P.F. Peterson, D.L. Sanchez, D. Sperling, J. Stagner, J.E. Trancik, C.J. Yang, K. Caldeira, Net-zero emissions energy systems, *Science* . 360 (2018). doi:10.1126/science.aas9793.
- [12] Z. Yang, J. Zhang, M.C.W. Kintner-Meyer, X. Lu, D. Choi, J.P. Lemmon, J. Liu, Electrochemical energy storage for green grid, *Chem. Rev.* 111 (2011) 3577–3613. doi:10.1021/cr100290v.
- [13] B. Pinnangudi, M. Kuykendal, S. Bhadra, Smart grid energy storage, in: *Power Grid Smart, Secur. Green Reliab.*, Academic Press, 2017: pp. 93–135. doi:10.1016/B978-0-12-805321-8.00004-5.
- [14] T. Searchinger, R. Heimlich, R.A. Houghton, F. Dong, A. Elobeid, J. Fabiosa, S. Tokgoz, D. Hayes, T. Yu, Use of U.S. croplands for biofuels increases greenhouse gases through emissions from land-use change, *Science* . 319 (2008) 1238–1240.
- [15] E.S. Rubin, J.E. Davison, H.J. Herzog, The cost of CO₂ capture and storage, *Int. J. Greenh. Gas Control*. 40 (2015) 378–400. doi:10.1016/j.ijggc.2015.05.018.
- [16] E. V. Kondratenko, G. Mul, J. Baltrusaitis, G.O. Larrazábal, J. Pérez-Ramírez, Status and perspectives of CO₂ conversion into fuels and chemicals by catalytic, photocatalytic and electrocatalytic processes, *Energy Environ. Sci.* 6 (2013) 3112–3135. doi:10.1039/c3ee41272e.

- [17] Y. Oh, X. Hu, Organic molecules as mediators and catalysts for photocatalytic and electrocatalytic CO₂ reduction, *Chem. Soc. Rev.* 42 (2013) 2253–2261. doi:10.1039/c2cs35276a.
- [18] S. Bai, J. Jiang, Q. Zhang, Y. Xiong, Steering charge kinetics in photocatalysis: intersection of materials syntheses, characterization techniques and theoretical simulations, *Chem. Soc. Rev.* 44 (2015) 2893–2939. doi:10.1039/C5CS00064E.
- [19] G. Centi, E.A. Quadrelli, S. Perathoner, Catalysis for CO₂ conversion: a key technology for rapid introduction of renewable energy in the value chain of chemical industries, *Energy Environ. Sci.* 6 (2013) 1711. doi:10.1039/c3ee00056g.
- [20] J. Shi, Y. Jiang, Z. Jiang, X. Wang, X. Wang, S. Zhang, P. Han, C. Yang, Enzymatic conversion of carbon dioxide, *Chem. Soc. Rev.* 44 (2015) 5981–6000. doi:10.1039/C5CS00182J.
- [21] S. Nitopi, E. Bertheussen, S.B. Scott, X. Liu, A.K. Engstfeld, S. Horch, B. Seger, I.E.L. Stephens, K. Chan, C. Hahn, J.K. Nørskov, T.F. Jaramillo, I. Chorkendorff, Progress and perspectives of electrochemical CO₂ reduction on copper in aqueous electrolyte, *Chem. Rev.* 119 (2019) 7610–7672. doi:10.1021/acs.chemrev.8b00705.
- [22] M. Carmo, D.L. Fritz, J. Mergel, D. Stolten, A comprehensive review on PEM water electrolysis, *Int. J. Hydrogen Energy.* 38 (2013) 4901–4934. doi:10.1016/j.ijhydene.2013.01.151.
- [23] Z.W. Seh, J. Kibsgaard, C.F. Dickens, I. Chorkendorff, J.K. Nørskov, T.F. Jaramillo, Combining theory and experiment in electrocatalysis: insights into materials design, *Science* . 355 (2017) eaad4998. doi:10.1126/science.aad4998.
- [24] B. Endrődi, G. Bencsik, F. Darvas, R. Jones, K. Rajeshwar, C. Janáky, Continuous-flow electroreduction of carbon dioxide, *Prog. Energy Combust. Sci.* 62 (2017) 133–154. doi:10.1016/j.peecs.2017.05.005.
- [25] Y. Hori, K. Kikuchi, S. Suzuki, Production of CO and CH₄ in electrochemical reduction of CO₂ at Metal Electrodes in aqueous hydrogencarbonate solutions, *Chem. Lett.* 14 (1985) 1695–1698. doi:10.1246/cl.1985.1695.
- [26] Y. Hori, Electrochemical CO₂ reduction on metal electrodes, in: C. Vayenas, R. White, M. Gamboa-Aldeco (Eds.), *Mod. Asp. Electrochem.*, Springer, New York, NY, 2008: pp. 89–189. doi:10.1007/978-0-387-49489-0_3.
- [27] A. Bagger, W. Ju, A.S. Varela, P. Strasser, J. Rossmeisl, Electrochemical CO₂ reduction: a classification problem, *ChemPhysChem.* 18 (2017) 3266–3273. doi:10.1002/cphc.201700736.
- [28] J.T. Feaster, C. Shi, E.R. Cave, T. Hatsukade, D.N. Abram, K.P. Kuhl, C. Hahn, J.K. Nørskov, T.F. Jaramillo, Understanding selectivity for the electrochemical reduction of carbon dioxide to formic acid and carbon monoxide on metal electrodes, *ACS Catal.* 7 (2017) 4822–4827. doi:10.1021/acscatal.7b00687.
- [29] A.A. Peterson, F. Abild-Pedersen, F. Studt, J. Rossmeisl, J.K. Nørskov, How copper catalyzes the electroreduction of carbon dioxide into hydrocarbon fuels, *Energy Environ. Sci.* 3 (2010) 1311–1315. doi:10.1039/c0ee00071j.
- [30] K.P. Kuhl, T. Hatsukade, E.R. Cave, D.N. Abram, J. Kibsgaard, T.F. Jaramillo, Electrocatalytic conversion of carbon dioxide to methane and methanol on transition metal surfaces, *J. Am. Chem. Soc.* 136 (2014) 14107–14113. doi:10.1021/ja505791r.
- [31] D. Gao, H. Zhou, J.J. Wang, S. Miao, F. Yang, G. Wang, J.J. Wang, X. Bao, Size-dependent electrocatalytic reduction of CO₂ over Pd nanoparticles, *J. Am. Chem. Soc.* 137 (2015) 4288–4291. doi:10.1021/jacs.5b00046.
- [32] A. Salehi-Khojin, H.R.M. Jhong, B.A. Rosen, W. Zhu, S. Ma, P.J.A. Kenis, R.I. Masel, Nanoparticle silver catalysts that show enhanced activity for carbon dioxide electrolysis, *J. Phys. Chem. C.* 117 (2013) 1627–1632. doi:10.1021/jp310509z.
- [33] W. Zhu, R. Michalsky, Ö. Metin, H. Lv, S. Guo, C.J. Wright, X. Sun, A.A. Peterson, S. Sun, Monodisperse

- Au nanoparticles for selective electrocatalytic reduction of CO₂ to CO, *J. Am. Chem. Soc.* 135 (2013) 16833–16836. doi:10.1021/ja409445p.
- [34] R. Reske, H. Mistry, F. Behafarid, B. Roldan Cuenya, P. Strasser, Particle size effects in the catalytic electroreduction of CO₂ on Cu nanoparticles, *J. Am. Chem. Soc.* 136 (2014) 6978–6986. doi:10.1021/ja500328k.
- [35] H. Mistry, R. Reske, Z. Zeng, Z.J. Zhao, J. Greeley, P. Strasser, B.R. Cuenya, Exceptional size-dependent activity enhancement in the electroreduction of CO₂ over Au nanoparticles, *J. Am. Chem. Soc.* 136 (2014) 16473–16476. doi:10.1021/ja508879j.
- [36] Y.C. Hsieh, S.D. Senanayake, Y. Zhang, W. Xu, D.E. Polyansky, Effect of chloride anions on the synthesis and enhanced catalytic activity of silver nanocoral electrodes for CO₂ electroreduction, *ACS Catal.* 5 (2015) 5349–5356. doi:10.1021/acscatal.5b01235.
- [37] Q. Lu, J. Rosen, Y. Zhou, G.S. Hutchings, Y.C. Kimmel, J.G. Chen, F. Jiao, A selective and efficient electrocatalyst for carbon dioxide reduction, *Nat. Commun.* 5 (2014) 1–6. doi:10.1038/ncomms4242.
- [38] A. Dutta, C.E. Morstein, M. Rahaman, A. Cedeno López, P. Broekmann, Beyond copper in CO₂ electrolysis: effective hydrocarbon production on silver-nanofoam catalysts, *ACS Catal.* 8 (2018) 8357–8368. doi:10.1021/acscatal.8b01738.
- [39] Z. Wang, G. Yang, Z. Zhang, M. Jin, Y. Yin, Selectivity on etching: creation of high-energy facets on copper nanocrystals for CO₂ electrochemical reduction, *ACS Nano.* 10 (2016) 4559–4564. doi:10.1021/acsnano.6b00602.
- [40] G. Wang, J. Liu, Y. Sui, M. Wang, L. Qiao, F. Du, B. Zou, Palladium structure engineering induced by electrochemical H intercalation boosts hydrogen evolution catalysis, *J. Mater. Chem. A.* 7 (2019) 14876–14881. doi:10.1039/c9ta03971f.
- [41] W. Zhu, Y.J. Zhang, H. Zhang, H. Lv, Q. Li, R. Michalsky, A.A. Peterson, S. Sun, Active and selective conversion of CO₂ to CO on ultrathin Au nanowires, *J. Am. Chem. Soc.* 136 (2014) 16132–16135. doi:10.1021/ja5095099.
- [42] W. Zhu, L. Zhang, P. Yang, C. Hu, Z. Luo, X. Chang, Z.J. Zhao, J. Gong, Low-coordinated edge sites on ultrathin palladium nanosheets boost carbon dioxide electroreduction performance, *Angew. Chemie - Int. Ed.* 57 (2018) 11544–11548. doi:10.1002/anie.201806432.
- [43] N. Han, Y. Wang, H. Yang, J. Deng, J. Wu, Y. Li, Y. Li, Ultrathin bismuth nanosheets from in situ topotactic transformation for selective electrocatalytic CO₂ reduction to formate, *Nat. Commun.* 9 (2018) 1–8. doi:10.1038/s41467-018-03712-z.
- [44] Y. Chen, C.W. Li, M.W. Kanan, Aqueous CO₂ reduction at very low overpotential on oxide-derived Au nanoparticles, *J. Am. Chem. Soc.* 134 (2012) 19969–19972. doi:10.1021/ja309317u.
- [45] C.H. Lee, M.W. Kanan, Controlling H⁺ vs CO₂ reduction selectivity on Pb electrodes, *ACS Catal.* 5 (2015) 465–469. doi:10.1021/cs5017672.
- [46] C.W. Li, M.W. Kanan, CO₂ reduction at low overpotential on Cu electrodes resulting from the reduction of thick Cu₂O films, *J. Am. Chem. Soc.* 134 (2012) 7231–7234. doi:10.1021/ja3010978.
- [47] D. Raciti, K.J. Livi, C. Wang, Highly dense Cu nanowires for low-overpotential CO₂ reduction, *Nano Lett.* 15 (2015) 6829–6835. doi:10.1021/acs.nanolett.5b03298.
- [48] T. Zhang, H. Zhong, Y. Qiu, X. Li, H. Zhang, Zn electrode with a layer of nanoparticles for selective electroreduction of CO₂ to formate in aqueous solutions, *J. Mater. Chem. A.* 4 (2016) 16670–16676. doi:10.1039/c6ta07000k.
- [49] A. Dutta, M. Rahaman, M. Mohos, A. Zanetti, P. Broekmann, Electrochemical CO₂ conversion using skeleton (sponge) type of Cu catalysts, *ACS Catal.* 7 (2017) 5431–5437. doi:10.1021/acscatal.7b01548.

- [50] E.R. Cave, J.H. Montoya, K.P. Kuhl, D.N. Abram, T. Hatsukade, C. Shi, C. Hahn, J.K. Nørskov, T.F. Jaramillo, Electrochemical CO₂ reduction on Au surfaces: mechanistic aspects regarding the formation of major and minor products, *Phys. Chem. Chem. Phys.* 19 (2017) 15856–15863. doi:10.1039/C7CP02855E.
- [51] M. Valenti, N.P. Prasad, R. Kas, D. Bohra, M. Ma, V. Balasubramanian, L. Chu, S. Gimenez, J. Bisquert, B. Dam, W.A. Smith, Suppressing H₂ evolution and promoting selective CO₂ electroreduction to CO at Low overpotentials by alloying Au with Pd, *ACS Catal.* (2019) 3527–3536. doi:10.1021/acscatal.8b04604.
- [52] D. Kim, J. Resasco, Y. Yu, A.M. Asiri, P. Yang, Synergistic geometric and electronic effects for electrochemical reduction of carbon dioxide using gold-copper bimetallic nanoparticles, *Nat. Commun.* 5 (2014) 1–8. doi:10.1038/ncomms5948.
- [53] J. He, N.J.J. Johnson, A. Huang, C.P. Berlinguette, Electrocatalytic alloys for CO₂ reduction, *ChemSusChem*. 11 (2018) 48–57. doi:10.1002/cssc.201701825.
- [54] J. Pérez-Ramírez, N. López, Strategies to break linear scaling relationships, *Nat. Catal.* 2 (2019) 971–976. doi:10.1038/s41929-019-0376-6.
- [55] M. Watanabe, M. Shibata, A. Kato, M. Azuma, T. Sakata, Design of alloy electrocatalysts for CO₂ Reduction: III . the Selective and reversible reduction of CO₂ on Cu Alloy Electrodes, *J. Electrochem. Soc.* . 138 (1991) 3382–3389. doi:10.1149/1.2085417.
- [56] J. Monzó, Y. Malewski, R. Kortlever, F.J. Vidal-Iglesias, J. Solla-Gullón, M.T.M. Koper, P. Rodriguez, Enhanced electrocatalytic activity of Au@Cu core@shell nanoparticles towards CO₂ reduction, *J. Mater. Chem. A*. 3 (2015) 23690–23698. doi:10.1039/c5ta06804e.
- [57] W. Zhu, L. Zhang, P. Yang, C. Hu, H. Dong, Z.J. Zhao, R. Mu, J. Gong, Formation of enriched vacancies for enhanced CO₂ electrocatalytic reduction over AuCu alloys, *ACS Energy Lett.* 3 (2018) 2144–2149. doi:10.1021/acsenerylett.8b01286.
- [58] F. Jia, X. Yu, L. Zhang, Enhanced selectivity for the electrochemical reduction of CO₂ to alcohols in aqueous solution with nanostructured Cu-Au alloy as catalyst, *J. Power Sources*. 252 (2014) 85–89. doi:10.1016/j.jpowsour.2013.12.002.
- [59] S. Back, J.H. Kim, Y.T. Kim, Y. Jung, Bifunctional interface of Au and Cu for improved CO₂ electroreduction, *ACS Appl. Mater. Interfaces*. 8 (2016) 23022–23027. doi:10.1021/acsmi.6b05903.
- [60] J. Gao, D. Ren, X. Guo, S.M. Zakeeruddin, M. Grätzel, Sequential catalysis enables enhanced C-C coupling towards multi-carbon alkenes and alcohols in carbon dioxide reduction: A study on bifunctional Cu/Au electrocatalysts, *Faraday Discuss.* 215 (2019) 282–296. doi:10.1039/c8fd00219c.
- [61] C.G. Morales-Guio, E.R. Cave, S.A. Nitopi, J.T. Feaster, L. Wang, K.P. Kuhl, A. Jackson, N.C. Johnson, D.N. Abram, T. Hatsukade, C. Hahn, T.F. Jaramillo, Improved CO₂ reduction activity towards C₂₊ alcohols on a tandem gold on copper electrocatalyst, *Nat. Catal.* 1 (2018) 764–771. doi:10.1038/s41929-018-0139-9.
- [62] S. Shen, X. Peng, L. Song, Y. Qiu, C. Li, L. Zhuo, J. He, J. Ren, X. Liu, J. Luo, AuCu alloy nanoparticle embedded Cu submicrocone arrays for selective conversion of CO₂ to ethanol, *Small*. 15 (2019) 1–7. doi:10.1002/sml.201902229.
- [63] D. Kim, C. Xie, N. Becknell, Y. Yu, M. Karamad, K. Chan, E.J. Crumlin, J.K. Nørskov, P. Yang, Electrochemical activation of CO₂ through atomic ordering transformations of AuCu nanoparticles, *J. Am. Chem. Soc.* 139 (2017) 8329–8336. doi:10.1021/jacs.7b03516.
- [64] K. Chen, X. Zhang, T. Williams, L. Bourgeois, D.R. MacFarlane, Electrochemical reduction of CO₂ on core-shell Cu/Au nanostructure arrays for syngas production, *Electrochim. Acta*. 239 (2017) 84–89. doi:10.1016/j.electacta.2017.04.019.
- [65] D. Kim, S. Lee, J.D. Ocon, B. Jeong, J.K. Lee, J. Lee, Insights into an autonomously formed oxygen-evacuated Cu₂O electrode for the selective production of C₂H₄ from CO₂, *Phys. Chem. Chem. Phys.* 17 (2015) 824–830. doi:10.1039/c4cp03172e.

- [66] R. Kas, R. Kortlever, A. Milbrat, M.T.M. Koper, G. Mul, J. Baltrusaitis, Electrochemical CO₂ reduction on Cu₂O-derived copper nanoparticles: controlling the catalytic selectivity of hydrocarbons, *Phys. Chem. Chem. Phys.* 16 (2014) 12194–12201. doi:10.1039/c4cp01520g.
- [67] J.K. Nørskov, J. Rossmeisl, A. Logadottir, L. Lindqvist, J.R. Kitchin, T. Bligaard, H. Jónsson, Origin of the overpotential for oxygen reduction at a fuel-cell cathode, *J. Phys. Chem. B.* 108 (2004) 17886–17892. doi:10.1021/jp047349j.
- [68] F. Gao, D.W. Goodman, Pd-Au bimetallic catalysts: understanding alloy effects from planar models and (supported) nanoparticles, *Chem. Soc. Rev.* 41 (2012) 8009–8020. doi:10.1039/c2cs35160a.
- [69] R. Ferrando, J. Jellinek, R.L. Johnston, Nanoalloys: From theory to applications of alloy clusters and nanoparticles, *Chem. Rev.* 108 (2008) 845–910. doi:10.1021/cr040090g.
- [70] C. Hahn, D.N. Abram, H.A. Hansen, T. Hatsukade, A. Jackson, N.C. Johnson, T.R. Hellstern, K.P. Kuhl, E.R. Cave, J.T. Feaster, T.F. Jaramillo, Synthesis of thin film AuPd alloys and their investigation for electrocatalytic CO₂ reduction, *J. Mater. Chem. A.* 3 (2015) 20185–20194. doi:10.1039/c5ta04863j.
- [71] R. Kortlever, I. Peters, C. Balemans, R. Kas, Y. Kwon, G. Mul, M.T.M. Koper, Palladium–gold catalyst for the electrochemical reduction of CO₂ to C₁–C₅ hydrocarbons, *Chem. Commun.* 52 (2016) 10229–10232. doi:10.1039/C6CC03717H.
- [72] J.J.L. Humphrey, D. Plana, V. Celorrio, S. Sadasivan, R.P. Tooze, P. Rodríguez, D.J. Fermín, Electrochemical reduction of carbon dioxide at gold-palladium core-shell nanoparticles: product distribution versus shell thickness, *ChemCatChem.* 8 (2016) 952–960. doi:10.1002/cctc.201501260.
- [73] S. Zhu, X. Qin, Q. Wang, T. Li, R. Tao, M. Gu, M. Shao, Composition-dependent CO₂ electrochemical reduction activity and selectivity on Au-Pd core-shell nanoparticles, *J. Mater. Chem. A.* 7 (2019) 16954–16961. doi:10.1039/c9ta05325e.
- [74] M. Ma, H.A. Hansen, M. Valenti, Z. Wang, A. Cao, M. Dong, W.A. Smith, Electrochemical reduction of CO₂ on compositionally variant Au-Pt bimetallic thin films, *Nano Energy.* 42 (2017) 51–57. doi:10.1016/j.nanoen.2017.09.043.
- [75] S. Kamimura, S. Yamashita, S. Abe, T. Tsubota, T. Ohno, Effect of core@shell (Au@Ag) nanostructure on surface plasmon-induced photocatalytic activity under visible light irradiation, *Appl. Catal. B Environ.* 211 (2017) 11–17. doi:10.1016/j.apcatb.2017.04.028.
- [76] J.H. Liu, A.Q. Wang, Y.S. Chi, H.P. Lin, C.Y. Mou, Synergistic effect in an Au-Ag alloy nanocatalyst: CO oxidation, *J. Phys. Chem. B.* 109 (2005) 40–43. doi:10.1021/jp044938g.
- [77] N.S.K. Gowthaman, B. Sinduja, S.A. John, Tuning the composition of gold-silver bimetallic nanoparticles for the electrochemical reduction of hydrogen peroxide and nitrobenzene, *RSC Adv.* 6 (2016) 63433–63444. doi:10.1039/c6ra05658j.
- [78] G. Zhang, Y. Kuang, J. Liu, Y. Cui, J. Chen, H. Zhou, Fabrication of Ag/Au bimetallic nanoparticles by UPD-redox replacement: application in the electrochemical reduction of benzyl chloride, *Electrochem. Commun.* 12 (2010) 1233–1236. doi:10.1016/j.elecom.2010.06.027.
- [79] M. Tahir, B. Tahir, N.A.S. Amin, Synergistic effect in plasmonic Au/Ag alloy NPs co-coated TiO₂ NWs toward visible-light enhanced CO₂ photoreduction to fuels, *Appl. Catal. B Environ.* 204 (2017) 548–560. doi:10.1016/j.apcatb.2016.11.062.
- [80] Q.H. Low, N.W.X. Loo, F. Calle-Vallejo, B.S. Yeo, Enhanced electroreduction of carbon dioxide to methanol using zinc dendrites pulse-deposited on silver foam, *Angew. Chemie - Int. Ed.* 58 (2019) 2256–2260. doi:10.1002/anie.201810991.
- [81] R. Kortlever, J. Shen, K.J.P. Schouten, F. Calle-Vallejo, M.T.M. Koper, Catalysts and reaction pathways for the electrochemical reduction of carbon dioxide, *J. Phys. Chem. Lett.* 6 (2015) 4073–4082. doi:10.1021/acs.jpcclett.5b01559.

- [82] Y. Wang, H. Hu, Y. Sun, Y. Tang, L. Dai, Q. Hu, A. Fisher, X.J. Yang, Facile Synthesis of Nanostructural High-Performance Cu–Pb Electrocatalysts for CO₂ Reduction, *Adv. Mater. Interfaces*. 6 (2019) 1–7. doi:10.1002/admi.201801200.
- [83] Y. Chen, M.W. Kanan, Tin oxide dependence of the CO₂ reduction efficiency on tin electrodes and enhanced activity for tin/tin oxide thin-film catalysts, *J. Am. Chem. Soc.* 134 (2012) 1986–1989. doi:10.1021/ja2108799.
- [84] S. Sarfraz, A.T. Garcia-Esparza, A. Jedidi, L. Cavallo, K. Takanabe, Cu–Sn bimetallic catalyst for selective aqueous Electroreduction of CO₂ to CO, *Acs Catal.* 6 (2016) 2842–2851. doi:10.1021/acscatal.6b00269.
- [85] Q. Li, J.J. Fu, W.L. Zhu, Z.Z. Chen, B. Shen, L.H. Wu, Z. Xi, T.Y. Wang, G. Lu, J.J. Zhu, S.H. Sun, Tuning Sn-catalysis for electrochemical reduction of CO₂ to CO via the core/shell Cu/SnO₂ structure, *J. Am. Chem. Soc.* 139 (2017) 4290–4293. doi:10.1021/jacs.6b00261.
- [86] C. Kim, T. Möller, J. Schmidt, A. Thomas, P. Strasser, Suppression of competing reaction channels by Pb adatom decoration of catalytically active Cu surfaces during CO₂ electroreduction, *ACS Catal.* 9 (2019) 1482–1488. doi:10.1021/acscatal.8b02846.
- [87] W. Luc, C. Collins, S. Wang, H. Xin, K. He, Y. Kang, F. Jiao, Ag–sn bimetallic catalyst with a core-shell structure for CO₂ reduction, *J. Am. Chem. Soc.* 139 (2017) 1885–1893. doi:10.1021/jacs.6b10435.
- [88] E.L. Clark, C. Hahn, T.F. Jaramillo, A.T. Bell, Electrochemical CO₂ reduction over compressively strained CuAg surface alloys with enhanced multi-carbon oxygenate selectivity, *J. Am. Chem. Soc.* 139 (2017) 15848–15857. doi:10.1021/jacs.7b08607.
- [89] D. Higgins, A.T. Landers, Y. Ji, S. Nitopi, C.G. Morales-Guio, L. Wang, K. Chan, C. Hahn, T.F. Jaramillo, Guiding electrochemical carbon dioxide reduction toward carbonyls using copper silver thin films with interphase miscibility, *ACS Energy Lett.* 3 (2018) 2947–2955. doi:10.1021/acsenerylett.8b01736.
- [90] S. Lee, G. Park, J. Lee, Importance of Ag–Cu biphasic boundaries for selective electrochemical reduction of CO₂ to ethanol, *ACS Catal.* 7 (2017) 8594–8604. doi:10.1021/acscatal.7b02822.
- [91] S.Y. Choi, S.K. Jeong, H.J. Kim, I.-H. Baek, K.T. Park, Electrochemical reduction of carbon dioxide to formate on tin–lead alloys, *ACS Sustain. Chem. Eng.* 4 (2016) 1311–1318. doi:10.1021/acssuschemeng.5b01336.
- [92] X. Bai, W. Chen, C. Zhao, S. Li, Y. Song, R. Ge, W. Wei, Y. Sun, Exclusive formation of formic acid from CO₂ electroreduction by a tunable Pd–Sn alloy, *Angew. Chemie - Int. Ed.* 56 (2017) 12219–12223. doi:10.1002/anie.201707098.
- [93] D.A. Torelli, S.A. Francis, J.C. Crompton, A. Javier, J.R. Thompson, B.S. Brunshwig, M.P. Soriaga, N.S. Lewis, nickel–gallium-catalyzed electrochemical reduction of CO₂ to highly reduced products at low overpotentials, *ACS Catal.* 6 (2016) 2100–2104. doi:10.1021/acscatal.5b02888.
- [94] A.R. Paris, A.B. Bocarsly, Mechanistic insights into C₂ and C₃ product generation using Ni₃Al and Ni₃Ga electrocatalysts for CO₂ reduction, *Faraday Discuss.* 215 (2019) 192–204. doi:10.1039/C8FD00177D.
- [95] W. Luc, C. Collins, S. Wang, H. Xin, K. He, Y. Kang, F. Jiao, Ag–sn bimetallic catalyst with a core-shell structure for CO₂ reduction, *J. Am. Chem. Soc.* 139 (2017) 1885–1893. doi:10.1021/jacs.6b10435.
- [96] M. Morimoto, Y. Takatsuji, R. Yamasaki, Electrodeposited Cu–Sn alloy for electrochemical CO₂ Reduction to CO/HCOO[−], (2017) 323–332.
- [97] K. Yu, Z. Wu, Q. Zhao, B. Li, Y. Xie, High-temperature-stable Au@SnO₂ core/shell supported catalyst for CO oxidation, *J. Phys. Chem. C.* 112 (2008) 2244–2247. doi:10.1021/jp711880e.
- [98] K. Yu, T. Yao, Z. Pan, S. Wei, Y. Xie, Structural evolution in the nanoscale diffusion process: a Au–Sn bimetallic system, *J. Chem. Soc. Dalt. Trans.* (2009) 10353–10358. doi:10.1039/b916215a.
- [99] E. Csapó, A. Oszkó, E. Varga, Á. Juhász, N. Buzás, L. Kőrösi, A. Majzik, I. Dékány, Synthesis and

- characterization of Ag/Au alloy and core(Ag)–shell(Au) nanoparticles, *Colloids Surfaces A Physicochem. Eng. Asp.* 415 (2012) 281–287. doi:10.1016/j.colsurfa.2012.09.005.
- [100] F.H. Ko, M.R. Tai, F.K. Liu, Y.C. Chang, Au-Ag core-shell nanoparticles with controllable shell thicknesses for the detection of adenosine by surface enhanced Raman scattering, *Sensors Actuators, B Chem.* 211 (2015) 283–289. doi:10.1016/j.snb.2015.01.047.
- [101] N.G. Bastús, F. Merkoçi, J. Piella, V. Puntes, Synthesis of highly monodisperse citrate-stabilized silver nanoparticles of up to 200 nm: kinetic control and catalytic properties, *Chem. Mater.* 26 (2014) 2836–2846. doi:10.1021/cm500316k.
- [102] I.D. Baikie, A.C. Grain, J. Sutherland, J. Law, Ambient pressure photoemission spectroscopy of metal surfaces, *Appl. Surf. Sci.* 323 (2014) 45–53. doi:10.1016/j.apsusc.2014.08.159.
- [103] G. Kresse, J. Hafner, Ab initio molecular dynamics for liquid metals, *Phys. Rev. B.* 47 (1993) 558–561. doi:10.1103/PhysRevB.47.558.
- [104] G. Kresse, J. Hafner, Ab initio molecular-dynamics simulation of the liquid-metalamorphous-semiconductor transition in germanium, *Phys. Rev. B.* 49 (1994) 14251–14269. doi:10.1103/PhysRevB.49.14251.
- [105] G. Kresse, J. Furthmüller, Efficiency of ab-initio total energy calculations for metals and semiconductors using a plane-wave basis set, *Comput. Mater. Sci.* 6 (1996) 15–50. doi:10.1016/0927-0256(96)00008-0.
- [106] G. Kresse, J. Furthmüller, Efficient iterative schemes for ab initio total-energy calculations using a plane-wave basis set, *Phys. Rev. B.* 54 (1996) 11169–11186. doi:10.1103/PhysRevB.54.11169.
- [107] J.P. Perdew, K. Burke, M. Ernzerhof, Generalized gradient approximation made simple, *Phys. Rev. Lett.* 77 (1996) 3865–3868. doi:10.1103/PhysRevLett.77.3865.
- [108] J.P. Perdew, K. Burke, M. Ernzerhof, Generalized gradient approximation made simple [*Phys. Rev. Lett.* 77, 3865 (1996)], *Phys. Rev. Lett.* 78 (1997) 1396–1396. doi:10.1103/PhysRevLett.78.1396.
- [109] P.E. Blöchl, Projector augmented-wave method, *Phys. Rev. B.* 50 (1994) 17953–17979. doi:10.1103/PhysRevB.50.17953.
- [110] G. Kresse, D. Joubert, From ultrasoft pseudopotentials to the projector augmented-wave method, *Phys. Rev. B.* 59 (1999) 1758–1775. doi:10.1103/PhysRevB.59.1758.
- [111] X. Nie, M.R. Esopi, M.J. Janik, A. Asthagiri, Selectivity of CO₂ reduction on copper electrodes: the role of the kinetics of elementary steps, *Angew. Chemie Int. Ed.* 52 (2013) 2459–2462. doi:10.1002/anie.201208320.
- [112] R. García-Muelas, F. Dattila, T. Shinagawa, A.J. Martín, J. Pérez-Ramírez, N. López, Origin of the selective electroreduction of carbon dioxide to formate by chalcogen modified copper, 9 (2018) 7153–7159. doi:10.1021/acs.jpcllett.8b03212.
- [113] M. Álvarez-Moreno, C. de Graaf, N. López, F. Maseras, J.M. Poblet, C. Bo, Managing the computational chemistry big data problem: the ioChem-BD platform, *J. Chem. Inf. Model.* 55 (2015) 95–103. doi:10.1021/ci500593j.
- [114] N. Arora, B.R. Jagirdar, From (Au₅Sn + AuSn) physical mixture to phase pure AuSn and Au₅Sn intermetallic nanocrystals with tailored morphology: digestive ripening assisted approach, *Phys. Chem. Chem. Phys.* 16 (2014) 11381–11389. doi:10.1039/c4cp00249k.
- [115] J.A. Taylor, S.M. Merchant, D.L. Perry, Study of the oxidation of gold-tin preforms using x-ray photoelectron spectroscopy, *J. Appl. Phys.* 78 (1995) 5356–5361. doi:10.1063/1.359715.
- [116] J.Y. Cheon, J.H. Kim, J.H. Kim, K.C. Goddeti, J.Y. Park, S.H. Joo, Intrinsic relationship between enhanced oxygen reduction reaction activity and nanoscale work function of doped carbons, *J. Am. Chem. Soc.* 136 (2014) 8875–8878. doi:10.1021/ja503557x.

- [117] M. Dunwell, Q. Lu, J.M. Heyes, J. Rosen, J.G. Chen, Y. Yan, F. Jiao, B. Xu, The central role of bicarbonate in the electrochemical reduction of carbon dioxide on gold, *J. Am. Chem. Soc.* 139 (2017) 3774–3783. doi:10.1021/jacs.6b13287.
- [118] S. Zhu, B. Jiang, W. Bin Cai, M. Shao, Direct observation on reaction intermediates and the role of bicarbonate anions in CO₂ electrochemical reduction reaction on Cu surfaces, *J. Am. Chem. Soc.* 139 (2017) 15664–15667. doi:10.1021/jacs.7b10462.
- [119] D. Hursán, C. Janáky, Electrochemical reduction of carbon dioxide on nitrogen-doped carbons: insights from isotopic labeling studies, *ACS Energy Lett.* 3 (2018) 722–723. doi:10.1021/acseenergylett.8b00212.
- [120] J.E. Pander, D. Ren, Y. Huang, N.W.X. Loo, S.H.L. Hong, B.S. Yeo, Understanding the heterogeneous electrocatalytic reduction of carbon dioxide on oxide-derived catalysts, *ChemElectroChem.* 5 (2018) 219–237. doi:10.1002/celec.201701100.
- [121] A. Dutta, A. Kuzume, M. Rahaman, S. Vesztergom, P. Broekmann, Monitoring the chemical state of catalysts for CO₂ electroreduction: an in operando study, *ACS Catal.* 5 (2015) 7498–7502. doi:10.1021/acscatal.5b02322.
- [122] Y. Ichinohe, T. Wadayama, A. Hatta, Electrochemical reduction of CO₂ on Silver as probed by surface-enhanced Raman scattering, *J. RAMAN Spectrosc.* 26 (1995) 335–340. doi:10.1021/ja00330a064.
- [123] A. Kar, S. Kundu, A. Patra, Surface defect-related luminescence properties of SnO₂ nNanorods and nanoparticles, *J. Phys. Chem. C.* 115 (2011) 118–124. doi:10.1021/jp110313b.
- [124] A. Dutta, A. Kuzume, V. Kaliginedi, M. Rahaman, I. Sinev, M. Ahmadi, B. Roldán Cuenya, S. Vesztergom, P. Broekmann, Probing the chemical state of tin oxide NP catalysts during CO₂ electroreduction: A complementary operando approach, *Nano Energy.* 53 (2018) 828–840. doi:10.1016/j.nanoen.2018.09.033.
- [125] E.A. Batista, M.L.A. Temperini, Spectroscopic evidences of the presence of hydrogenated species on the surface of copper during CO₂ electroreduction at low cathodic potentials, *J. Electroanal. Chem.* 629 (2009) 158–163. doi:10.1016/j.jelechem.2009.02.010.
- [126] J.L. Castro, J.C. Otero, J.I. Marcos, Anomalous SERS of monocarboxylic acids on silver sols, *J. Raman Spectrosc.* 28 (1997) 765–769. doi:10.1002/(sici)1097-4555(199710)28:10<765::aid-jrs145>3.0.co;2-o.
- [127] J.-H. Liu, A.-Q. Wang, Y.-S. Chi, H.-P. Lin, C.-Y. Mou, Synergistic effect in an Au–Ag alloy nanocatalyst: CO oxidation, *J. Phys. Chem. B.* 109 (2005) 40–43. doi:10.1021/jp044938g.
- [128] J. Rosen, G.S. Hutchings, Q. Lu, S. Rivera, Y. Zhou, D.G. Vlachos, F. Jiao, Mechanistic insights into the Electrochemical Reduction of CO₂ to CO on nanostructured Ag surfaces, *ACS Catal.* 5 (2015) 4293–4299. doi:10.1021/acscatal.5b00840.
- [129] L.Q. Zhou, C. Ling, M. Jones, H. Jia, Selective CO₂ reduction on a polycrystalline Ag electrode enhanced by anodization treatment, *Chem. Commun.* 51 (2015) 17704–17707. doi:10.1039/c5cc06752a.
- [130] T. Hatsukade, K.P. Kuhl, E.R. Cave, D.N. Abram, T.F. Jaramillo, Insights into the electrocatalytic reduction of CO₂ on metallic silver surfaces, *Phys. Chem. Chem. Phys.* 16 (2014) 13814–13819. doi:10.1039/C4CP00692E.
- [131] P. Liu, J.K. Nørskov, Ligand and ensemble effects in adsorption on alloy surfaces, *Phys. Chem. Chem. Phys.* 3 (2001) 3814–3818. doi:10.1039/b103525h.
- [132] J.K. Nørskov, T. Bligaard, J. Rossmeisl, C.H. Christensen, Towards the computational design of solid catalysts, *Nat. Chem.* 1 (2009) 37–46. doi:10.1038/nchem.121.
- [133] A. Kahn, Fermi level, work function and vacuum level, *Mater. Horizons.* 3 (2016) 7–10. doi:10.1039/c5mh00160a.
- [134] H.A. Hansen, J.B. Varley, A.A. Peterson, J.K. Nørskov, Understanding trends in the electrocatalytic activity of metals and enzymes for CO₂ reduction to CO, *J. Phys. Chem. Lett.* 4 (2013) 388–392.

doi:10.1021/jz3021155.

- [135] L. Burgio, R.J.H. Clark, S. Firth, Raman spectroscopy as a means for the identification of plattnerite (PbO_2), of lead pigments and of their degradation products, *Analyst*. 126 (2001) 222–227. doi:10.1039/b008302j.
- [136] B.D. Smith, D.E. Irish, A surface enhanced raman scattering study of the intermediate and poisoning species formed during the electrochemical reduction of CO_2 on Copper, 144 (1997) 4288–4296. doi:10.1149/1.1838180.
- [137] H. Xiao, T. Cheng, W.A. Goddard, R. Sundararaman, Mechanistic explanation of the pH dependence and onset potentials for hydrocarbon products from electrochemical reduction of CO on Cu (111), *J. Am. Chem. Soc.* 138 (2016) 483–486. doi:10.1021/jacs.5b11390.

Acknowledgments

I am thankful for Doctoral School of Chemistry at University of Szeged and the Head of Department of Physical Chemistry and Material Science, **Dr. Ágota Tóth**, for her time and the continuous support to the international students throughout the doctoral work.

I would like to thank my supervisors, **Dr. Csaba Janáky** and **Dr. Edit Csapó**, for assisting in the development of my scientific research skills, and without their support, the result presented in this dissertation would have not been possible. Progress was slow at first; it took nearly one year to develop a synthesis method for the first bimetallic system, which was frustrating from a results perspective. However, through the entire time, my advisors managed to stay optimistic and excited. I am also grateful for the great opportunities I had to take part in international conferences and training schools as well as all the encouraging words provided by them to my work. Really, I am also fortunate to be a part of Janáky's lab and Edit Csapó's lab, where I got more knowledge about the different synthesis strategies of bimetallic nanoparticles and how investigate the electrocatalytic activity in carbon dioxide reduction.

Thanks much to the former, and current members of the research group for their help in the beginning of my work and for the friendly, and creative working environment. I would like to highlight the help of Dr. Gábor Bencsik, Dr. Dorottya Hursán, Dr. Gergely Ferenc Samu, Dr. Jie He, Egon Kecsenovity, Ádám Balog, and Ms. Katalin Sziveri

I acknowledge a scholarship from Egypt's Ministry of Higher Education and Scientific Research, and the support I have received from Egypt's office for cultural and Educational Relations in Vienna is greatly acknowledged. I also acknowledge a scholarship from Tempus Public Foundation (TPS).

In addition to those who had a scientific influence on my graduate research career, I am thankful for the presence of many people who supported me on a personal level. **My parents** encouraged my university education and doctoral studies without applying too much pressure and helped me in the path I chose. Thanks to **my Father** who is defiantly the inspiration for studying chemistry. I am also fortunate to have kind sisters who helped keep me on track through the challenges of the last six years.

I am also thankful for many friends at Szeged who have offered an amazing atmosphere for social activities throughout without distractions from work. I have had excellent companions, lastly, I would like to thank the solidarity of the Egyptian Community in Hungary.

Dedicated to
My beloved Parents & Sisters

Publication list

Hungarian Scientific Bibliography (MTMT) identifier: 10071976g

Publications related to the scientific topic of the dissertation

- 1) **Ahmed Mohsen Ismail**, Gergely F. Samu, Ádam Balog, Edit Csapó, and Csaba Janáky
Composition-Dependent Electrocatalytic Behavior of Au–Sn Bimetallic Nanoparticles in Carbon Dioxide Reduction.
ACS Energy Lett. **2019**, *4*, 48–53. doi:10.1021/acseenergylett.8b01996
- 2) **Ahmed Mohsen Ismail**, Edit Csapó, and Csaba Janáky
Correlation between the Work Function of Au–Ag Nanoalloys and Their Electrocatalytic Activity in Carbon Dioxide Reduction.
Electrochim. Acta **2019**, *313*, 171–178. doi:10.1016/j.electacta.2019.05.016
- 3) **Ahmed Mohsen Ismail**, Gergely F. Samu, Huu Chuong Nguyễn, Edit Csapó, Núria López, and Csaba Janáky
Au/Pb Interface Allows Methane Formation Pathway in Carbon Dioxide Electroreduction
ACS Catal. **2020**, *10*, 5681–5690. doi:10.1021/acscatal.0c00749

Conference Lectures and Posters**Lecture:**

- 1) **Ahmed Mohsen Ismail**, Gergely F. Samu, Edit Csapó, and Csaba Janáky
Electrochemical CO₂ Reduction at Different Au-Sn Bimetallic Catalysts
International Symposium on Electrocatalysis (Electrocat2018)
29 August – 1 September, 2018, Szczyrk, Poland
- 2) **Ahmed Mohsen Ismail**, Gergely F. Samu, Edit Csapó, and Csaba Janáky
Au-Sn Bimetallic Electrocatalysts for Electrochemical CO₂ Reduction
8th Szeged International Workshop on Advances in Nanoscience (SIWAN 8)
7 – 10 October, 2018, Szeged, Hungary
- 3) **Ahmed Mohsen Ismail**, Edit Csapó, and Csaba Janáky
Bimetallic electrocatalysts for electrochemical CO₂ reduction
International symposium intermetallic Compounds in Catalysis (IMCAT 2019)
17 – 19 September, 2019, Chemnitz, Germany

Posters:

- 1) **Ahmed Mohsen Ismail**, Gergely F. Samu, Edit Csapó, and Csaba Janáky
Composition Dependent Electrocatalytic Behavior of Sn-Au Bimetallic Nanoparticles in Carbon-dioxide Reduction
69th Annual Meeting of the International Society of Electrochemistry
2 – 7 September, 2018, Bologna, Italy
- 2) **Ahmed Mohsen Ismail**, Edit Csapó, and Csaba Janáky
Au-Ag Bimetallic Catalysts with Different Composition for CO₂ Reduction
International Workshop on Electrochemistry of Electroactive Materials (WEEM – 2019)
16 – 21 June, 2019, Borovets, Bulgaria
- 3) **Ahmed Mohsen Ismail**, Edit Csapó, and Csaba Janáky
Bimetallic electrocatalysts for electrochemical CO₂ reduction
International symposium intermetallic Compounds in Catalysis (IMCAT 2019)
17 – 19 September, 2019, Chemnitz, Germany

Co-author of conference posters

- 1) Edit Csapó, Ditta Ungor, Ádám Juhász, Csaba Janáky, **Ahmed Mohsen Ismail**
Noble metal colloids: development of optical sensors and electrocatalysts
8th International Workshop on Advances in Nanoscience (SIWAN 8)
7– 10 October, 2018, Szeged, Hungary

- 2) Edit Csapó, Ditta Ungor, Ádám Juhász, Csaba Janáky, **Ahmed Mohsen Ismail**
Size-controlled noble metal colloids and clusters: development of electrocatalysts and optical biosensors
9th International Colloids Conference (COLL2019)
16 – 19 June, 2019, Barcelona-Sitges, Spain